Doctoral theses at NTNU, 2014:132

Xiang Tan

Numerical Investigation of Ship's Continuous-Mode Icebreaking in Level Ice

Doctoral Thesis

Xiang Tan

ISBN 978-82-326-0188-2 (printed version)
ISBN 978-82-326-0189-9 (electronic version)
ISSN 1503-8181

NTNU – Trondheim
Norwegian University of
Science and Technology

NTNU
Norwegian University of
Science and Technology
Faculty of Engineering
Science and Technology
Department of Marine Technology

Doctoral theses at NTNU, 2014:132

NTNU

NTNU – Trondheim
Norwegian University of
Science and Technology

Xiang Tan

Numerical Investigation of Ship's Continuous-Mode Icebreaking in Level Ice

Thesis for the degree of Philosophiae Doctor

Trondheim, May 2014

Norwegian University of Science and Technology
Faculty of Engineering Science and Technology
Department of Marine Technology

NTNU – Trondheim
Norwegian University of
Science and Technology

NTNU
Norwegian University of Science and Technology

Thesis for the degree of Philosophiae Doctor

Faculty of Engineering Science and Technology
Department of Marine Technology

ISBN 978-82-326-0188-2 (printed version)
ISBN 978-82-326-0189-9 (electronic version)
ISSN 1503-8181

Doctoral theses at NTNU, 2014:132

Printed by Skipnes Kommunikasjon as

To my parents,
who gave me the world.

Abstract

This thesis is a summary of studies that were carried out as part of candidacy for a PhD degree. The purpose of these studies was to evaluate some factors in ship design that are intended for navigating in ice using numerical simulations. A semi-empirical numerical procedure was developed by combining mathematical models that describe the various elements of the continuous-mode icebreaking process in level ice. The numerical procedure was calibrated and validated using full- and model-scale measurements. The validated numerical model was in turn used to investigate and clarify issues that have not been previously considered.

An icebreaker typically breaks ice by its power, its weight and a strengthened bow with low stem angle. The continuous icebreaking process involves heave and pitch motions that may not be negligible. The numerical procedure was formulated to account for all of the possible combinations of motions for six degrees of freedom (DOFs). The effects of the motion(s) for certain DOF(s) were investigated by comparing simulations in which the relevant motion(s) were first constrained and then relieved.

In the continuous-mode icebreaking process, a ship interacts with an icebreaking pattern consisting of a sequence of individual icebreaking events. The interactions among the key characteristics of the icebreaking process, i.e., the icebreaking pattern, ship motions, and ice resistance, were studied using the numerical procedure in which the ship motions and excitation forces were solved for in the time domain and the ice edge geometry was simultaneously updated.

Observations at various test scales have shown that the crushing pressure arising from the ice–hull interaction depends on the contact area involved. A parametric study was carried out on the numerical procedure to investigate the effect of the contact pressure on icebreaking.

The loading rates associated with the ship's forward speed have been anticipated to play an important role in determining the bending failure loads, in view of the dynamic water flow underneath the ship and the inertia of the ice. The dynamic bending behavior of ice could also explain the speed dependence of the icebreaking resistance component. A dynamic bending failure criterion for ice was derived, incorporated into the numerical procedure and then validated using full-scale data. The results obtained using the dynamic and static bending failure criteria were compared to each other.

In addition, the effect of the propeller flow on the hull resistance for ships running propeller first in level ice was investigated by applying the information obtained from model tests to the numerical procedure. The thrust deduction in ice was discussed.

Acknowledgements

Working on the PhD project has been a challenging and exciting episode of my life. I would like to give my gratitude to the following people who have helped and encouraged me in different ways.

To my supervisor Prof. Torgeir Moan, who offered me a possibility to pursue my study on ice, otherwise I may have been working in an irrelevant field, in view of climate change which makes it not always easy to find the perfect research object in the Chinese Seas nowadays. Throughout the supervision, he kept his trust, patience and sense of humor when I had lost mine.

To my co-supervisor Prof. Kaj Riska, without the support from whom the present thesis would not have been completed. Encouraged by his words:" *there is no stupid questions only stupid answers*", I indeed traded some lousy questions for many really good answers, which reshaped my understanding of ship design for ice.

To the editors and anonymous reviewers of the scientific publications to which I submitted my papers. Their constructive feedbacks have helped to make the papers more presentable.

To Dr. Biao Su for providing valuable time and knowledge in discussing the details of the numerical model and troubleshooting the computer routine.

To Dr. Yanlin Shao, who helped me construct the first lines of my first ship model.

To Mr. Xiangyue Zhang, who introduced Norway to me, for lots and lots of assistance he provided when I made my application.

To all the staff at the Centre for Ships and Ocean Structures (CeSOS) and the Department of Marine Technology for their administrative help.

I would also like to thank the Research Council of Norway for financial support through CeSOS during the first three years. Thank Total E&P Norge AS for the financial support for the last one-and-a-half years.

Finally, thank those whose names I want to keep to myself, for through them, I saw the self of mine.

18.12.2013
Trondheim

Publications

Appended Papers

The three papers incorporated into this thesis constitute an essential part of a coherent and integral body of work which is focused on a set of related issues on ship's continuous-mode icebreaking in level ice.

Paper 1:

A six-degrees-of-freedom numerical model for level ice–ship interaction
Tan, X., Su, B., Riska, K. and Moan, T.
Published in *Cold Regions Science and Technology*, 2013

Paper 2:

Effect of dynamic bending of level ice on ship's continuous-mode icebreaking
Tan, X., Riska, K. and Moan, T.
Revised manuscript submitted to *Cold Regions Science and Technology*

Paper 3:

Performance simulation of a dual-direction ship in level ice
Tan, X., Riska, K. and Moan, T.
Under review in the *Journal of Ship Research*

Other Papers

Papers listed below are not incorporated into the thesis as they are the primitive versions of the appended papers.

The effect of heave, pitch and roll motions to ice performance of ships
Tan, X., Su, B., Riska, K. and Moan, T.
Accepted for oral presentation and published in proceedings of the *21st IAHR International Symposium on Ice*. 11–15 June, 2012, Dalian, China.

Effect of ship speed on ship's ice resistance with ship's vertical motions included
Tan, X., Riska, K. and Moan, T.
Accepted for oral presentation and published in proceedings of the *PRADS2013*. 20–25 October, 2013, Changwon City, Korea.

Declaration of Authorship

The publications listed above are co-authored. As the first author of the papers, I developed the numerical procedure, practiced the calculations, analyzed the results, and wrote the papers. The work was carried out under the supervision of Prof. Torgeir Moan and Prof. Kaj Riska who are co-authors of these papers. Prof. Kaj Riska has contributed to initiating the topics, providing measurement data and reviewing the results. Prof. Torgeir Moan has contributed to supporting and giving constructive criticism to enhance the quality of the publications. As the second author of appended paper 1, Dr. Biao Su provided the initial algorithm for the ice–ship contact modular and useful guidance. In appended papers 2 and 3, the algorithm for the ice–ship contact modular was re-programmed by the author of this thesis to make necessary improvements.

Contents

1

Introduction

1.1 General

> The Arctic *"used to be the last frontier, now it seems like we are at the center of the world."*

said the former prime minister of Greenland at a forum hosted by the Energy Security Initiative at the Brookings Institution in April, 2013. A study conducted by the US Geological Survey (USGS) in 2008 indicated that the Arctic may hold 90 billion barrels of oil, 1669 trillion cubic feet of natural gas and 44 billion barrels of natural gas liquids, of which approximately 84 percent is expected to occur in offshore areas (USGS, 2008). At the same time, global energy demand will increase by a third by 2035, and nearly half of the world's existing production capacity will be phased out, as estimated by the International Energy Agency (IEA) in *World Energy Outlook* 2013 (WEO, 2013).

These foreseeable massive developments in the Arctic impelled by great access to natural resources and climate change entail both opportunities and challenges.

The hard and thick retreating multiyear sea ice provides easier access to valuable natural resources in the high north. Offshore oil companies are heading north, and exploration licenses are being issued across the Arctic rim nations. In addition, the extent of the summer sea ice is receding, and the northern sea lanes (the Northern Sea Route and North-west Passage), which serve as a shortcut to connect western Europe and the US Atlantic Seaboard with the Far East, are nearly free of ice during the summer navigation periods. Forty-three ships sailed the Northern Sea Route in 2012, in contrast to a total of three or four in 2010. This is appealing to maritime companies conducting cargo and crude oil transportation, especially the bulk transport of oil, gas, ores, and minerals, between the East and the West. Furthermore, as a newly emerging tourist destination, the Arctic is attracting increasing numbers of people due to the beauty of its untamed nature.

However, development activities in the Arctic present additional challenges to those commonly encountered in open waters. Natural factors characterizing Arctic conditions include low temperatures, perpetual darkness in winter, extreme weather, remoteness, and the presence of ice, all of which must be considered to

ensure the overall safety of Arctic marine activities. Among these factors, the presence of ice cover poses the single largest challenge in the design and operation of Arctic marine structures.

For ships navigating in ice-infested waters, ice loads represent the dominant load. A ship can either be designed to a high ice class with a high cost for independent navigation or to a low ice class with the possible escort of icebreakers, depending on the operational profile. Ice conditions vary in time from day to day in tactical, voyage planning sense and from month to month (or even from year to year) in strategic, transport chain design sense (Riska, 2011). Spatially, a ship navigating in ice encounters various ice conditions due to its possible operation over a large geographical area. The variation in the ice conditions affects the operational profile because the voyage typically partially involves open water and partially involves ice at various degrees of ice concentrations. The designation of an ice class thus requires a compromise between the ship performance (safety) over the entire voyage and the commercial return. That is, a design should factor in both technological and economic considerations. The goal is to achieve adequate performance, adequate hull and machinery strength and proper functioning of the ship in ice and in cold weather (Riska, 2010).

The harsh environment of Arctic regions demands innovative solutions. Arctic ship technology, which is the main subject for naval architects and Arctic engineers, has been evolving in conjunction with the exploration and transportation activities in ice-infested waters. However, there is inevitably a time lag between the developments of design codes and the technological innovations. In addition, the design codes do not address the mechanisms involved in an ice–ship interaction. The studies included in this thesis explore the technological aspects of ship design with respect to ship performance in level ice. The aim is to develop insight into a ship's continuous-mode icebreaking process using numerical modeling. Numerical modeling can supplement existing design methods by accounting for technological innovations and providing detailed information from direct calculations.

1.2 Objectives, scope, and organization of the thesis

In this thesis, numerical methods are used to investigate factors in ship design that affect ship performance in ice. A numerical procedure was formulated to simulate the dynamic process of continuous-mode icebreaking for ships in level ice by integrating semi-empirical ice load models and ship theories. The effect of the hull shape on the ice resistance was considered by modeling the true geometry of the ship hull. The material properties of the ice were assumed to be deterministic.

These numerical simulations are supplementary to full- and model-scale measurements.

The main objectives are as follows:

1) to simulate the interaction between a ship hull and a level ice sheet with ship motions in 6 DOFs;
2) to investigate the interactions among the ship motions, icebreaking pattern, and ice resistance (ship performance);
3) to quantify the effect of the average contact pressure;
4) to introduce the speed dependence of the icebreaking resistance component; and
5) to clarify the effect of the propeller flow on the ice resistance when the ship runs astern.

The thesis is composed of the following chapters.

In **Chapter 1**, the general background, objectives, scope, and organization of the thesis are presented.

In **Chapter 2**, an overview is presented of existing research on ship performance in ice to serve as a background for the present study in terms of the theories and methodologies used to address this problem.

In **Chapter 3**, the modeling methodology, which consists of the underlying assumptions, theories, and numerical implementation, used to develop the numerical procedure that is used to conduct the studies outlined below is described.

In **Chapter 4**, the interactions among the three key characteristics in the ship's continuous-mode icebreaking in level ice are investigated: the ship motions, icebreaking pattern, and ice resistance (ship performance). A case study is conducted on the Anchor Handling and Towing Supply vessel/Ice Breaker (AHTS/IB) Tor Viking II. The results are compared with full-scale data.

In **Chapter 5**, the effect of the average contact pressure is investigated. A parametric study is carried out on the AHTS/IB Tor Viking II to quantify the effect of the pressure–area (p–a) relation. The values for the parameters of the p–a curve are determined by calibrating the numerical model with full-scale data.

In **Chapter 6**, the effect of the ice bending failure criterion on the ship motions, ice resistance, and ship performance is investigated for continuous-mode icebreaking in level ice. The ice dynamic bending failure criterion developed in **Chapter 3** is

incorporated into the numerical procedure to investigate the effect of the ship's forward speed. A case study on the AHTS/IB Tor Viking II is presented.

In **Chapter 7**, the performance of a dual-direction ship is investigated. The information obtained from the model tests is used to study the effect of the "bow propeller". A case study on the M/T Uikku is conducted at model scale.

In **Chapter 8**, the work presented in previous chapters is summarized along with primary conclusions of the study, and recommendations for future work are provided.

The thesis consists of a summary and three appended scientific papers. The structure and inter-connections between the studies are shown in Fig. 1.1.

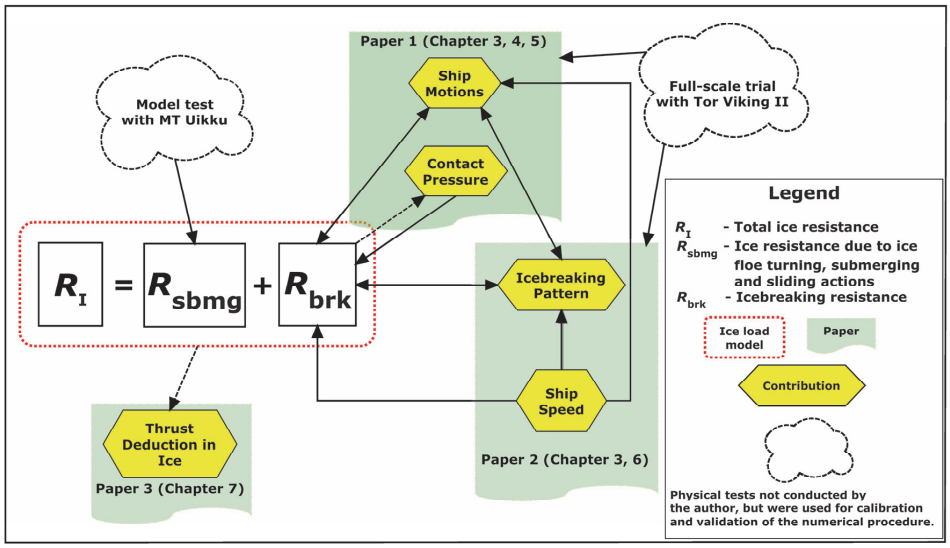

Fig. 1.1 Scope of work and inter-connections between papers

2

Overview of Studies on Ship Performance in Ice

The performance of ships in ice is measured by their ability to break (or to maneuver in) the ice while maintaining a certain forward speed or proper functioning. These requirements can be achieved by optimizing the designs of the hull and the propulsion system to lower the hull resistance in ice and to increase the propulsion thrust, respectively. In general, optimal designs involve knowledge about the interactions among the ship hull, intact ice cover, broken ice floes, water, and propeller. In this chapter, a review of the existing literature on ship performance primarily in level ice is presented to serve as a background for this thesis in terms of the theories and research methodologies used in the field.

2.1 Hull ice resistance

2.1.1 Analytical formulations

Ice resistance is the time average of the longitudinal resistance a ship experiences when moving in ice.

The first formulation of ice resistance was published by Runeberg (1888/89), who recognized the importance of the friction between ice and the ship hull as well as that of the stem angle at the waterline: these factors are still regarded as important in the modern design of ice-capable ships.

In a historical review of literature on ship performance in ice, Jones (2004) introduced the work of Shimanskii (1938), in which a semi-empirical method was employed to investigate the continuous-mode icebreaking resistance. Shimanskii (1938)'s work is likely the first attempt to relate the ice resistance to design parameters, in which a form has been developed for resistance whereas the values of the coefficients have been determined using full-scale data.

Kashteljan et al. (1968) were the first to decompose the ice resistance into components with different physical origins (namely, icebreaking, ice floe turning and submerging, and broken ice resistance) and provided detailed expressions for

these components that were based on model- and full-scale tests on the ship *Ermak*.

The basic concepts formulated by Shimanskii (1938) and Kashteljan et al. (1968), such as including semi-empirical design parameters and the decomposition of the ice resistance, are still used today, although the forms of the formulae and the number and definitions of the coefficients have varied from study to study. Non-dimensional approaches (e.g., Lewis and Edwards, 1970), pure analytical approaches (e.g., White, 1970; Milano, 1973), and regression analysis (e.g., Vance, 1975) have been used in combination with full-scale experiences and model tests (e.g., Tatinclaux, 1984) to derive various semi-empirical ice resistance formulae (e.g., Edwards et al., 1976; Naegle, 1980; Kotras et al., 1983; Lewis et al., 1983; Lindqvist, 1989; Keinonen et al., 1991).

The resistance formulae introduced above describe the ice resistance in terms of "design parameters" for the ice properties (e.g., the thickness, strength, and friction), the hull size (e.g., the beam, displacement), the hull form (e.g., the stem angle, waterline angle), and the ship speed. An average value is typically given for the ice resistance in the longitudinal direction. These models were used as practical engineering tools in the early design of icebreaking ships and were generally in passable agreement with full-scale measurements.

2.1.2 Hull ice load models

In the ice resistance models introduced in Section 2.1.1, the resistance is described by a single equation or several equations, and the detailed interaction mechanisms that produce the ice resistance are only included when they enable the mean resistance to be determined. Designers are then forced to treat the problem from a macroscopic perspective, as noted by Lewis and Edwards (1970). The effects of various parameters, such as the friction, local contact pressure, bending behavior of ice, local loading rate, and ship motions are either not considered or are represented implicitly by empirical constants. Moreover, some of these formulae may be overly ship-specific to be extrapolated to different types of ships and thus to satisfy the demands for innovative ship (structure) types and optimal designs.

To better understand the detailed mechanisms of local interaction events, extensive research has been carried out on the physics involved in the different phases of the dynamic process of icebreaking.

For example, information and experiences in friction have accrued (e.g., Jansson, 1956(a); Jansson, 1956(b); Makinen et al., 1975; Scarton, 1975; Saeki et al., 1986; Frederking and Barker, 2002), resulting in modern applications of low-friction and

ice-resistant coatings to the underwater and ice belt area of the hull of ice-capable ships, in addition to many other auxiliary systems that help to further reduce friction and abrasion; the physics of the mechanisms involved in ice–structure contact have been studied to formulate contact models (e.g., Kurdyumov and Kheisin, 1976; Varsta, 1983; Riska, 1987; Joensuu and Riska, 1988; Daley, 1991; Tuhkuri, 1996; Sodhi et al., 1998); the effects of local ice pressures have been analyzed (e.g., Masterson and Frederking, 1993; Masterson et al., 2007; Jordaan et al., 1993; Timco and Sudom, 2013) and incorporated in the ISO 19906 Arctic Structures Standard (ISO, 2010); the bending behavior of floating ice wedges has been investigated (e.g., Kerr, 1975; Varsta, 1983; Izumiyama et al., 1991; Fox, 1993; Dempsey and Zhao, 1993) both experimentally and theoretically; and the relative magnitude of different ice resistance components has been investigated (e.g., Enkvist, 1972; Valanto, 1989).

Moreover, direct calculations of ice loads in 2-D and 3-D have been carried out using advanced finite/discrete element modelling methods (e.g., Valanto, 1992; Valanto, 2001; Løset, 1994; Hopkins, 2004; Liu, 2011; Lu et al., 2012) and other numerical techniques such as particle-in-cell (PIC) (e.g., Sayed et al., 2000; Sayed et al., 2011) and smoothed-particle hydrodynamics (SPH).

These hull ice load models and their methodologies have provided detailed information about the ice–hull interaction from various perspectives. Although the author did not intend to present these studies chronologically, research interests in recent years have actually shifted from single-equation ice resistance formulae (Section 2.1.1) to a better understanding of and modeling based on the physical mechanisms introduced in this section (Section 2.1.2).

2.1.3 Continuous-mode icebreaking

In the continuous-mode icebreaking process, the ice around the ship hull fails repeatedly. A typical icebreaking bow typically has a low stem angle to transmit a large vertical load component that causes the ice in front of the bow to fail by bending. Both model- and full-scale studies (e.g., Lewis and Edwards, 1970; Kotras et al., 1983; Ettema et al., 1987; Ettema et al., 1991; Izumiyama et al., 1991; Valanto, 1993) have shown that the failure of ice sheets by bending and the emergence of a new ice edge follow a seemingly regular pattern consisting of the sequential breaking-off of wedge- and cusp-shaped ice pieces from the intact ice field. The geometry of the ice edge created by repeated breaking is often referred to as an “icebreaking pattern”.

Although icebreaking cycles are essential elements of the continuous icebreaking process, individual icebreaking events may not act in unison: the hull may interact with a pattern of icebreaking rather than with individual breaking events, and the hull motions may affect the cyclic processes by significantly altering the contact geometry and loading pattern, resulting in different rates of ice sheet loading if significant accelerations occur as the ice fails and is suddenly displaced from beneath the bow. Important noncyclical processes also occur because of the non-simultaneous failure of the ice around the ship's hull (Ettema et al., 1987). Thus, the total ice resistance acting on the hull is actually the integral over the icebreaking waterline of the local contact pressure at a single instant in time.

Thus, it is more realistic to investigate the problem from a time domain perspective (e.g., Wang, 2001; Liu, 2009; Aksnes, 2010; Aksnes, 2011a; Aksnes, 2011b; Lubaed and Løset, 2011) and examine the dynamic process by patterns of icebreaking. Wang (2001) developed a numerical model using geometric grid method to simulate the continuous contact between a (flexible) fixed conical structure and a moving ice sheet in the time domain. The icebreaking pattern was reproduced by determining the crack size from the loading rate and ice properties. This strategy was then followed in later studies on different aspects that are relevant to ships in ice, such as dynamic positioning (e.g., Nguyen et al., 2009; Nguyen et al., 2011), ice resistance, and maneuvering (e.g., Martio, 2007; Su et al., 2010a; Su et al., 2010b; Sawamura et al., 2010). In Su et al. (2011), random ice conditions (i.e., the thickness and strength) were also incorporated into the numerical model. Tan et al. (2012) developed a numerical model by extending Su's planar model to a 6-DOF one. The true geometry of the 3-D ship hull was modeled using computational geometry methods. The fully coupled motions of the ship were considered for 6 DOFs together with the corresponding environmental forces. In Tan et al. (2013) (appended paper 1), the effect of the average contact pressure was investigated in a parametric study. The interactions among the icebreaking pattern, ship motions, and ice resistance were also investigated.

2.2 Propulsion for ice-capable ships

Ship performance in ice is influenced by propulsion and hull lines designs, rather than just hull ice resistance, in relation to propulsion power and efficiency, propeller strength, and propeller–hull interaction.

Juva and Riska (2002) developed a method to determine the ship power requirements from the required ship performance. The authors analyzed the K_e factor that relates the propulsion power to the propeller thrust in the Finnish-

Swedish ice class rules (FSICR) and considered that this factor was not a constant but rather a function of the propulsion characteristics, the total resistance to be overcome, and the thrust deduction. The FSICR were shown to produce slightly conservative results.

Juurmaa and Segercrantz (1981) were the first to recognize the importance of the propulsion efficiency in ice and demonstrated that while different ship models might have the same resistance, they could have extremely different overall performances because of different ice–propeller interactions. The authors also noted that nozzle propellers can have extremely low efficiencies when blocked with ice. Veitch (1995) established a dynamic ice load model for marine screw propellers that was primarily based on laboratory ice cutting tests. The model simulates the contact between a propeller blade and a submerged ice body. The pressure distribution at the leading edge area was analyzed computationally, and the ice contact forces on the blade in the time domain were predicted. In the model tests, the ice failure at the leading edge was characterized by an ice chipping process, whereas on the suction side, the ice failed primarily due to the coalescence of small cracks.

Another effect of the propulsion system comes from the propeller–hull interaction. Zahn et al. (1987) conducted a series of full-scale trials in level ice with the ship Mobile Bay. The authors were able to conduct full-scale towed resistance tests that were difficult to perform in which the hull resistance could be measured directly. The authors also derived a thrust deduction factor as a function of the ice thickness by comparing towed resistance tests with additional self-propulsion tests. Kitagawa et al. (1986) conducted a series of model-scale self-propulsion tests and concluded that a minimum parallel mid-body of $0.25L_{\mathrm{pp}}$ was required to prevent an excessive propeller–ice interaction. Leiviskä (2004) conducted a series of model tests to clarify the effect of the thrust deduction for ships running propeller first in ice. Several distinct types of tests were performed to measure the open water characteristics of the propeller, the open water thrust deduction factors, and the added resistance from the propeller–hull–ice interaction in level and brash ice. These tests provided insight into the physical mechanisms of the phenomena observed in bow propellers.

Moreover, the propulsion efficiency has also been improved significantly by installing electric podded propulsion systems with electrical motors in the pods for which no separate rudders and long shaftlines are needed. The high electrical efficiency allows for a full torque to be achieved at a low RPM and a motor over-torque that matches the ice operation requirements, which makes the propulsion

system well suited to dual-direction ships in Arctic waters (see, e.g., Juurmaa et al., 2001; Vocke et al., 2011).

2.3 Remarks

Existing research studies on ship performance in level ice are briefly reviewed in this chapter. The issues that arise in a ship–ice interaction are primarily addressed using research methodologies that can be categorized into three groups: full-scale experiences, laboratory tests, and numerical simulations. Field studies produce the best, real world information; however, these studies are typically costly to conduct, and the ice conditions are uncontrollable. Laboratory physical modeling techniques are well-established, but remain expensive, and the model ice properties need to be improved.

Frequently, research studies are carried out by combining physical tests and theoretical/numerical calculations, each of which offer their unique advantages. Physical tests can provide phenomenological information on the behavior of the ice and the structure that is useful in view of the complexities of the dynamic process and the material properties of ice. Numerical simulations are relatively cost effective and easier to conduct, and extensive parametric studies can be conducted with respect to both the ice and structural parameters, where the numerical results can be calibrated and validated using physical test data.

Using the experiences obtained from full- and model-scale tests and connecting the elements of the icebreaking process using various hull ice load and propulsion models, the phenomena of icebreaking can be very well reproduced using semi-empirical numerical procedures. These semi-empirical time domain simulations can be used to supplement existing design methods by treating the problem holistically while retaining the physical bases of the elements of the detailed ship–ice interaction.

3

Numerical Procedure

The numerical procedure was developed and further improved in appended papers 1 and 2. In appended paper 1, a 6-DOF model for the continuous-mode icebreaking of a ship was developed, and the effect of the ship motions on the ship performance in level ice was investigated. The pressure–area relation was also explored. The numerical procedure was improved in appended paper 2 by implementing a failure criterion for wedge-shaped ice subjected to a dynamic loading, which was used to calculate the speed dependence of the motions and the bare hull ice resistance.

3.1 Underlying assumptions and simplifications

1) The force superposition principle was followed, i.e., the ice floes were assumed to be cleared by the advancing hull immediately after being broken away from the intact ice sheet; thus, the resistance arising from the ice floe clearing and submersion was considered not to interfere with subsequent contacts. Thus, this component, which is denoted by R_{sbmg}, could be separated from the total resistance. Similarly, the open water resistance, R_{ow}, could also be separated from the total resistance. Finally, the expression for the total resistance of ships in ice was written as follows:

$$R_{\mathrm{T}} = \underbrace{R_{\mathrm{brk}} + R_{\mathrm{sbmg}}}_{R_{\mathrm{I}}} + R_{\mathrm{ow}} \tag{3.1},$$

   where R_{brk} is the icebreaking component that accrues through crushing until bending failure occurs.

2) The numerical procedure was used to calculate R_{brk}, which was assumed to determine the dynamic behavior of the icebreaking process, from the contact conditions between the ship's icebreaking waterline and ice edge; R_{sbmg}, which was assumed to primarily produce a quasi-static force, was calculated as a global load using the empirical formula developed by Lindqvist (1989).

3) The ship's maneuvering coefficients (**M**, **A**, **B**, and **C** in Eq. (3.7)) were calculated prior to conducting the numerical runs using a 3-D boundary element program and assuming a low wave frequency: these coefficients were held constant during a numerical run. Linear hydrodynamic damping was not included, i.e., $\mathbf{B} = \mathbf{0}$, because in ice covered waters the ice load is considered to be the primary source of energy consumption.

4) The process of icebreaking was idealized as series of successive contact–crushing–bending cycles.

5) Crushing failure was considered the only local failure mode in ice, although physical tests have shown that shearing or flaking can also occur (Matlock et al., 1971; Riska, 1995; Tuhkuri, 1996).

3.2 Reference frames

Two right-handed Cartesian reference frames were employed to describe the rigid body motion of the ship and the geometry of the ice edge: an Earth-fixed, inertial frame and a ship body-fixed frame (Fig. 3.1).

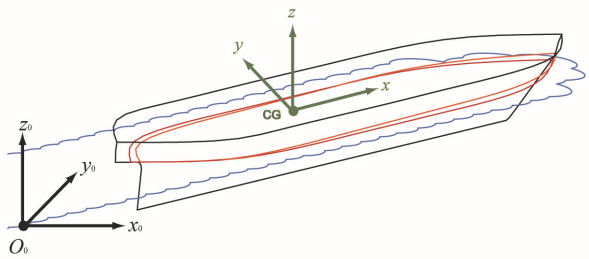

Fig. 3.1 Reference frames

The trajectory of the ship and the ice edge geometry were expressed with respect to the Earth-fixed reference frame, which was denoted by $\boldsymbol{x_0 y_0 z_0}$. The coordinate plane, $\boldsymbol{x_0 O_0 y_0}$, coincided with the calm water plane, with the $\boldsymbol{z_0}$ axis pointing upwards. The hydrodynamic properties and inertial coefficients of the ship were constant with respect to the coordinate system that was parallel to the principal axes of inertia of the ship: therefore, a body-fixed reference frame, $\boldsymbol{xyz}$, was introduced in which the origin was aligned with the center of gravity (**CG**) of the ship and body axes $\boldsymbol{x}$, $\boldsymbol{y}$, $\boldsymbol{z}$ corresponded to the longitudinal, transverse and vertical coordinates, respectively. The linear and angular velocities and the accelerations of the ship were expressed in the body-fixed reference frame.

The two reference frames were related via the following matrix transformation:

$$\boldsymbol{a}^0 = \boldsymbol{u} + \mathbf{R}_b^0(\boldsymbol{\Theta})\boldsymbol{a}^b \tag{3.2}$$

where $\boldsymbol{a}^0$ and $\boldsymbol{a}^b$ are the expressions of an arbitrary vector, $\boldsymbol{a}$, in $\boldsymbol{x}_0\boldsymbol{y}_0\boldsymbol{z}_0$ and $\boldsymbol{xyz}$, respectively; $\boldsymbol{u}$ is the translational vector from **CG** to $\boldsymbol{O}_0$; and $\mathbf{R}_b^0(\boldsymbol{\Theta})$ is the rotation matrix from $\boldsymbol{xyz}$ to $\boldsymbol{x}_0\boldsymbol{y}_0\boldsymbol{z}_0$.

The rotation matrix, $\mathbf{R}_b^0(\boldsymbol{\Theta})$, was defined following Fossen (2011):

$$\mathbf{R}_b^0(\boldsymbol{\Theta}) = \begin{bmatrix} c\theta c\psi & -c\phi s\psi + s\phi s\theta c\psi & s\phi s\psi + c\phi s\theta c\psi \\ c\theta s\psi & c\phi c\psi + s\phi s\theta s\psi & -s\phi c\psi + c\phi s\theta s\psi \\ -s\theta & s\phi c\theta & c\phi c\theta \end{bmatrix} \tag{3.3}$$

where

$$\boldsymbol{\Theta} = [\phi, \theta, \psi] \tag{3.4}$$

which denotes the Euler angles for: roll (ϕ), pitch(θ) and yaw(ψ); "c" in Eq. (3.3) denotes "cos", and "s" denotes "sin".

The relationship between the body-fixed angular velocity ($\boldsymbol{\omega}_{b/0}^b$) and the Euler rate ($\dot{\boldsymbol{\Theta}}$) was given by the following matrix transformation:

$$\dot{\boldsymbol{\Theta}} = \mathbf{T}(\boldsymbol{\Theta})\boldsymbol{\omega}_{b/0}^b \tag{3.5}$$

where

$$\mathbf{T}(\boldsymbol{\Theta}) = \begin{bmatrix} 1 & \sin\phi\tan\theta & \cos\phi\tan\theta \\ 0 & \cos\phi & -\sin\phi \\ 0 & \sin\phi / \cos\theta & \cos\phi / \cos\theta \end{bmatrix} \tag{3.6}$$

3.3 Ship rigid body dynamics

During the continuous-mode icebreaking process, the ship experiences rigid body motions in 6 DOFs that are governed by the following dynamic equations of motion:

$$(\mathbf{M} + \mathbf{A})\ddot{\mathbf{r}} + \mathbf{B}\dot{\mathbf{r}} + \mathbf{C}\mathbf{r} = \mathbf{F} \tag{3.7}$$

where **M**, **A**, **B** and **C** are the mass, added mass, linear damping, and hydrostatic restoring force matrices; **F** is the excitation force and moment vector that is the sum of the following components: the icebreaking forces and moments $\mathbf{F}_{brk}$, the ice

floe turning and submerging component $\mathbf{F}_{\text{sbmg}}$, drag forces from the water $\mathbf{F}_{\text{water}}$, and propulsion and steering forces $\mathbf{F}_{\text{p}}$. For a body with a principal plane of symmetry, these maneuvering coefficient matrices have the following forms with respect to the ship's **CG** (e.g., Faltinsen, 1990):

$$\mathbf{M} = \begin{bmatrix} m & 0 & 0 & 0 & 0 & 0 \\ 0 & m & 0 & 0 & 0 & 0 \\ 0 & 0 & m & 0 & 0 & 0 \\ 0 & 0 & 0 & I_{44} & 0 & -I_{46} \\ 0 & 0 & 0 & 0 & I_{55} & 0 \\ 0 & 0 & 0 & -I_{46} & 0 & I_{66} \end{bmatrix} \tag{3.8}$$

$$\mathbf{A}(\text{or } \mathbf{B}) = \begin{bmatrix} A_{11} & 0 & A_{13} & 0 & A_{15} & 0 \\ 0 & A_{22} & 0 & A_{24} & 0 & A_{26} \\ A_{31} & 0 & A_{33} & 0 & A_{35} & 0 \\ 0 & A_{42} & 0 & A_{44} & 0 & A_{46} \\ A_{51} & 0 & A_{53} & 0 & A_{55} & 0 \\ 0 & A_{62} & 0 & A_{64} & 0 & A_{66} \end{bmatrix} \tag{3.9}$$

$$\mathbf{C} = \begin{bmatrix} 0 & 0 & 0 & 0 & 0 & 0 \\ 0 & 0 & 0 & 0 & 0 & 0 \\ 0 & 0 & C_{33} & 0 & C_{35} & 0 \\ 0 & 0 & 0 & C_{44} & 0 & 0 \\ 0 & 0 & C_{53} & 0 & C_{55} & 0 \\ 0 & 0 & 0 & 0 & 0 & 0 \end{bmatrix} \tag{3.10}$$

The general acceleration, velocity, and global position and orientation vectors of the ship's **CG** are denoted as follows:

$$\begin{aligned} \ddot{\mathbf{r}} &= [\dot{u}, \dot{v}, \dot{w}, \dot{p}, \dot{q}, \dot{r}] \\ \dot{\mathbf{r}} &= [u, v, w, p, q, r] \\ \mathbf{r} &= [x, y, z, \phi, \theta, \psi] \end{aligned} \tag{3.11}$$

where the components are organized in the order of surge, sway, heave, roll, pitch, and yaw. This order is followed for the vectors used throughout this thesis.

A numerical solution to Eq. (3.7) was obtained using the "Newmark–beta" step-by-step time integration method (e.g., Langen and Sigbjornsson, 1977), where the accelerations of the ship were assumed to vary linearly during each time step.

The acceleration at the time instant τ in the (k+1)th time step, $\ddot{\mathbf{r}}^{\text{k}}(\tau)$, was given as follows:

$$\ddot{\mathbf{r}}^{\text{k}}(\tau) = \ddot{\mathbf{r}}_{\text{k}}^{\text{k}} + (\ddot{\mathbf{r}}_{\text{k+1}}^{\text{k}} - \ddot{\mathbf{r}}_{\text{k}}^{\text{k}}) \frac{\tau}{h} \tag{3.12}$$

where h is the length of the time step; the subscripts indicate the time step; and the superscripts indicate the reference frame in which the vector is expressed.

Integrating Eq. (3.12) over time yields the incremental velocity:

$$\Delta\dot{\mathbf{r}}^{\mathrm{k}}(\tau) = \int_0^{\tau} \ddot{\mathbf{r}}^{\mathrm{k}}(\xi)\mathrm{d}\xi = \ddot{\mathbf{r}}_{\mathrm{k}}^{\mathrm{k}}\tau + (\ddot{\mathbf{r}}_{\mathrm{k+1}}^{\mathrm{k}} - \ddot{\mathbf{r}}_{\mathrm{k}}^{\mathrm{k}})\frac{\tau^2}{2h} \tag{3.13}$$

Thus, the velocity at the time instant τ in the (k+1)th time step could be expressed as follows:

$$\dot{\mathbf{r}}^{\mathrm{k}}(\tau) = \dot{\mathbf{r}}_{\mathrm{k}}^{\mathrm{k}} + \Delta\dot{\mathrm{r}}^{\mathrm{k}}(\tau) = \dot{\mathbf{r}}_{\mathrm{k}}^{\mathrm{k}} + \ddot{\mathbf{r}}_{\mathrm{k}}^{\mathrm{k}}\tau + (\ddot{\mathbf{r}}_{\mathrm{k+1}}^{\mathrm{k}} - \ddot{\mathbf{r}}_{\mathrm{k}}^{\mathrm{k}})\frac{\tau^2}{2h} \tag{3.14}$$

The displacement was obtained using a similar procedure:

$$\mathbf{r}^{\mathrm{k}}(\tau) = \mathbf{r}_{\mathrm{k}}^{\mathrm{k}} + \int_0^{\tau} \dot{\mathbf{r}}^{\mathrm{k}}(\xi)\mathrm{d}\xi = \dot{\mathbf{r}}_{\mathrm{k}}^{\mathrm{k}}\tau + \ddot{\mathbf{r}}_{\mathrm{k}}^{\mathrm{k}}\frac{\tau^2}{2} + (\ddot{\mathbf{r}}_{\mathrm{k+1}}^{\mathrm{k}} - \ddot{\mathbf{r}}_{\mathrm{k}}^{\mathrm{k}})\frac{\tau^3}{6h} \tag{3.15}$$

By allowing $\tau = h$, the velocity and displacement at the end of each time step were obtained as:

$$\dot{\mathbf{r}}_{\mathrm{k+1}}^{\mathrm{k}} = \dot{\mathbf{r}}_{\mathrm{k}}^{\mathrm{k}} + (\ddot{\mathbf{r}}_{\mathrm{k}}^{\mathrm{k}} + \ddot{\mathbf{r}}_{\mathrm{k+1}}^{\mathrm{k}})\frac{h}{2} \tag{3.16}$$

$$\mathbf{r}_{\mathrm{k+1}}^{\mathrm{k}} = \mathbf{r}_{\mathrm{k}}^{\mathrm{k}} + \dot{\mathbf{r}}_{\mathrm{k}}^{\mathrm{k}}h + \ddot{\mathbf{r}}_{\mathrm{k}}^{\mathrm{k}}\frac{h^2}{3} + \ddot{\mathbf{r}}_{\mathrm{k+1}}^{\mathrm{k}}\frac{h^2}{6} \tag{3.17}$$

Requiring that the system attained equilibrium at the end of each time step yielded the following expression:

$$(\mathbf{M} + \mathbf{A})\ddot{\mathbf{r}}_{\mathrm{k+1}}^{\mathrm{k}} + \mathbf{B}\dot{\mathbf{r}}_{\mathrm{k+1}}^{\mathrm{k}} + \mathbf{C}\mathbf{r}_{\mathrm{k+1}}^{\mathrm{k}} = \mathbf{F}_{\mathrm{k+1}}^{\mathrm{k}} \tag{3.18}$$

The dynamic equations of motion, i.e., Eqs. (3.16)–(3.18), were then solved. The resulting solution corresponded to the incremental displacement:

$$\Delta\mathbf{r}_{\mathrm{k+1}}^{\mathrm{k}} = \dot{\mathbf{r}}_{\mathrm{k}}^{\mathrm{k}}h + \ddot{\mathbf{r}}_{\mathrm{k}}^{\mathrm{k}}\frac{h^2}{3} + (\mathbf{M} + \mathbf{A})^{-1}(\mathbf{F}_{\mathrm{k+1}}^{\mathrm{k}} - \mathbf{C}\mathrm{r}_{\mathrm{k+1}}^{\mathrm{k}})\frac{h^2}{6} \tag{3.19}$$

Finally, the state variables were updated and used as initial values for the next time step as follows:

$$\ddot{\mathbf{r}}_{\mathrm{k+1}}^{\mathrm{k}} = \frac{6}{h^2}(\Delta\mathbf{r}_{\mathrm{k+1}}^{\mathrm{k}} - \dot{\mathbf{r}}_{\mathrm{k}}^{\mathrm{k}}h - \ddot{\mathbf{r}}_{\mathrm{k}}^{\mathrm{k}}\frac{h^2}{3}) \tag{3.20}$$

$$\dot{\mathbf{r}}_{\mathrm{k+1}}^{\mathrm{k}} = \dot{\mathbf{r}}_{\mathrm{k}}^{\mathrm{k}} + \Delta\dot{\mathbf{r}}_{\mathrm{k+1}}^{\mathrm{k}} \tag{3.21}$$

$$\mathbf{r}_{\mathrm{k+1}}^{\mathrm{k}} = \mathbf{r}_{\mathrm{k}}^{\mathrm{k}} + \Delta\mathbf{r}_{\mathrm{k+1}}^{\mathrm{k}} \tag{3.22}$$

3.4 Icebreaking load model

In the numerical procedure, the icebreaking (i.e., crushing and bending) force component, $\mathbf{F}_{brk}$, directly caused the formation of the icebreaking pattern and was calculated by integrating the contact forces over the icebreaking waterline. The methodology for this procedure is introduced in this section.

3.4.1 Ship hull geometry

Fig. 3.2 presents the ship's hull geometry that formed the rigid body boundary condition for the ice edge in the icebreaking process. The ship hull lines were modeled by spline interpolation based on the lines drawing. The variation in the icebreaking waterline because of the rigid body motions of the ship with 6 DOFs was included by solving for the intersection curve between the ship hull and the water plane at each time step.

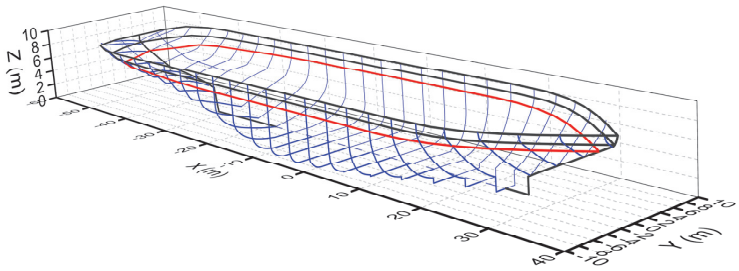

Fig. 3.2 Ship geometry model

Computational geometry principles (e.g., Farin, 1997) were applied to develop a subroutine to discretize the waterline into nodes (Fig. 3.3). The ice edge was also discretized into nodes based on the ice edge shape from the previous time step or any given initial condition.

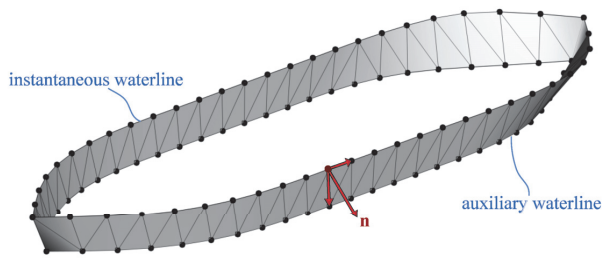

Fig. 3.3 Frame angle calculation

The frame angles, which are denoted by φ, on the waterline nodes were calculated at each time step in compliance with the ship's motions in heave, roll and pitch. Fig. 3.3 presents the auxiliary waterline below the instantaneous icebreaking waterline that was created to facilitate the construction of the hull panels. For a sufficiently small hull panel (on the order of cm^2), the frame angle could be represented by the directional cosine between the normal to the hull, $\boldsymbol{n}$, and the vertical axis of each waterline node.

3.4.2 Contact detection

The possible contact zones between the ship hull and ice edge were identified by using a geometric argument, i.e., by detecting the overlap between the ship's icebreaking waterline and the ice edge, as shown in Fig. 3.4.

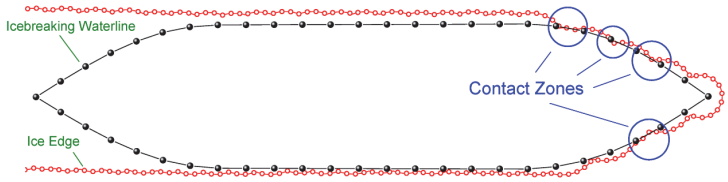

Fig. 3.4 Contact detection

The contact area, A_{cr}, for each contact zone was calculated by considering two types of contact interfaces with a flat hull at the contact point (Fig. 3.5).

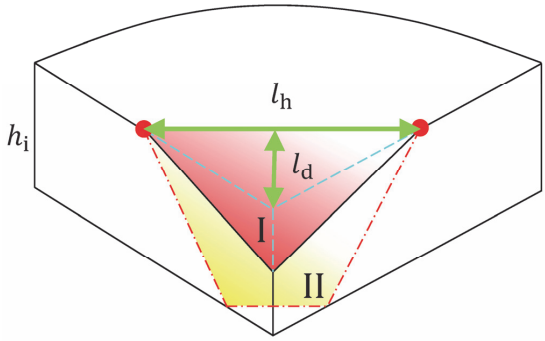

Fig. 3.5 Idealized contact interfaces

For each of the contact interface types, the contact area was described by the contact length, L_h, the indentation depth, L_d, and the frame angle, φ, as follows:

$$A_{\mathrm{cr}} = \begin{cases} \frac{1}{2} L_{\mathrm{h}} \frac{L_{\mathrm{d}}}{\cos\varphi} & , \quad L_{\mathrm{d}} \tan\varphi \le h_{\mathrm{i}} \quad \text{(type I)} \\ \frac{1}{2}\left(L_{\mathrm{h}} + L_{\mathrm{h}} \frac{L_{\mathrm{d}} - \frac{h_{\mathrm{i}}}{\tan\varphi}}{L_{\mathrm{d}}}\right), & L_{\mathrm{d}} \tan\varphi > h_{\mathrm{i}} \quad \text{(type II)} \end{cases} \tag{3.23}.$$

3.4.3 Contact pressure

The local crushing force on each contact zone was then calculated based on a model of the average contact pressure given by Riska (1995):

$$F_{\mathrm{cr}} = p_{\mathrm{av}} A_{\mathrm{cr}} \tag{3.24},$$

where the local crushing force, F_{cr}, was idealized as the product of the average contact pressure, p_{av}, and the contact area.

For simplicity, it is typically assumed that p_{av} can be represented by the crushing strength, σ_{cr}, of ice. However, many field observations and physical experiments have shown that p_{av} depends on the magnitude of the contact area, among other factors, such as the loading rate, temperature, and ice properties.

This dependence is commonly known as the pressure–area (p–a) relation. Analyses on full-scale measurements (e.g., Masterson and Frederking., 1993; Masterson et al., 2007) have shown that the p–a curves exhibit a power law form:

$$p_{\mathrm{av}} = k A_{\mathrm{cr}}^{n} \tag{3.25},$$

where k and n are empirical parameters, k is positive, and n is negative.

The effect of the average contact pressure and the evaluation of the p–a curves using the numerical procedure are discussed in Chapter 5.

3.4.4 Contact forces

A local coordinate system (Fig. 3.6), denoted by **τnz**, was introduced to transform the rigid body velocities with respect to the **CG** to the hull nodal velocities:

$$\mathbf{v}_{\mathrm{i}}^{\{\tau \mathrm{nz}\}} = \begin{bmatrix} v_{\tau} \\ v_{\mathrm{n}} \\ v_{\mathrm{z}} \end{bmatrix} = \begin{bmatrix} \cos\alpha_{\mathrm{i}} & -\sin\alpha_{\mathrm{i}} & 0 \\ \sin\alpha_{\mathrm{i}} & \cos\alpha_{\mathrm{i}} & 0 \\ 0 & 0 & 1 \end{bmatrix} \begin{bmatrix} v_{\mathrm{x}} \\ v_{\mathrm{y}} \\ v_{\mathrm{z}} \end{bmatrix} = \mathbf{M}(\alpha_{\mathrm{i}}) \cdot \mathbf{v}_{\mathrm{i}}^{\{\mathrm{ship}\}} \tag{3.26},$$

where α_{i} denotes the waterline angle at node i.

The velocities were then decomposed into components that were tangential (v_1) and normal (v_2) to the contact surface, as shown in Fig. 3.7.

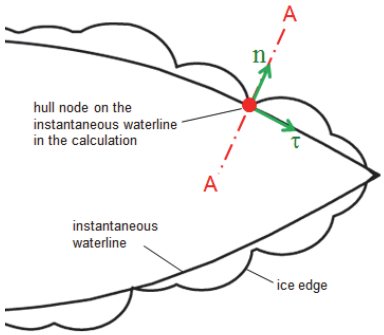

Fig. 3.6 Local coordinate system **τnz**

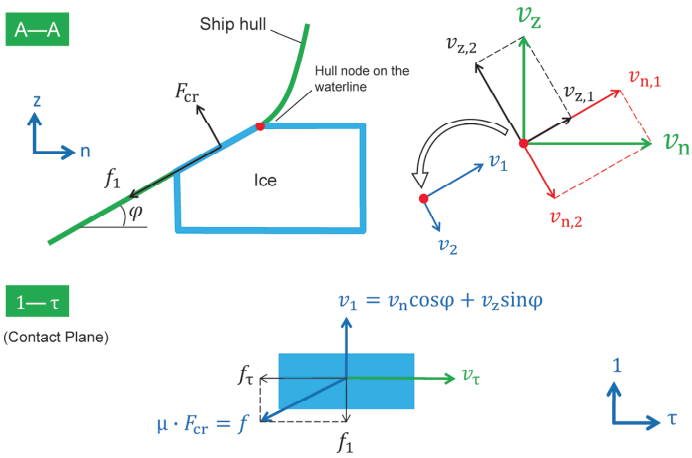

Fig. 3.7 Local contact forces

The nodal velocities were then expressed in vector form as follows:

$$\mathbf{v}_i^{\{\tau 12\}} = \begin{bmatrix} v_\tau \\ v_1 \\ v_2 \end{bmatrix} = \begin{bmatrix} 1 & 0 & 0 \\ 0 & \cos\varphi & \sin\varphi \\ 0 & \sin\varphi & -\cos\varphi \end{bmatrix} \begin{bmatrix} v_\tau \\ v_n \\ v_z \end{bmatrix} \tag{3.27}$$

The magnitude of the crushing force, F_{cr}, which was caused by v_2, and developed in Section 3.4.3, could be expressed in vector form as follows:

$$F_{cr} = \begin{cases} -p_{av}A_{cr}, & v_2 \le 0 \\ 0, & v_2 > 0 \end{cases} \tag{3.28}$$

where the negative sign indicates that the force was always in the opposite direction to that of v_2.

In the contact plane (i.e., plane $\mathbf{1}-\boldsymbol{\tau}$ in Fig. 3.7), the tangential relative velocities, v_1 and v_τ, produced vertical and horizontal friction forces, which are denoted by f_1 and f_τ, respectively:

$$f_1 = \mu F_{cr} \frac{v_1}{\sqrt{v_\tau^2 + v_1^2}} \tag{3.29}$$

$$f_\tau = \mu F_{cr} \frac{v_\tau}{\sqrt{v_\tau^2 + v_1^2}} \tag{3.30}$$

The nodal force on the ship hull in **τnz** could then be obtained as

$$\mathbf{F}_i^{\{\tau nz\}} = \begin{bmatrix} F_\tau \\ F_n \\ F_z \end{bmatrix} = \begin{bmatrix} 1 & 0 & 0 \\ 0 & \cos\varphi & \sin\varphi \\ 0 & \sin\varphi & -\cos\varphi \end{bmatrix} \begin{bmatrix} f_\tau \\ f_1 \\ F_{cr} \end{bmatrix} \tag{3.31}$$

Finally, the forces in **τnz**, $\mathbf{F}_i^{\{\tau nz\}}$, were transformed back to the ship's reference system as follows:

$$\mathbf{F}_i^{\{ship\}} = \mathbf{M}^{-1}(\alpha_i) \cdot \mathbf{F}_i^{\{\tau nz\}} \tag{3.32}$$

The sum contact load on the ship was then obtained by integrating $\mathbf{F}_i^{\{ship\}}$ over all of the contact zones that acted on the ship simultaneously.

3.4.5 Bending failure criterion

The normal crushing force on the ice edge, which is denoted by F'_{cr}, together with the vertical frictional force, which is denoted by f'_1, result in a vertical force component, F'_z:

$$F'_z = -(F'_{cr}\cos\varphi - f'_1 \sin\varphi) \tag{3.33}$$

As the ship penetrates further into the ice, the contact area and thus the contact forces increase. This process continues until F'_z exceeds the bearing capacity, P_f, of the ice edge.

Tan et al. (2012) (appended paper 1) used a numerical procedure into which a static bending failure criterion was incorporated; the static bending failure criterion was developed by Kashtelyan (Kerr, 1975) from observations:

$$P_f^{static} = c_f \sigma_f h_i^2 \left(\frac{\theta_w}{\pi}\right)^2 \tag{3.34}$$

where c_f is an empirical coefficient that is determined by field tests; σ_f is the flexural strength of the ice; and θ_w is the ice wedge opening angle at the vertex.

In a subsequent case study presented in appended paper 2, the numerical procedure was improved by incorporating a dynamic bending failure criterion because both experimental and theoretical studies (e.g., Varsta, 1983; Valanto, 1989; Valanto, 1992) have indicated that the bending failure load of an ice wedge subjected to a rapid loading increases with the indentation speed. The inertial force of the ice and the hydrodynamics of the water foundation, which are associated with the loading rate, affect the ice bending failure load.

The dynamic bending failure criterion was developed based on the finite element calculations of the dynamic bending failure loads for level ice provided by Varsta (1983), as shown in Fig. 3.8.

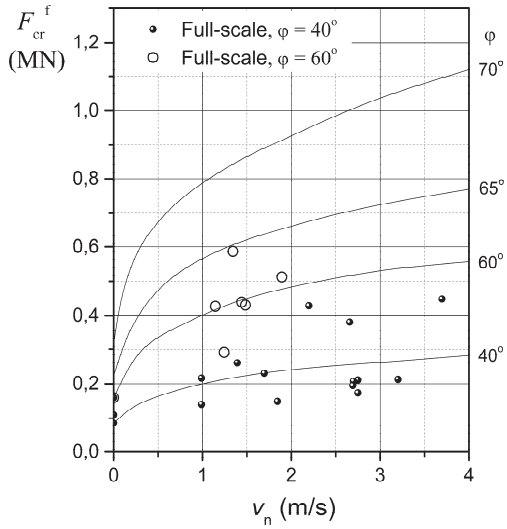

Fig. 3.8 Normal crushing force at failure vs. ship forward speed (reproduced from Varsta (1983): notations for force, speed and frame angle were changed to be consistent with this study)

Geometrical relations between the force and velocity components and dimensional analysis were used to obtain a dimensionless coefficient function of the normal relative speed:

$$\lambda_t(v_2) = \frac{P_f(v_2)}{\sigma_f h_i^2 (\frac{\theta_w}{\pi})^2} \quad (3.35),$$

which is plotted in Fig. 3.9.

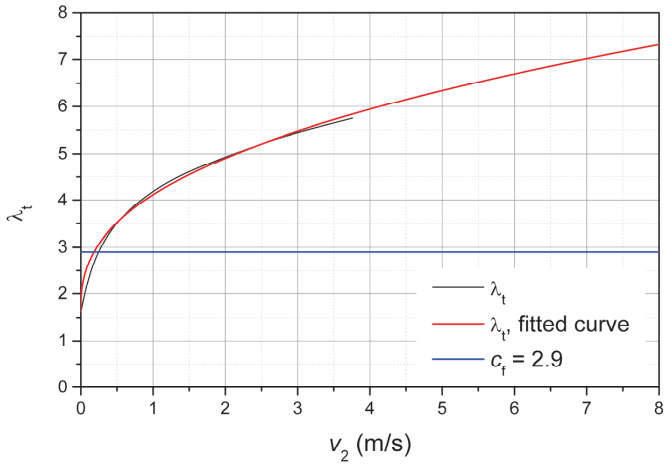

Fig. 3.9 Coefficient λ_t as a function of crushing speed v_2 ($h_i = 0.35$ m, $\sigma_f = 1.2$ MPa, $\theta_w = 90°$)

The numerical expression for λ_t was obtained by curve fitting, as shown in Fig. 3.9, which was then used to incorporate the dynamic effect described by Eq. (3.35) into the bending failure load:

$$P_f(v_2) = (1.65 + 2.47v_2^{0.40})\sigma_f h_i^2 (\frac{\theta_w}{\pi})^2 \quad (3.36).$$

3.4.6 Bending crack

Model- and full-scale observations have shown that the failure of an ice sheet by bending and the emergence of a new ice edge follows a seemingly regular pattern consisting of wedge- and cusp-shaped ice pieces that sequentially break off from the intact ice field.

In the numerical procedure, the shape of the bending crack was idealized as a circular arc. In Tan et al. (2013) (appended paper 1), the size of the broken ice floe was represented by the "ice floe radius" that was developed by Wang (2001), which can be expressed as:

$$R = C_l l(1 + C_v v_2) \quad (3.37),$$

where v_2 is the normal crushing speed, as shown in Fig. 3.7; l is the characteristic length of ice; and C_l and C_v are two empirical parameters.

Using static theory for an elastic plate on an elastic foundation yielded the following solution for l:

$$l = \left(\frac{Eh_i^3}{12(1-\nu^2)\rho_w g}\right)^{\frac{1}{4}} \quad (3.38).$$

The ice edge that is in contact with the hull can take quite irregular shapes, which can be observed in the icebreaking patterns in nature and was observed in the numerical simulations. The "ice floe radius" model given by Eq. (3.37) specifies only one dimension (the radial direction, or depth) of the broken floe. In a subsequent study described in appended paper 2, an additional condition was used together with Eq. (3.37) to describe the geometry for which the ice cover fails. Based on reports from full-scale tests, Milano (1973) suggested that the ratio between the length (denoted as $c_2 l$ in Fig. 3.10) and the depth (denoted as $c_1 l$ in Fig. 3.10) of the cusp for sea ice ranged from approximately 3.0 to 6.0.

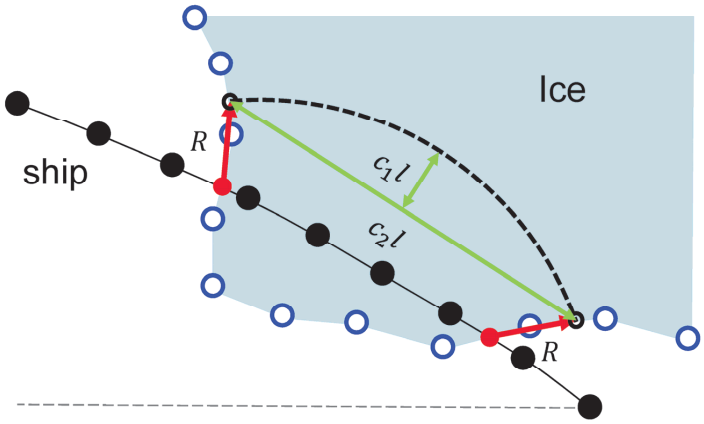

Fig. 3.10 Example of bending crack

Therefore, the following coefficient, C_r, was defined:

$$C_r = \frac{c_2 l}{c_1 l} \quad (3.39),$$

and was introduced into the numerical procedure to represent the length-to-depth ratio of the broken ice cusp.

The sequence of the geometry of the ice edge created by repeated breaking is often referred to as the "icebreaking pattern". Fig. 3.11 provides an example of the icebreaking pattern observed in an ice model test. Fig. 3.12(a) presents a simulated icebreaking pattern. A comparison of the observed and simulated icebreaking patterns illustrates that the numerical procedure reproduced the icebreaking process well.

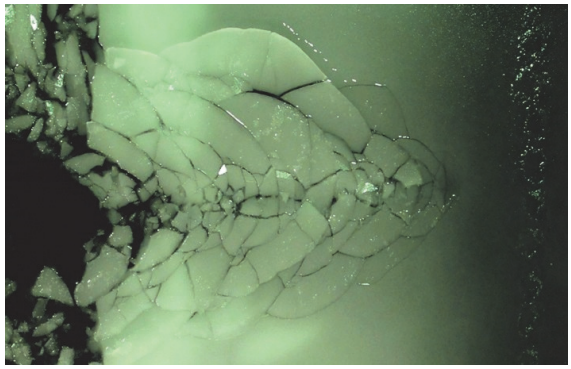

Fig. 3.11 Observed icebreaking pattern for the bow of the M/T Uikku in Aalto ice tank in Feb., 2012 (Photograph by X. Tan)

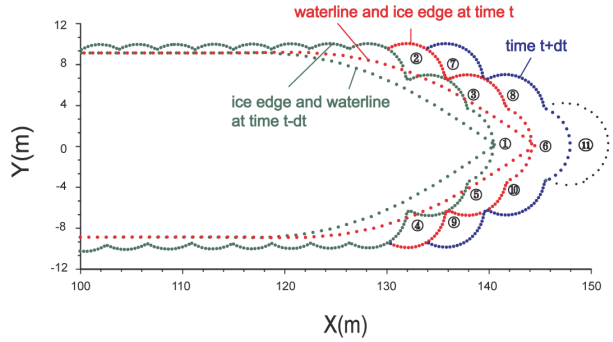

(a)

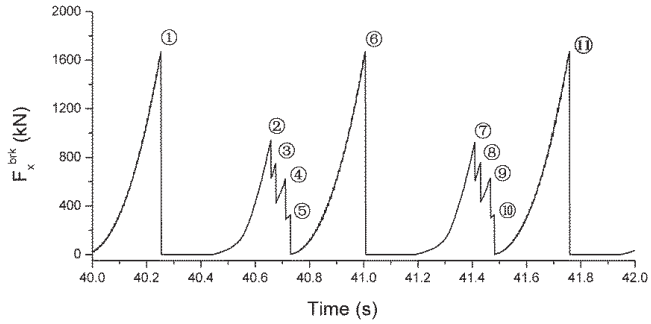

(b)

Fig. 3.12 (a) Simulated icebreaking pattern and (b) corresponding icebreaking force

3.5 Propulsion force

The concept of the net thrust in ice, T_{net}, i.e., the thrust available to overcome the ice resistance after considering the thrust used to overcome the open water resistance, was incorporated into the numerical model to represent the propulsion force for self-propulsion conditions.

The net thrust in ice was defined as:

$$T_{\mathrm{net}} = T_{\mathrm{T}} \cdot (1 - t_{\mathrm{ow}}) - R_{\mathrm{ow}}^{[\mathrm{h}]} \tag{3.40},$$

where T_{T} is the total thrust; t_{ow} is the open water thrust deduction factor; and $R_{\mathrm{ow}}^{[\mathrm{h}]}$ is the bare hull open water resistance.

In early designs, the effect of the speed in Eq. (3.40) was approximated by the quadratic factor $f_{\mathrm{v}}(u)$ (Riska et al., 1997), which depended on the maximum open water speed, as follows:

$$T_{\mathrm{net}}(u) = f_{\mathrm{v}}(u) \cdot T_{\mathrm{B}} = (1 - \frac{1}{3} \cdot \frac{u}{v_{\mathrm{ow}}} - \frac{2}{3} \cdot (\frac{u}{v_{\mathrm{ow}}})^2) \cdot T_{\mathrm{B}} \tag{3.41},$$

where T_{B} is the bollard pull; and v_{ow} is the maximum open water speed.

Eq. (3.41) illustrates that T_{net} equals the bollard pull when the ship speed is zero, and T_{net} equals zero when the ship is at the maximum open water speed.

The actual total thrust, T_{T}, derived from the propeller open water tests was used in paper 3. For papers 1 and 2, Eq. (3.41) was used to describe the propulsion force.

3.6 Coupling between ship motions and excitation forces

Once the ice edge has broken away from the intact ice sheet, a new ice edge is generated and the next icebreaking cycle begins. Eq. (3.19) illustrates that the ship's current state variables and the environmental loads are interdependent on each other. In the icebreaking process, the ship motions and icebreaking pattern affect each other simultaneously. The coupling between the ship motions and excitation forces was solved for iteratively at each time step until equilibrium was achieved. The following convergence criterion was used:

$$\frac{\left\| \mathbf{F}_{\mathrm{k+1}}^{(\mathrm{i+1})} - \mathbf{F}_{\mathrm{k+1}}^{(\mathrm{i})} \right\|_2}{\left\| \mathbf{F}_{\mathrm{k+1}}^{(\mathrm{i})} \right\|_2} \leq 10^{-3} \tag{3.42}.$$

A flowchart of the numerical procedure is provided in Fig. 3.13.

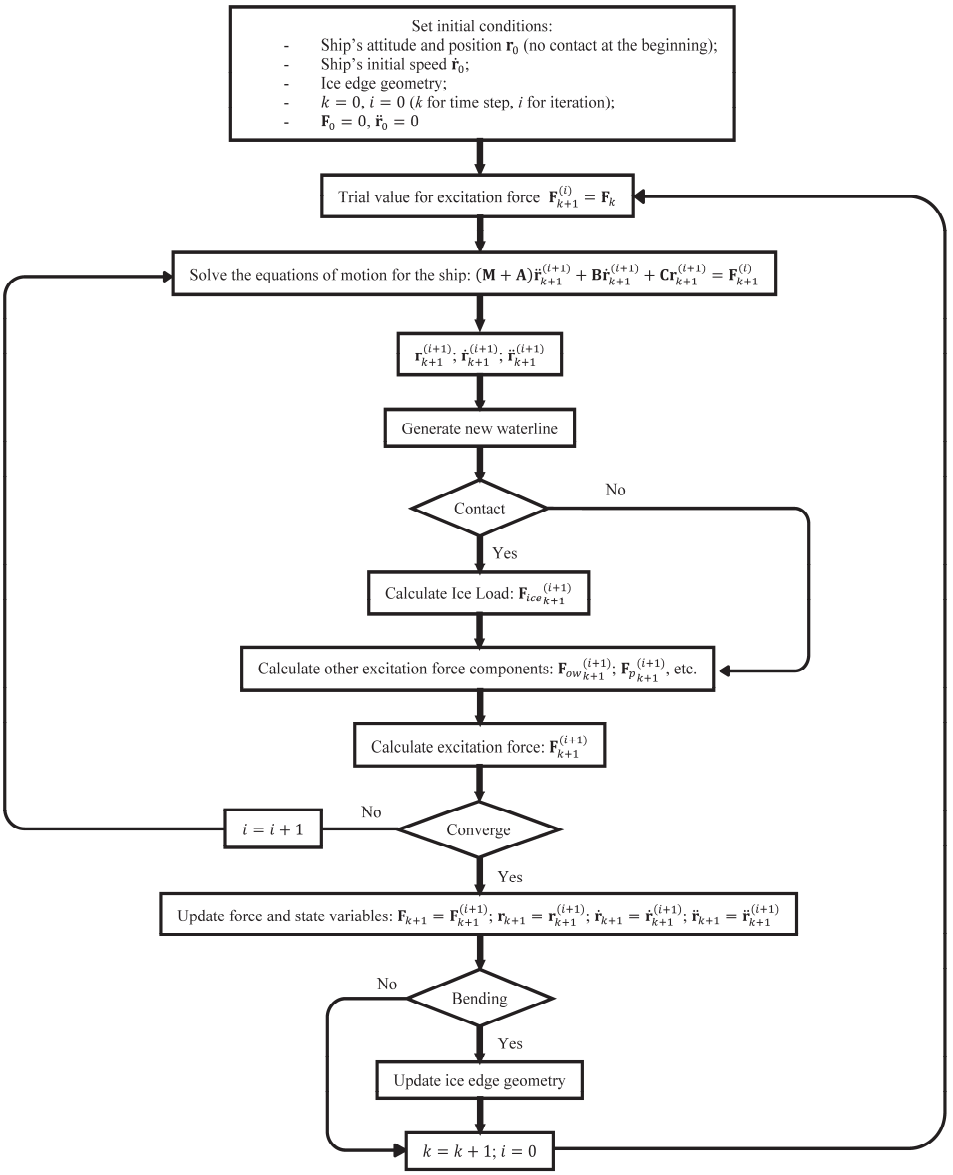

Fig. 3.13 Flowchart of the numerical procedure

4

Ship Motions, Icebreaking Pattern, and Ice Resistance

In this chapter, the effect of the interactions among the three key characteristics in the dynamic process of continuous icebreaking is discussed: the ship motions, icebreaking pattern, and ice resistance (ship performance). The corresponding paper on this issue is appended paper 1. When considering ship motions with 6 DOFs, variations in the waterline geometry and frame angle from the heave, pitch, and roll further complicate the relationships among these characteristics. The interdependencies between these characteristics are intricate and thus difficult to describe explicitly. The numerical model served as a tool for investing this complex problem by reproducing the icebreaking patterns and simulating the ship motions and ice resistance in the time domain. Case studies were conducted for the Swedish icebreaker AHTS/IB Tor Viking II. The results from three different DOF configurations were compared to the full-scale data to determine the relations among these characteristics. The *p*–*a* relation (Chapter 5) and the dynamic bending failure criterion for ice (Chapter 6) were not included thus far. The contact pressure was evaluated as the crushing strength of ice (σ_{cr}), and the static bending failure criterion developed by Kashtelyan (1968) (i.e., Eq.(3.34)) was used.

4.1 AHTS/IB Tor Viking II

The AHTS/IB Tor Viking II has a conventional propulsion system that consists of four medium speed diesel engines connected with two reduction gears into two CP-propellers equipped with nozzles. The ship's full-scale parameters are provided in Table 4.1. A full-scale test series was conducted on the Tor Viking II in the northernmost Baltic in winter 2000; the tests consisted of on-ice measurements of ice properties and thicknesses (Riska et al., 2001).

In this thesis, the values of the ship and ice parameters that are listed in Table 4.1 and Table 4.2 were used as inputs for all of the case studies on the Tor Viking II.

Table 4.1 Ship parameters

Parameter	Notation	Value	Dimension
Length over all	LOA	83.70	m
Length between perpendiculars	Lpp	75.20	m
Breath, moulded	B	18.00	m
Draught, max icebreaking	D	6.50	m
Bollard-pull, ahead	T_B	202	t
Displacement	M	5.74×10^6	kg
Moment of inertia	I_{xx}	2.98×10^8	kg . m^2
	I_{yy}	2.03×10^9	kg . m^2
Added mass coefficients	A_{33}	1.83×10^7	kg
	A_{44}	5.36×10^7	kg . m^2
	A_{55}	4.47×10^9	kg . m^2
Restoring force coefficients	C_{33}	1.31×10^7	N/m
	C_{44}	1.38×10^8	N . m
	C_{55}	6.09×10^9	N . m
Propulsion output	P_D	13440	kW
Open water speed	v_{ow}	16.40	knot

Table 4.2 Ice properties

Parameter	Notation	Value	Dimension
Density	ρ_i	880	kg/m^3
Young's modulus	E	5.40	GPa
Poisson ratio	ν	0.33	
Crushing strength	σ_{cr}	2.30	MPa
Bending strength	σ_f	0.58	MPa
Coefficient of friction	μ	0.15	

4.2 Motion configurations

The numerical procedure was developed to include various ship motion configurations. In addition to the 6-DOF ship motion model, reduced-order models could be generated by constraining any of the DOF(s) to investigate the effect of specific motion(s) on icebreaking. In this chapter, the following motion configurations are used:

- 6-DOF model – includes all motions in 6 DOFs;

- 4-DOF model – includes surge, heave, roll, and pitch; and
- 3-DOF model – a planar model that includes motions in surge, sway, and yaw.

The relationships between the motion configurations are shown in Fig. 4.1.

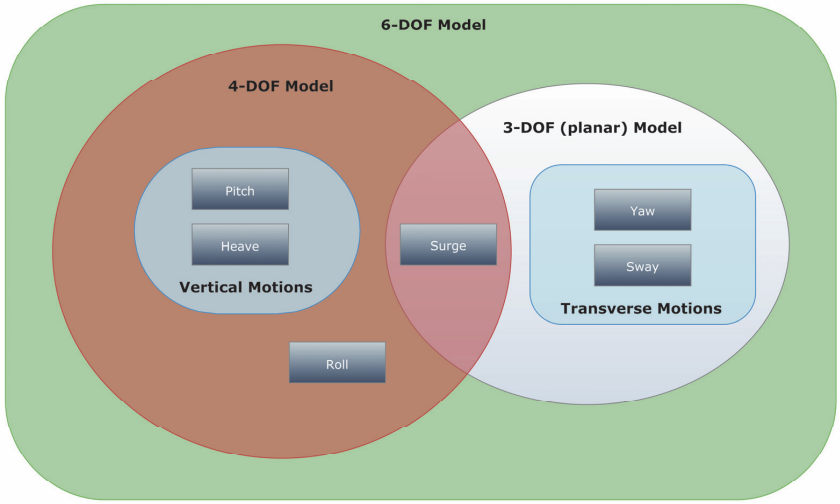

Fig. 4.1 Relationships between the motion configurations

4.3 Interaction between ship motions and the icebreaking pattern

Fig. 4.2 and Fig. 4.3 present typical simulation results for the ship motions and icebreaking patterns.

The loading conditions, including the loading rate, waterline geometry, and hull frame angle, are asymmetric on the two sides of the hull because of the ship motions, and this often drive the ship to drift transversely, as shown in Fig. 4.2(d) and Fig. 4.3(d).

The effect of the icebreaking pattern on the heave, pitch, and roll is determined by comparing these motions in Fig. 4.2 and Fig. 4.3: the more unevenly distributed ice pressure around the hull for 0.5-m-thick ice caused a larger vibration amplitude of these motions than that obtained for 0.6-m-thick ice, although the corresponding mean values were smaller.

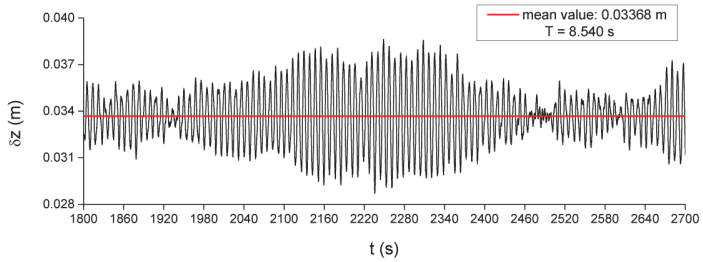

(a) Heave

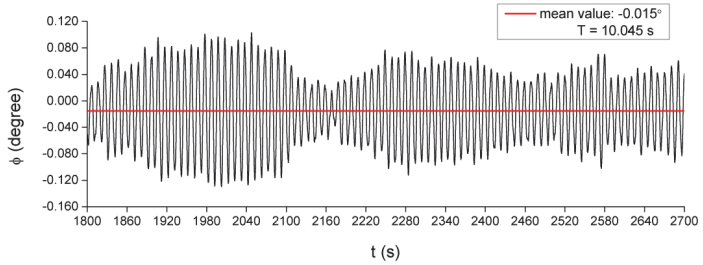

(b) Roll

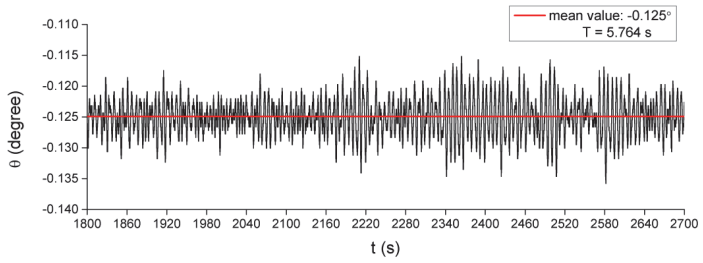

(c) Pitch

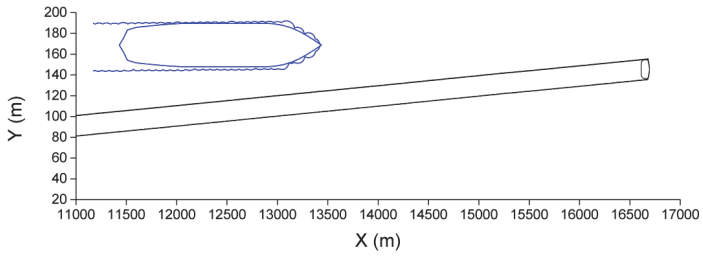

(d) Ship's course (not to scale) and icebreaking pattern

Fig. 4.2 Simulated ship motions and icebreaking pattern
(ice thickness: 0.6 m, full propulsion power, 6-DOF model)

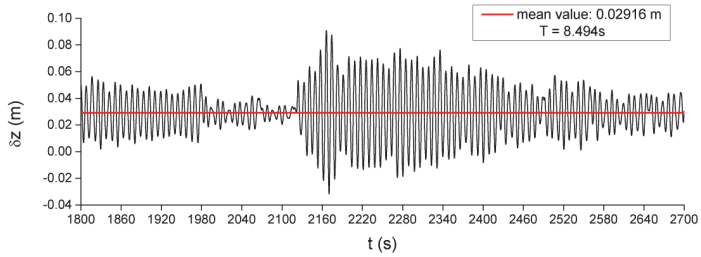

(a) Heave

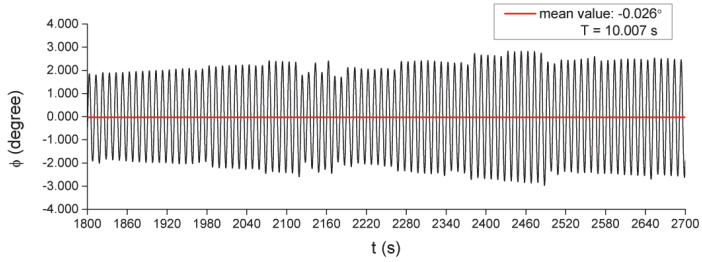

(b) Roll

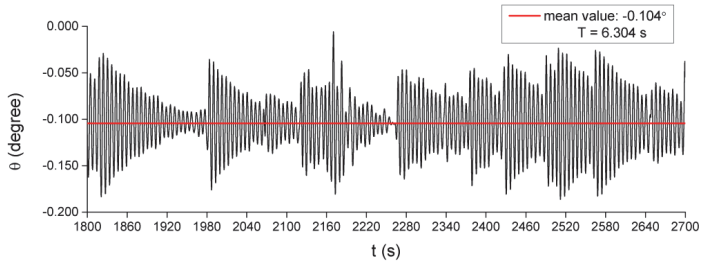

(c) Pitch

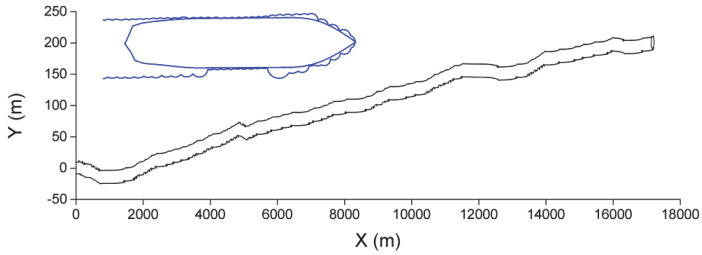

(d) Ship's course (not to scale) and icebreaking pattern

Fig. 4.3 Simulated ship motions and icebreaking pattern
(ice thickness: 0.5 m, full propulsion power, 6-DOF model)

The effect of the ship's transverse motions (sway and yaw) on the icebreaking pattern can be seen in the example shown in Fig. 4.4. The icebreaking pattern not only affected but was in turn affected by the inclusion of the sway and yaw motions.

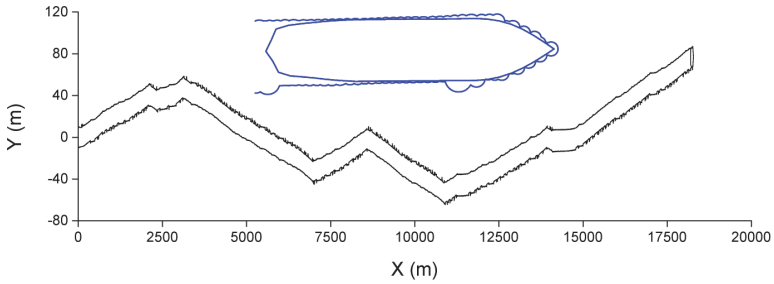

(a) 6-DOF model

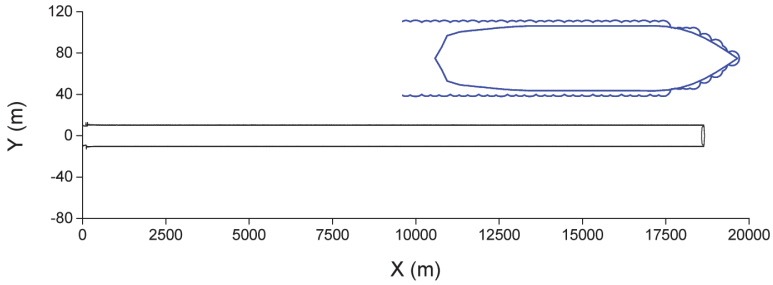

(b) 4-DOF model

Fig. 4.4 Comparison of the ship's course (not to scale) and icebreaking pattern for the 6- and 4-DOF models (ice thickness: 0.4 m, full propulsion power)

The effect of the heave and pitch on the icebreaking pattern was determined by comparing Fig. 4.5(a) and Fig. 4.5(b). Accounting for the heave and pitch in the model decreased the crushing on the side hull.

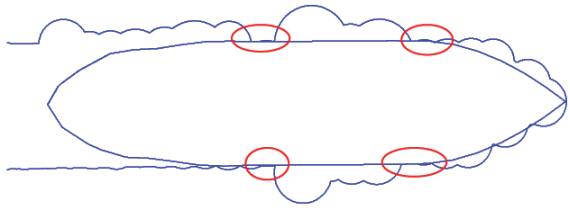

(a) 6-DOF model

(b) 3-DOF (planar) model

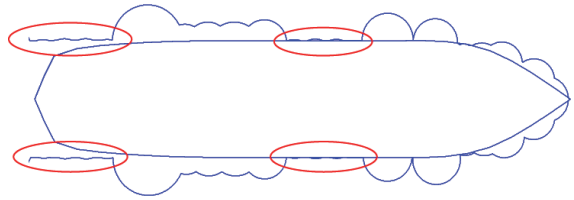

(c) 4-DOF model

Fig. 4.5 Icebreaking patterns for different motion configurations
(ice thickness: 0.7 m, full propulsion power)

4.4 Interaction between the ship motions and ship performance

4.4.1 Vertical motions (pitch and heave)

A ship's performance in ice is often described using a plot of the ice thickness versus the forward speed that can be attained at full propulsion power, i.e., the h–v curve (In the subsequent part of this thesis, v is used to denote the ship's forward speed instead of u that was defined in Chapter 3). Fig. 4.6 illustrates that the numerical predictions generally correlated well with the regression curve of the full-scale data.

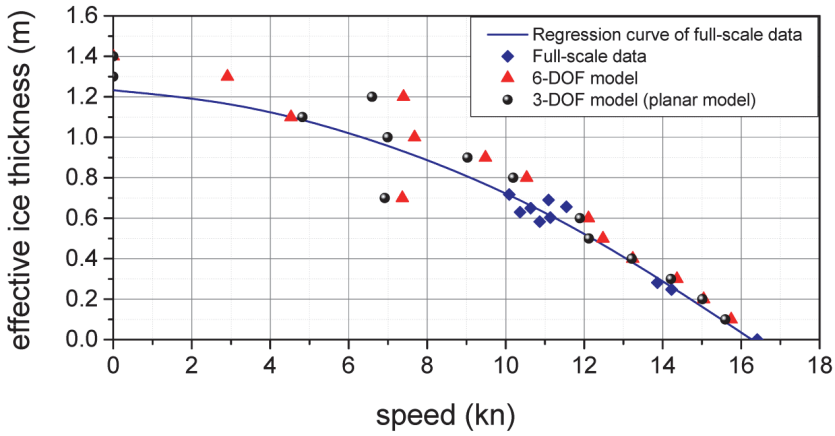

Fig. 4.6 h–v curve

Fig. 4.6 presents the numerical predictions obtained using the 6- and 3-DOF (planar) models. Comparing the results for these two motion configurations illustrates that the speeds predicted by the 6-DOF model are slightly higher than those obtained using the 3-DOF model for most of the ice thicknesses considered (except for the 1.1-m-thick ice) and that this result tended to be more obvious for thick ice. This implies that the inclusion of vertical motions is generally beneficial for icebreaking. This trend can be explained by the fact that a ship does not "plow through" ice when advancing in thick ice; instead, the ship drives its bow onto the ice to break the ice with its weight. Thus, this "ramming" process in thick ice involves relatively large motions of heave and, in particular, pitch. In thin ice, however, the bending strength of ice is low, and the ice typically breaks without a noticeable change in the ship's trim. From an energy perspective, this result also suggests that in the absence of artificial constraints for the 6-DOF model, the ship breaks ice such that the energy is optimized among the 6 DOFs.

4.4.2 Transverse motions (sway and yaw)

Fig. 4.7 compares the numerical predictions obtained using the 6- and 4-DOF models. For most of the cases in thick ice (except for the case in 1.0-m-thick ice), the speed predicted by the 4-DOF model was slightly higher than that predicted by the 6-DOF model. This result implies that, especially in thick ice, reciprocating sway and yaw causes an increase in ice resistance because of the enlarged forward project area of the ship. This phenomenon was less obvious in thin ice than in thick ice because the ice pressure is often more non-uniformly distributed around the

hull in thick ice, thereby causing the ship to yaw and sway. Furthermore, the 6-DOF model did not tend to yield a higher speed than the 4-DOF model from energy perspective, as noted in Section 4.4.1, because although the 6-DOF model has fewer artificial constraints and thus was more energy efficient compared to the 4-DOF model, the relieved DOFs in sway and yaw do not contribute as significantly to icebreaking as the vertical motions. Transverse motions can only cause difficulties in icebreaking because ice is more easily bent than crushed; for a typical icebreaking hull, vertical motions bend ice, whereas transverse motions crush ice. Thus this advantage in terms of the energy use offered by the 6-DOF model was canceled out by the added resistance resulting from the transverse motions.

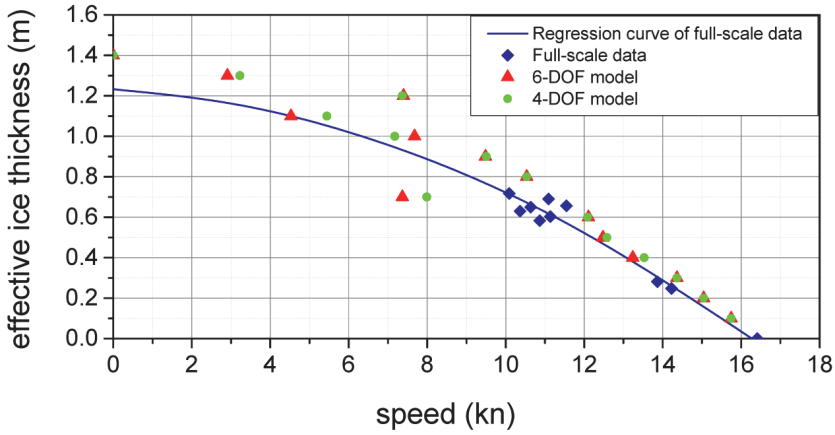

Fig. 4.7 h–v curve

4.4.3 Roll

The effect of roll on ice resistance is more complicated. Roll might be expected to resemble other reciprocating transverse motions (sway and yaw) that produce an enlarged forward project area and thus an added resistance. However, roll is also a motion with a vertical effect. That is, under some circumstances (e.g., when the bending strength of the ice is low and the slope at the side hull is considerably lower than 90°), rolling may also help to create a wider channel.

It was observed in the numerical calculations that when the bow opened a channel that was not sufficiently wide for the maximum beam to pass through, continuous crushing occurred along the side hull, thereby increasing the ice resistance. Moreover, if the ship experienced large rolling angles simultaneously, the ice edge around the midbody was constantly crushed instead of bent because of the large side hull slope angle of the Tor Viking II (90°). Large amplitudes of the roll motion

and correspondingly high values of ice resistance were reported in model tests conducted by Ettema et al. (1987).

4.5 Interaction between the icebreaking pattern and ship performance

Su (2011) investigated the effect of the icebreaking pattern on ship performance (ice resistance) in ice. The resistance depended on both the ice thickness and the icebreaking pattern: when shoulder crushing (e.g., Fig. 4.8) occurs constantly, the ship experiences a higher icebreaking resistance than when shoulder crushing is absent, even in relatively thin ice. In this study, similar occurrences of shoulder crushing were also observed. For example, in the case of 0.7-m-thick ice with the icebreaking patterns shown in Fig. 4.5 (where the shoulder crushing is encircled in red), the predicted speed was considerably lower than even that for thicker ice, as seen from the h–v curves.

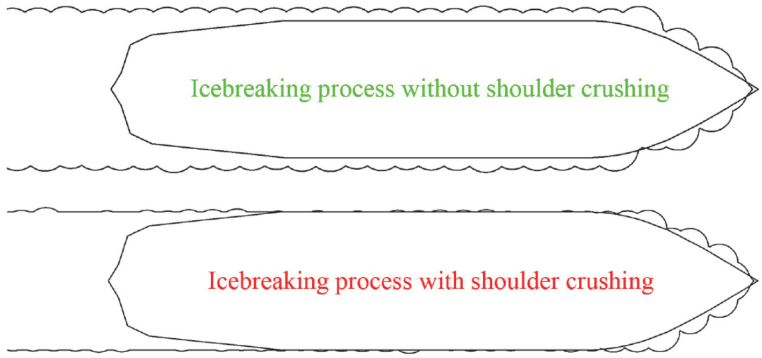

Fig. 4.8 Two different icebreaking patterns (Su, 2011)

5

Effect of the Average Contact Pressure

Studies on the average contact pressure are presented in this chapter. The corresponding content can be found in appended paper 1. First, the developed numerical procedure was used to conduct a parametric study on the average contact pressure by incorporating parameterized pressure–area curves into the numerical model. The effects of the average contact pressure on the ship motions, ice resistance, and ship performance were investigated. The numerical ship performance results were then compared with the full-scale performance data to determine values for the parameters of the *p*–*a* curve. The AHTS/IB Tor Viking II was used as the physical prototype with the ship and ice properties presented in Chapter 4.

5.1 Parametric study

As discussed in Section 3.4.3, the average contact pressure typically depends on the contact area through a *p*–*a* curve, as given in Eq. (3.25). However, the values for the parameters *k* and *n* in the literature exhibit a wide range of scatter, possibly because the dependences determined in various studies were derived under different conditions, i.e., the definitions of the contact area, test scales, and ice properties differed. The mechanism of this contact area dependence is not fully understood; therefore, this study was performed semi-empirically by carrying out a parametric study using the developed numerical procedure.

The parameterized *p*–*a* curve was defined as:

$$p_{\mathrm{av}} = p_0\left(\frac{A_{\mathrm{cr}}}{A_0}\right)^n = kA_{\mathrm{cr}}^n \tag{5.1}$$

The values of the parameter n were equally spaced between 0.0 and –0.4 (where $n = 0$ corresponds to a constant contact pressure, i.e., no *p*–*a* relation is used). A_0 and p_0 in Eq. (5.1) denote the reference area and pressure, respectively. Apart from simplifying the parametric study, the reference area and pressure values were introduced because a threshold value for the contact area below which the pressure was independent of the contact area needed to be fixed, implying that

there was a transition for the material property from being governed by fracture mechanics to being controlled by strength of material.

In this study, the values for A_0 and p_0 were determined empirically: in the Baltic Sea, the measured average pressure on a gauge with an area of 35×35 cm² has a mean value of 2.3 MPa (Kujala, 2007). These values served as reference values in the parametric study.

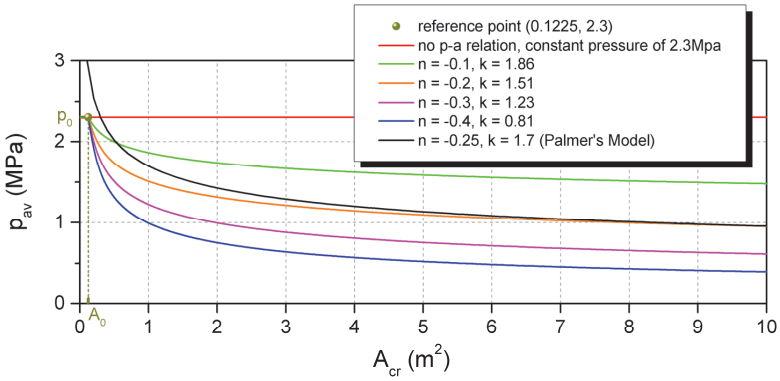

Fig. 5.1 Parameterized pressure–area curves

Fig. 5.2 and Fig. 5.3 present the mean values of the ship motions at full propulsion power, which were predicted using the selected *p*–*a* curves, versus the ice thickness. The mean values of motions are shown to generally increase as the *p*–*a* dependence becomes stronger (i.e., corresponding to smaller values of *n*).

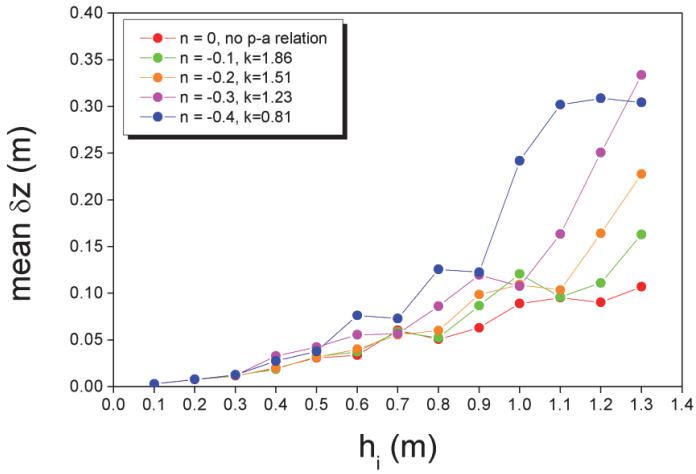

Fig. 5.2 Mean values of heave vs. ice thickness using p_{av} as a parameter

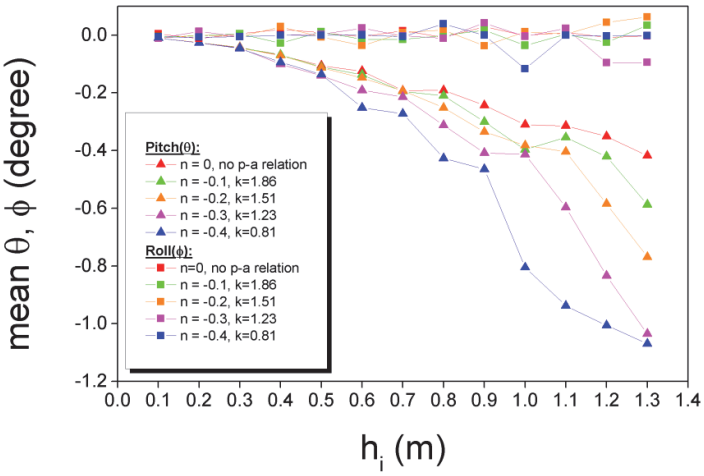

Fig. 5.3 Mean values of roll and pitch vs. ice thickness using p_{av} as a parameter

Fig. 5.4 is a plot of the predicted ice resistance at a speed of 5 m/s versus the ice thickness, illustrating that the ice resistance generally increased with the degree of dependence (i.e., decreasing values of n).

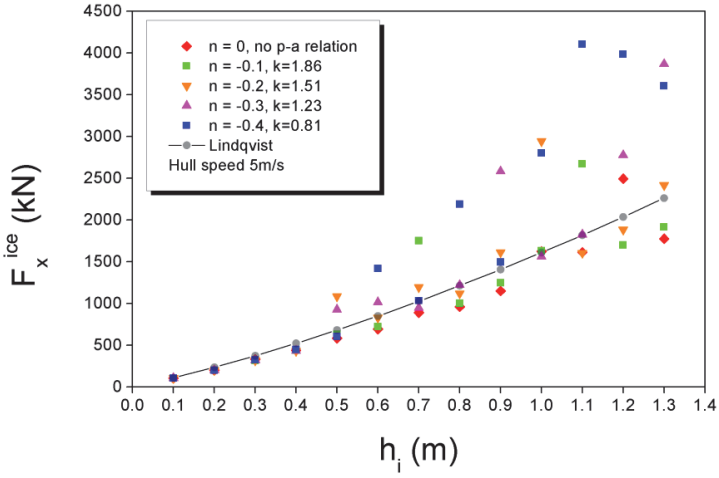

Fig. 5.4 Ice resistance vs. ice thickness using p_{av} as a parameter

Fig. 5.2 through Fig. 5.4 present the effects of the average contact pressure on the ship motions and the ice resistance, indicating that when the degree of dependence was stronger (i.e., the values of n were smaller), the ship tended to experience higher excitations from the ice that resulted in larger motions and higher resistance. This result can be attributed to the average contact pressure on a

certain contact area being lower when the dependence is stronger (i.e., the values of n are smaller); thus, a larger contact area must be attained to achieve the force needed to cause the ice to fail. Thus, the triangular force peaks for the icebreaking force have a larger area and thus larger energy consumption. The simulated motions and ice resistance for some ice thicknesses displayed some irregularities from the effects of the icebreaking pattern.

5.2 Evaluation of the *p*–*a* curve

The numerical predictions of the ship performance using the selected p–a curves are plotted in Fig. 5.5. There were smaller discrepancies between the results obtained for the p–a curve for n between –0.2 and –0.3 and the regression curve of the full-scale data than for the results obtained using other curves. The aforementioned n values agreed well with the values given by Palmer (1991).

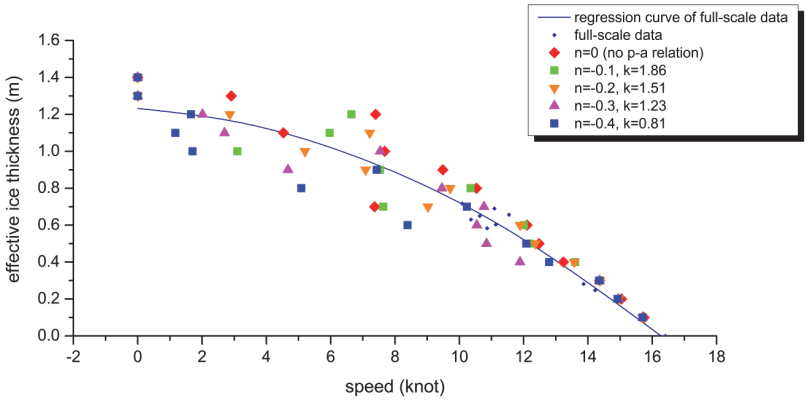

Fig. 5.5 h–v curve obtained using the p–a relation

6

Effect of the Ice Bending Failure Load

In this chapter, the effects of the ice bending failure criterion on the ship motions, ice resistance, and ship performance during continuous-mode icebreaking in level ice are considered. Appended paper 2 is associated with this problem. First, the bending failure criterion for sheet ice subjected to a dynamic load that was developed in Section 3.4.5 (Eq. (3.36)) was incorporated into the numerical procedure. Then, a series of case studies was carried out for the AHTS/IB Tor Viking II to calculate the ship motions, ice resistance, and ship performance, and the numerical results were validated using the full-scale data. Finally, the numerical results obtained using the static (Eq. (3.34)) and dynamic bending failure criteria were compared to each other, and the effects of the ice bending failure load and ship forward speed are discussed.

6.1 Validation of the ice dynamic bending failure criterion

Fig. 6.1 presents the *h*–*v* curves calculated using the dynamic and static bending failure criteria, respectively. The results obtained using the numerical procedure with the dynamic bending failure criterion correlated better with the full-scale regression curve.

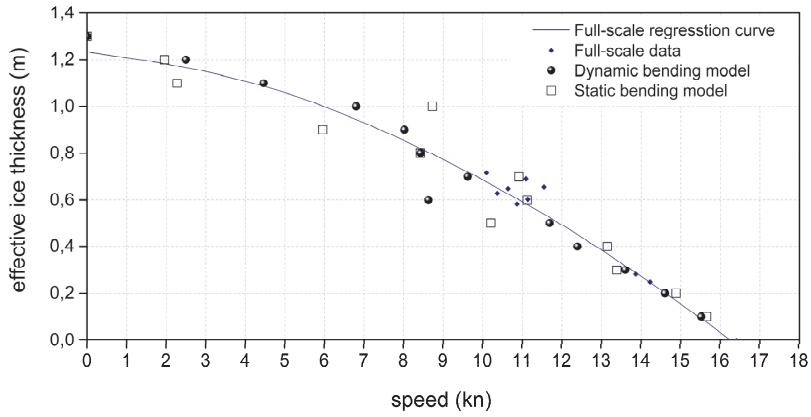

Fig. 6.1 *h*–*v* curve for different bending failure criteria

Fig. 6.2 presents the ice resistance at full propulsion power. The predicted ice resistance was in good agreement with the full-scale data.

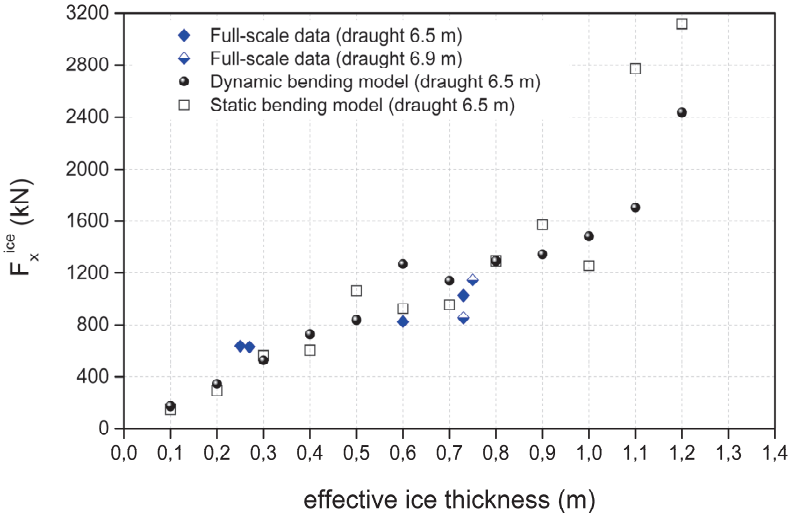

Fig. 6.2 Ice resistance at full propulsion power

6.2 Effect of dynamic bending on the ice resistance and ship motions

Fig. 6.3 presents the mean values of the simulated surge ice resistance and pitch moment.

The results obtained using the static bending failure criterion did not appear to be sensitive to the ship's forward speed in thick ice (e.g., for ice thicknesses of 0.7 and 1.1 m). However, in thin ice (e.g., for ice thicknesses of 0.1 and 0.3 m), the curves appeared to be moderately linear. This result can be attributed to the dominance of the broken ice resistance, R_{sbmg}, in thin ice. In the numerical model, this component was calculated using Lindqvist's (1989) resistance formulae, which accounts for the speed dependence. In thick ice, however, the icebreaking resistance component, R_{brk}, dominates, and the static bending failure model cannot capture the effect of the speed on the icebreaking forces.

The results obtained using the dynamic bending failure criterion varied linearly with the ship's forward speed, which is consistent with observations and data from previous studies (e.g., Voelker and Geisel, 1984; Riska et al., 1997).

Comparing the ice resistances that were calculated using these two ice bending criteria indicated that a higher ice resistance was obtained using the static bending criterion over a low speed range than that obtained using the dynamic bending criterion. However, contrasting results were obtained at high speeds. This result was obtained because, as shown in Fig. 3.9, the ice bending failure load for the dynamic bending criterion increased with the colliding speed that was associated with the ship's forward speed; for the static model, however, the ice bending failure load is independent of the ship speed. At low speeds, a higher ice bending failure load is obtained from the static bending criterion than that obtained from the dynamic bending criterion, which consequently resulted in a higher ice resistance.

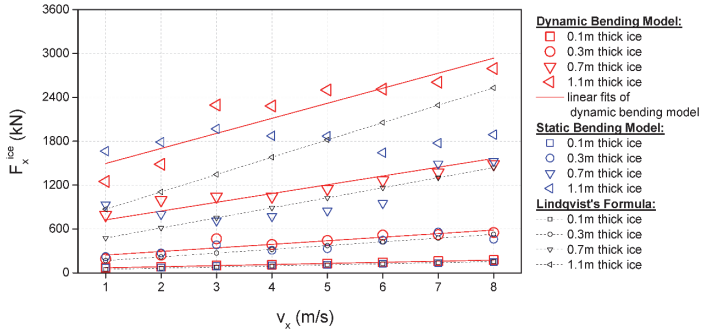

(a) Surge ice resistance

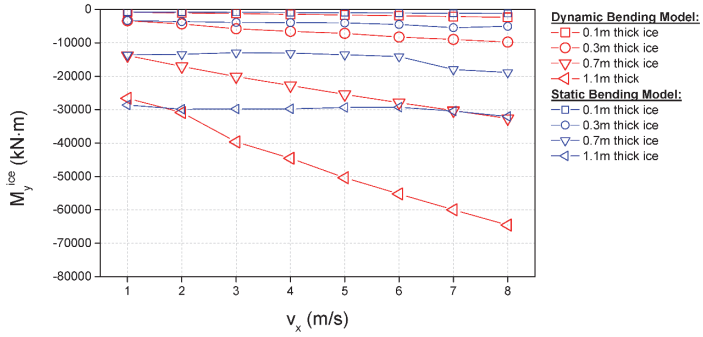

(b) Pitch moment

Fig. 6.3 Simulated mean values of ice resistance vs. ship forward speed for different ice thicknesses

The mean values of the simulated ship motions that were obtained using the static and dynamic bending failure criteria are plotted in Fig. 6.4: the heave that was calculated using the dynamic bending failure criterion varied linearly with the

ship's forward speed. Although the roll was not influenced by the ship speed, some major jumps for the roll angles were identified especially in thick ice. This observation was consistent with the phenomena reported by Ettema et al. (1987), as stated in Section 4.4.3.

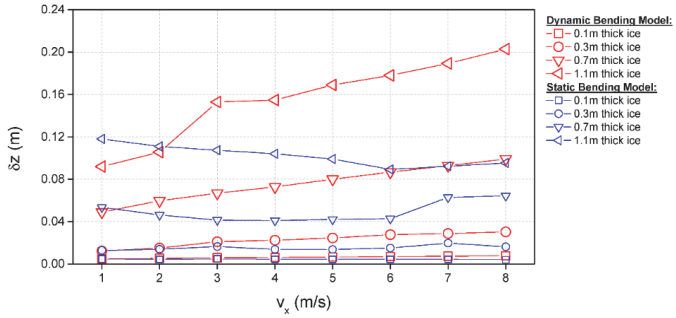

(a) Heave

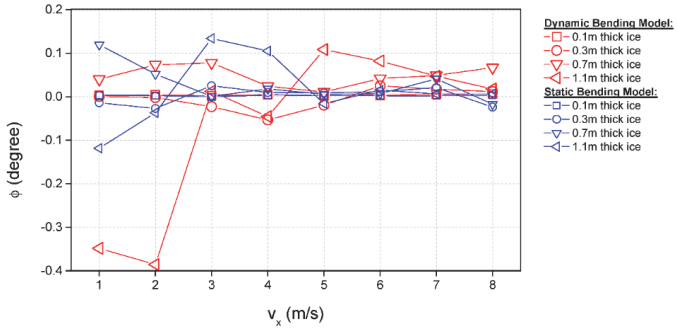

(b) Roll

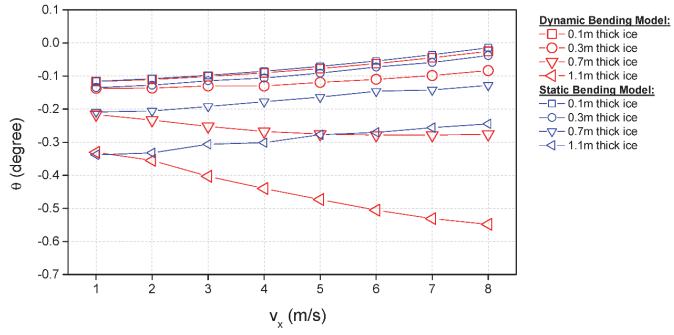

(c) Pitch

Fig. 6.4 Simulated mean values of the ship motions vs. the ship's forward speed for different ice thicknesses

The pitch angles calculated using the static bending model decreased linearly with the ship speed for all of the ice thicknesses considered. However, the pitch angles calculated using the dynamic bending model decreased with the ship speed for thin ice but increased with the ship speed for thick ice (Fig. 6.4 (c)). In medium-thick ice (i.e., ice thicknesses of 0.5 and 0.7 m), the pitch angles calculated using the dynamic bending criterion increased with the speed in the low speed range while decreased with the speed in the high speed range. The natural pitch frequency for the Tor Viking II is estimated to be 0.15 Hz. A spectral analysis on the time histories of the pitch moment at the lowest ship speed of 1.0 m/s yielded frequency values of 1.31 and 0.20 Hz for ice thicknesses of 0.1 and 1.1 m, respectively. As the ship speed increased, the frequency of pitch moment increased and thus moved farther away from the natural pitch frequency. This behavior resulted in a general decrease in the pitch, as was obtained using the static bending model. Using the dynamic bending model, however, the magnitude of the pitch moment in thick ice increased dramatically compared to that in thin ice, as well as to the results obtained using the static model. Therefore, the value of the pitch angle was affected by the magnitude of the pitch moment and its frequency. A similar trend in the variation in the mean values of pitch and heave with the ship speed has been reported for model tests by Ettema et al. (1987), as shown in Fig. 6.5.

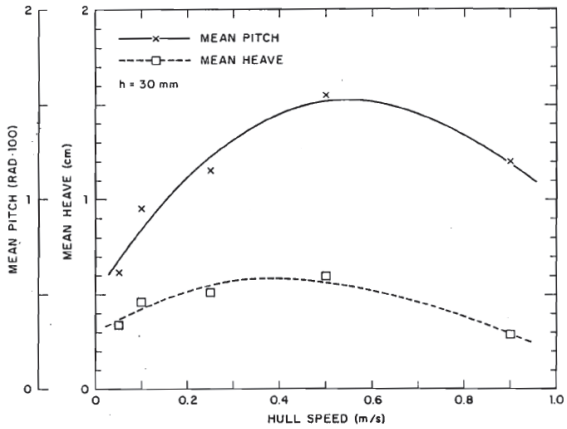

Fig. 6.5 Mean values of pitch and heave vs. hull speed from a model test with an USCGC Polar-Class Icebreaker (Ettema et al., 1987)

7

Performance of a Dual-Direction Ship in Level Ice

A study on the performance of the dual-directional icebreaking tanker M/T Uikku is discussed in this chapter: appended paper 3 is the corresponding paper. The study was carried out at model scale. The effect of the propeller–ice–hull interaction for running astern (propeller first) was considered in the numerical procedure by calibrating the broken ice resistance component, R_{sbmg}, using the model test data. The numerical model was in turn used to study the thrust deduction in ice.

7.1 Introduction to thrust deduction

7.1.1 Thrust deduction in open water

Open water tests have shown that the thrust force of a ship at the self-propulsion point, i.e., free running at the maximum speed that can be attained without an external towing force, exceeds the towing force that is measured when the ship is towed at the same speed. Thus, the propeller alters the hull resistance by an amount, for which the force equilibrium equation can be expressed as:

$$T_{\mathrm{T}} = R_{\mathrm{ow}}^{[\mathrm{h}]} + \Delta R_{\mathrm{ow}} \qquad (7.1),$$

where T_{T} denotes the total thrust, i.e., the thrust measured on the propeller shaft; $R_{\mathrm{ow}}^{[\mathrm{h}]}$ is the open water resistance, where the superscript [h] denotes the resistance under the towed condition (the bare hull resistance); and ΔR_{ow} is the hull resistance augmentation (the added resistance) that is caused by the interaction between the ship hull and propeller flow.

The physical origin of ΔR_{ow} is that the propeller accelerates flow in front and behind of it resulting in an increased rate of shear in the boundary layer (i.e., an increased frictional resistance on the propeller blades) and a reduced (ahead mode) or increased (astern mode) pressure over the rear of the hull (i.e., an increased pressure resistance on the hull).

In practice, this increase in the resistance is viewed as a thrust deduction:

$$T_{\mathrm{T}} \cdot (1 - t_{\mathrm{ow}}) = R_{\mathrm{ow}}^{[\mathrm{h}]} \tag{7.2}$$

where ΔR_{ow} is expressed as a fraction of the total thrust by a thrust deduction factor that is defined as:

$$t_{\mathrm{ow}} = \frac{\Delta R_{\mathrm{ow}}}{T_{\mathrm{T}}} \tag{7.3}$$

7.1.2 Thrust deduction in ice

In ice-covered waters, the force equilibrium equation for a ship breaking ice at self-propulsion can be expressed as:

$$T_{\mathrm{T}} = \underbrace{R_{\mathrm{I}}^{[\mathrm{h}]} + R_{\mathrm{ow}}^{[\mathrm{h}]}}_{R_{\mathrm{T}}^{[\mathrm{h}]}} + \Delta R_{\mathrm{T}} \tag{7.4}$$

where $R_{\mathrm{I}}^{[\mathrm{h}]}$ is the bare hull ice resistance; $R_{\mathrm{T}}^{[\mathrm{h}]}$ is the total bare hull resistance; and ΔR_{T} is the hull resistance augmentation caused by the interaction among the ship hull, propeller flow and ice.

Unlike the added resistance in open water, ΔR_{T} is often observed to be negative when the ship is running propeller first. In fact, when the ship is running propeller first in ice-covered waters, the propeller causes an increase in the hull resistance (a positive ΔR_{ow}) because of the interaction between the stern and propeller flow, as explained in Section 7.1.1, whereas the broken ice floes attached to the bottom of the hull are flushed backwards (towards the bow) by the flow generated by the propeller which causes a decrease (denoted by ΔR_{I}) in the hull resistance component R_{sbmg}. The experiences with icebreaking for a ship that was running astern suggest that the overall effect of the propeller is often to reduce the total hull resistance even if the open water thrust deduction is higher than when the ship was running ahead, implying that the effect of ΔR_{I} overrides that of ΔR_{ow}.

The added resistances, ΔR_{ow} and ΔR_{I}, originate from different regions of the hull and arise from different physical mechanisms; thus, ΔR_{T} was assumed to be a superposition of ΔR_{ow} and ΔR_{I}:

$$\Delta R_{\mathrm{T}} = \Delta R_{\mathrm{I}} + \Delta R_{\mathrm{ow}} \tag{7.5}$$

Thus, Eq. (7.4) becomes:

$$T_{\mathrm{T}} = R_{\mathrm{I}}^{[\mathrm{h}]} + \Delta R_{\mathrm{I}} + R_{\mathrm{ow}}^{[\mathrm{h}]} + \Delta R_{\mathrm{ow}} \tag{7.6}$$

By introducing the concept of the net thrust in ice, which is defined by Eq. (3.40), Eq. (7.6) can be alternatively expressed as:

$$T_{\text{net}} = R_{\text{I}}^{[\text{h}]} + \Delta R_{\text{I}} \tag{7.7}$$

The thrust deduction factor in ice is defined in this thesis as:

$$t_{\text{I}} = \frac{\Delta R_{\text{I}}}{T_{\text{T}}} \tag{7.8}$$

Thus,

$$T_{\text{T}} \cdot (1 - t_{\text{ow}} - t_{\text{I}}) = R_{\text{ow}}^{[\text{h}]} + R_{\text{I}}^{[\text{h}]} \tag{7.9}$$

In addition, an overall thrust deduction factor can be defined as:

$$t_{\text{TOT}} = \frac{\Delta R_{\text{T}}}{T_{\text{T}}} \tag{7.10}$$

Thus,

$$T_{\text{T}} \cdot (1 - t_{\text{TOT}}) = R_{\text{ow}}^{[\text{h}]} + R_{\text{I}}^{[\text{h}]} \tag{7.11}$$

7.2 M/T Uikku

M/T Uikku was the first western oil tanker to navigate the entire Northern Sea Route. The product tanker was built in 1977 and was originally installed with a conventional propeller–rudder propulsion system. In 1993, the propeller–rudder configuration was replaced with an 11.4 MW Azipod unit with a “pushing” type azimuth propeller, and the ship’s ice strengthening was also increased.

The stern design does not allow the propeller to azimuth fully in 360°. Thus, the efficiency in astern mode is lower than that in ahead mode because of the inversely rotating propeller, as illustrated by the K_{T}, K_{Q} and η_0 curves derived from the propeller open water model tests (Fig. 7.1).

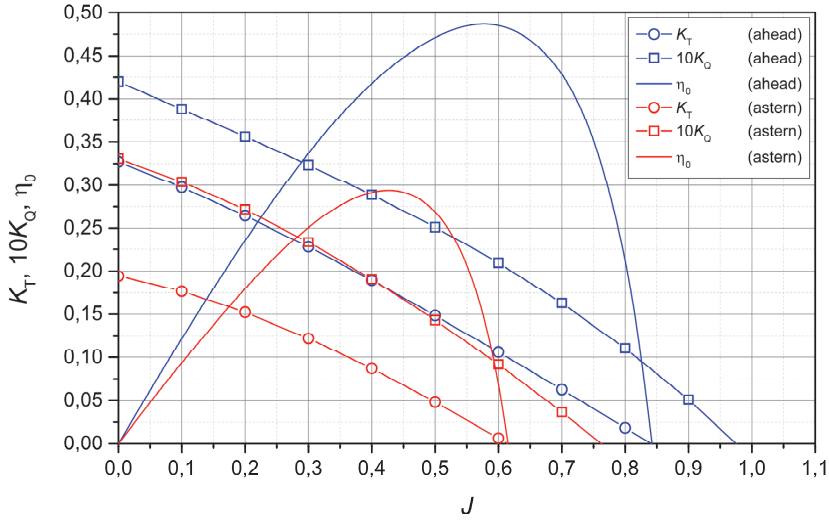

Fig. 7.1 K_T, K_Q and η_0 curves (n = 15 s^{-1})

The main particulars of the ship are listed in Table 7.1.

Table 7.1 Ship parameters*

Parameter	Notation	Dimension	F.S Value	M.S Value
Length over all	LOA	m	164.4	5.21
Length between perpendiculars	L_{pp}	m	150.0	4.75
Breath, moulded	B	m	22.2	0.70
Draught, icebreaking	D	m	9.5	0.30
Propulsion power	P_D	W	11.4×10^6	64.55
Propeller diameter	D_P	m	5.6	0.179

* M.S. denotes model scale, F.S. denotes full scale; the scale factor is 31.56.

7.3 Information from the model tests

A series of model tests was conducted by Leiviskä (2004) to investigate the propeller–hull–ice interaction using a model of the M/T Uikku. The tests were conducted under towed as well as self-propulsion conditions in astern mode to investigate the effect of the bow propellers on the ice floe turning and submerging resistance component, R_{sbmg}. In the towed tests, the bare hull resistance, $R_T^{[h]}$, was measured at the same speeds as in the self-propulsion condition.

The level ice model tests were conducted for two ice thicknesses, 18 and 29 mm. For each of the ice thicknesses, four tests were carried out with different power

outputs that bounded the installed propulsion power of the ship. The test results provided by Leiviskä (2004) were somewhat raw; thus, the author of this thesis extended the results for use in this study. The maximum ship speeds at the full installed propulsion power at each of the ice thicknesses were calculated and are listed in Table 7.2.

Table 7.2 Maximum ship speed attainable at full power in astern mode*

Ice thickness	mm	0	18	29
Ship speed	m/s	0.97	0.59	0.33

* The ship speed values listed in Table 7.2 were calculated by the author of this thesis based on the test results reported by Leiviskä (2004).

The added resistances caused by the flushing effect of the propeller flow in astern mode were calculated and are listed in Table 7.3 and Table 7.4 based on the measured quantities.

Table 7.3 Hull resistance augmentation in 18mm level ice in astern mode*

v [m/s]	n [1/s]	Q [Nm]	P_D [W]	T_T [N]	$R_T^{[h]}$ [N]	$R_{ow}^{[h]}$ [N]	$R_I^{[h]}$ [N]	t_{ow}	ΔR_{ow} [N]	ΔR_T [N]	ΔR_I [N]
0.36	10.0	0.440	27.6	12.6	18.2	2.0	16.2	0.219	2.8	-5.6	-8.4
0.55	12.5	0.772	60.6	19.9	25.8	4.4	21.4	0.241	4.8	-5.9	-10.7
0.74	15.0	1.009	95.1	29.9	35.7	8.0	27.7	0.257	7.7	-5.8	-13.5
0.91	17.5	1.334	146.7	41.0	45.2	11.6	33.6	0.264	10.8	-4.2	-15.0

Table 7.4 Hull resistance augmentation in 29mm level ice in astern mode*

v [m/s]	n [1/s]	Q [Nm]	P_D [W]	T_T [N]	$R_T^{[h]}$ [N]	$R_{ow}^{[h]}$ [N]	$R_I^{[h]}$ [N]	t_{ow}	ΔR_{ow} [N]	ΔR_T [N]	ΔR_I [N]
0.26	11.7	0.789	57.9	19.6	23.0	1.1	21.9	0.179	3.5	-3.4	-6.9
0.38	12.5	0.851	66.8	22.6	29.2	2.2	27.0	0.203	4.6	-6.6	-11.2
0.53	15.0	1.267	119.4	32.0	37.5	4.1	33.4	0.217	6.9	-5.5	-12.4
0.73	17.5	1.650	181.4	42.3	49.6	7.6	42.0	0.235	9.9	-7.3	-17.2

* The following quantities were originally recorded in the level ice model tests conducted by Leiviskä (2004): v, n, Q, T_T, and $R_T^{[h]}$ (highlighted in yellow). The values presented for $R_{ow}^{[h]}$ and t_{ow} (highlighted in green) were interpolated by the author of this study from the open water tests conducted by Leiviskä (2004). The remianing quanties were calculated by the author of this study using the measurements and equations presented in Section 7.1

The negative values for ΔR_T and ΔR_I that are shown in Table 7.3 and Table 7.4 illustrate that when the ship was running astern in level ice, the propeller had the effect of lowering the total hull resistance. This is because the propeller flow flushed away some of the broken ice floes that would have otherwise been

attached to, or slid along the hull, thereby decreasing the area of the hull that was covered by the broken ice pieces. Consequently, the resistance component, R_{sbmg}, was lowered.

7.4 Calibration of the numerical model

In the numerical model, R_{sbmg} was calculated using an empirical formula developed by Lindqvist (1989), where 70% of the underwater part of the hull is assumed to be covered by broken ice floes during icebreaking. Lindqvist's (1989) resistance formula was originally developed for ships moving ahead; thus, this coverage coefficient was modified in this study to account for the flushing effect of the propeller flow on the broken ice floes when the ship was moving astern.

This coefficient was modified by fitting the numerical calculations to the model test results presented in Table 7.2. That is, for each of the ice thicknesses listed in Table 7.2, the ship speed at the full installed propulsion power was calculated using the numerical procedure. Adjusting Lindqvist's (1989) coverage coefficient in the numerical model yielded a value of 0.32 for the best fit to the model test results. This value was used in the numerical procedure to predict the ship performance in astern mode. For ahead mode, the original value of 0.7 for the coverage coefficient proposed by Lindqvist (1989) was used.

With the modified broken ice resistance component, the numerical procedure was used to predict the ship performance for a range of ice thicknesses, as shown in Fig. 7.2. This figure presents the calculated ship performance, which was obtained using the average values of the material properties of ice measured in the model tests, as listed in Table 7.5.

Table 7.5 Average values of the model ice properties

Parameter	Notation	Dimension	Value
Density	ρ_i	kg/m^3	880
Young's modulus	E	MPa	34.7
Poisson ratio	ν		0.33
Crushing strength	σ_{cr}	kPa	76.7
Bending strength	σ_f	kPa	24.3
Coefficient of friction	μ		0.05

Fig. 7.2 clearly illustrates that the ship performance in thick ice in astern mode was better than that in ahead mode, even for a lower total thrust.

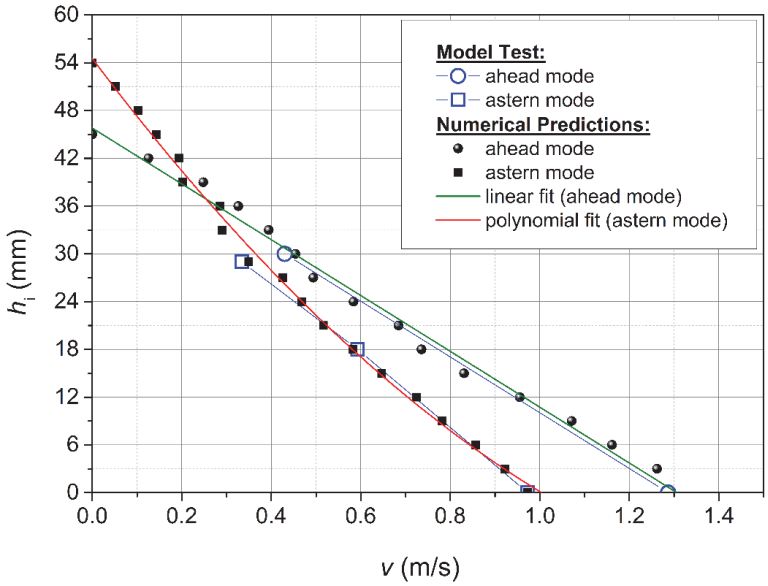

Fig. 7.2 h–v curve

Fig. 7.3 presents a plot of the predicted bare hull ice resistance versus the ship speed against the model test results. The predicted and measured values were in good agreement with each other. The numerical predictions were verified using the model test results by performing the calculations shown in Fig. 7.3 using the actual values of the ice material properties measured in each test, as listed in Table 7.6.

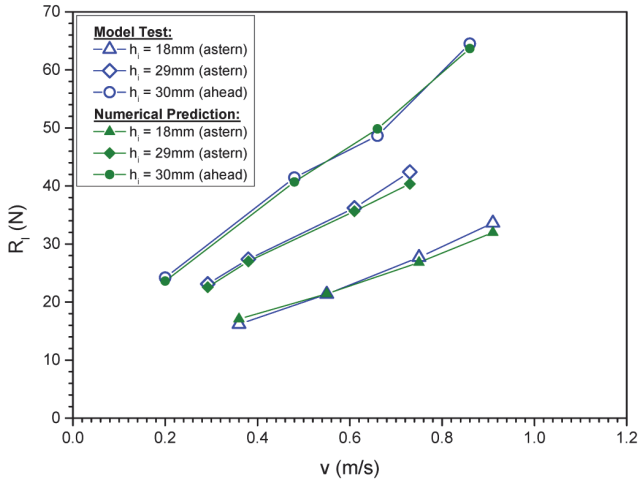

Fig. 7.3 Bare hull ice resistance

Table 7.6 Model ice properties for the resistance tests

Direction	h_i (mm)	σ_f (kPa)	σ_{cr} (kPa)	E (MPa)
Astern	18	21.6	100.2	73.0
Astern	29	26.9	69.4	24.2
Ahead	30	28.1	69.3	23.8

7.5 Thrust deduction in ice

Eq. (7.7) illustrates that the added resistance from the propeller–ice interaction, ΔR_I, i.e., the thrust deduction in ice, is equal to the difference between the net thrust, T_{net}, and the bare hull ice resistance, $R_I^{[h]}$.

Fig. 7.4 presents the predicted bare hull ice resistance versus the ship speed for a series of ice thicknesses. For these calculations, the average values of the material properties of ice listed in Table 7.5 were used so that the results were comparable to each other.

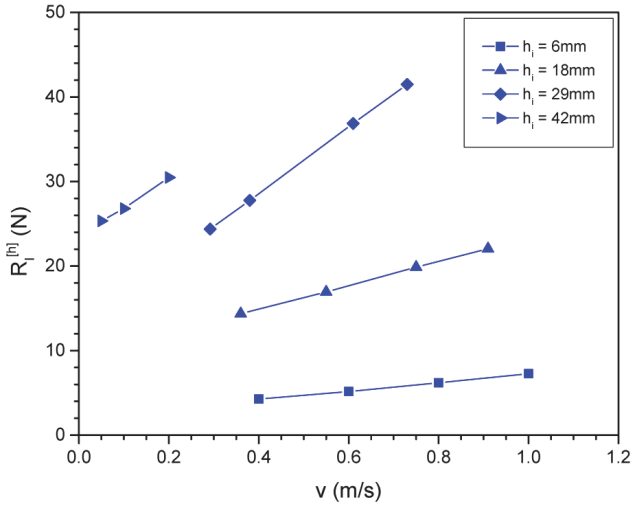

Fig. 7.4 Predicted bare hull ice resistance vs. ship speed

Fig. 7.5 provides an example of the procedure for deriving the thrust deduction in ice. For each ice thickness, the ship speed at the full installed propulsion power was determined using the h–v curve shown in Fig. 7.2. Then, the net thrust and bare hull ice resistance at the same speed were obtained from the T_{net} and bare hull ice resistance curves.

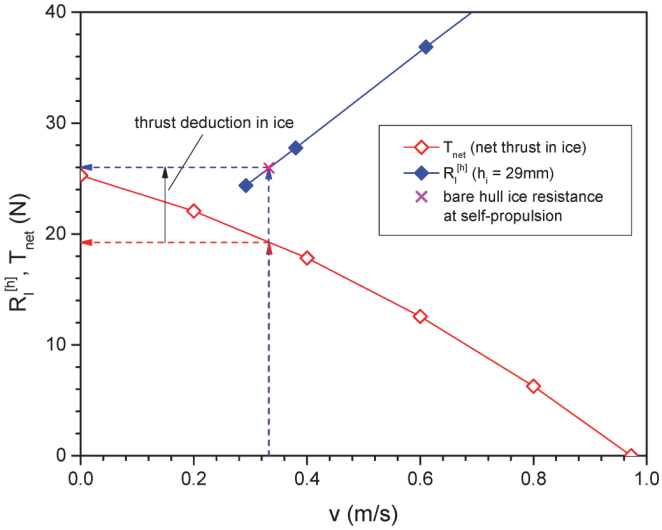

Fig. 7.5 Example of deriving the added resistance from the propeller–ice interaction

The thrust deduction in ice for a series of ice thicknesses at the full installed propulsion power is plotted in Fig. 7.6.

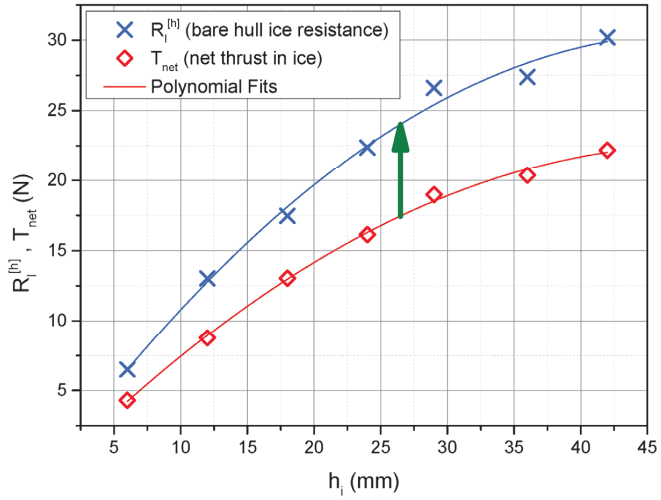

Fig. 7.6 Thrust deduction at full propulsion power in astern mode

Fig. 7.7 presents the thrust deduction factor in ice, t_{I}, and the overall thrust deduction factor, t_{TOT}, versus the ship speed.

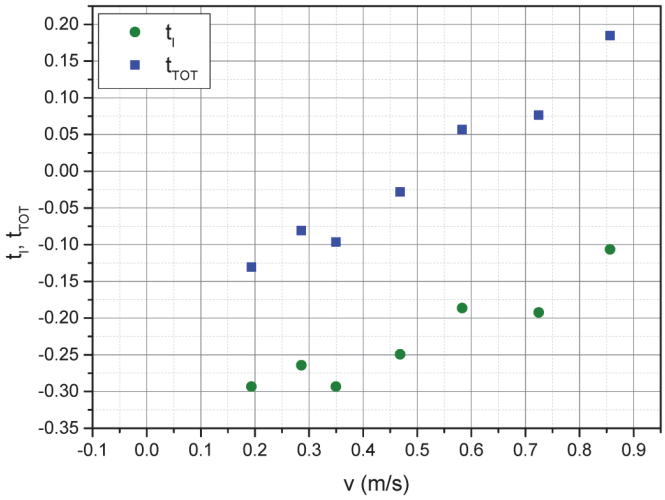

Fig. 7.7 Thrust deduction factors during icebreaking

8

Summary

A numerical procedure was developed to simulate the icebreaking process in level ice in detail. The procedure was then used to investigate various factors by comparisons and calibrations with full- and model-scale measurements. The studies were conducted using a series of case studies on two icebreaking ships, the AHTS/IB Tor Viking II and the M/T Uikku, at full and model scales, respectively. Several issues that have not been previously considered are explored in this thesis.

8.1 Primary conclusions

The primary conclusions from this thesis are summarized below.

Ship motions, icebreaking pattern, and ice resistance are three key characteristics that interact in the continuous-mode icebreaking process:

i. Ship motions in pitch and heave are generally beneficial for icebreaking, especially in thick ice.

ii. Transverse motions, i.e., sway, yaw, and roll, may result in an added resistance because of an enlarged forward project area and more frequent side hull crushing by ice.

iii. Non-uniform loading conditions around the ship hull resulting from an asymmetric icebreaking pattern may excite ship motions in both the horizontal and vertical planes.

iv. The icebreaking pattern simultaneously affects and is affected by ship motions in both the horizontal and vertical planes.

v. Under certain conditions, the ice resistance can be determined by the icebreaking pattern, e.g., when shoulder crushing occurs, the ship experiences a higher ice resistance, even in relative thin ice, than in the absence of shoulder crushing.

The mean values of the ship motions and ice resistance increase with the degree of dependence of the pressure–area relation (i.e., the *n* value decreases). This result can be attributed to the decrease in the average contact

pressure on a certain contact area for a stronger p–a dependence (i.e., smaller values of n); thus, a larger contact area must be attained to achieve the force needed to cause the ice to fail. Thus, the triangular force peaks for the icebreaking force have a larger area and thus a larger energy consumption. Calibrating the numerical procedure using the full-scale data yielded an n value between –0.3 and –0.2. Moreover, the average contact pressure may affect the ship motions and ice resistance indirectly by altering the icebreaking pattern.

A dynamic bending failure criterion for ice was incorporated into the numerical procedure to clearly reveal the effect of the ship's forward speed on the ship motions and the ice resistance compared to the previously used static bending failure criterion. The ice resistance and pitch moment calculated using the dynamic bending failure criterion generally increased linearly with the ship's forward speed. The heave that was calculated using the dynamic bending failure criterion varied linearly with the ship's forward speed; roll was not affected by the ship speed, but some major jumps for roll angles were identified especially in thick ice. The pitch that was calculated using the dynamic bending failure criterion decreased with the ship speed for thin ice but increased with the ship speed for thick ice. This behavior resulted from the effect of both the magnitude and frequency of the pitch moment.

The effect of propeller flow on the hull resistance in astern mode was considered by calibrating the numerical model with model test data. The value of the coverage coefficient in Lindqvist's (1989) resistance formula for the M/T Uikku when going astern at the installed propulsion power was 0.32. For the installed propulsion power, the thrust deduction in thick ice was higher than that in thin ice, and the absolute value of the thrust deduction factor in pure ice generally decreased with the ship speed. For different values of the propulsion power, the absolute value of the added resistance from the propeller–ice interaction increased with the ship speed (which was associated with different values of the propulsion power) for a certain ice thickness.

8.2 Contributions

The primary contributions of the studies included in this thesis are given below.

A numerical procedure was developed to accomplish the following objectives:

i. solve the interaction between the ship hull and the ice edge based on realistic contact conditions;
ii. reproduce the icebreaking pattern from repeated icebreaking events

iii. include ship motions in 6 DOFs;
iv. allow for various motion configurations; and
v. simulate both captured and free-running conditions.

The developed numerical procedure was used to clarify the following issues that are related to the continuous-mode icebreaking process of ships in level ice:

i. the interactions among the ship motions, icebreaking pattern and ice resistance;
ii. the effect of the average contact pressure;
iii. the bending failure criterion of an ice sheet subjected to a dynamic load;
iv. the speed dependence of the icebreaking resistance and ship motions;
v. the performance of a dual-direction ship; and
vi. the thrust deduction in ice.

8.3 Recommendations for future work

In practice, the icebreaking process in level ice involves a breaking pattern of ice which seems quite chaotic. Further studies should be carried out to investigate the features of this chaotic system instead of following the evolution of individual breaking events. Whereas the icebreaking process does evolve a pattern that is followed and repeated over the entire process, the patterns that evolve over a long time can be highly unpredictable. Interestingly, the numerical results for the icebreaking pattern are similar in character: the simulated results indicate that the evolution of the icebreaking pattern is highly unpredictable even if the ice was bent in a deterministic manner and all of the elements in the model were deterministic, i.e., no randomness was introduced into the model; the icebreaking pattern was also sensitive to the initial conditions, e.g., changing the ice thickness occasionally resulted in severe shoulder crushing.

A follow-up study should be conducted on the correlation between the mathematical model of the icebreaking pattern and the channel width and ship motions. The occurrence of shoulder crushing was determined by the icebreaking pattern, which was obtained using the numerical model by assuming that ice bent in a predefined manner. The icebreaking patterns are inherently based on the major assumptions made in the analytical treatment of the problem.

The speed dependence of the ice wedge failure load obtained in this study was based on limited information and idealized conditions. The adequacy of the dynamic bending failure criterion for describing the icebreaking

processes for other ice thicknesses and flexural strengths should be verified in future studies. For example, the speed-dependent coefficient function, λ_t, was derived for a certain ice thickness (0.35 m) and ice flexural failure strength (1.2 MPa), assuming that the failure load was proportional to the ice thickness squared and the ice flexural strength. The effect of the geometry of the ice wedge should also be investigated. For this purpose, more extensive studies, both theoretical and physical, are required to solve the problem of the ice–water–ship interaction.

In practice, the propeller flow may also affect the breaking of level ice by lowering the water pressure below the intact ice. Future studies are needed to describe this effect quantitatively.

References

Aksnes, V., 2010. A simplified interaction model for moored ships in level ice. Cold Regions Science and Technology, Vol. 63, pp. 29–39.

Aksnes, V., 2011a. A panel method for modeling level ice actions on moored ships. Part 1: Local ice force formulation. Cold Regions Science and Technology, Vol. 65, pp. 128–136.

Aksnes, V., 2011b. A panel method for modeling level ice actions on moored ships. Part 2: Simulations. Cold Regions Science and Technology, Vol. 65, pp. 137–144.

Daley, C., 1991. Ice edge contact – A brittle failure process model. Ph.D. Thesis, Laboratory of Naval Architecture and Marine Engineering, Helsinki University of Technology, Espoo, Finland.

Dempsey, J.P. and Zhao, Z., 1993. Elastohydrodynamic response of an ice sheet to forced sub-surface uplift. Journal of the Mechanics and Physics of Solids, Vol. 41, pp. 487–506.

Edwards, R.Y., Major, R.A., Kim, J.K., German, J.G., Lewis, J.W., and Miller, D.R., 1976. Influence of major characteristics of icebreaker hulls on their powering requirements and maneuverability in ice. Transactions of Society of Naval Architects and Marine Engineers (SNAME), Vol. 84.

Enkvist, E., 1972. On the ice resistance encountered by ships operating in the continuous mode of icebreaking. Report No. 24, The Swedish Academy of Engineering Science in Finland, Helsinki, Finland.

Ettema, R., Stern, F., and Lazaro, J., 1987. Dynamics of continuous-mode icebreaking by a Polar-class icebreaker hull. Report No. 314, Iowa Institute of Hydraulic Research.

Ettema, R., Sharifi, M.B., Georgakakos, K.P., and Stern, F., 1991. Chaos in continuous-mode icebreaking. Cold Regions Science and Technology, Vol. 19, pp. 131–144.

Faltinsen, O.M., 1990. Sea loads on ships and offshore structures. Cambridge University Press, Cambridge, UK.

Farin, G.E., 1997. Curves and surfaces for computer-aided geometric design – a practical guide. Academic Press, New York.

Fossen, T.I., 2011. Handbook of marine craft hydrodynamics and motion control, John Wiley & Sons, Ltd, Chichester, UK.

Fox, C., 1993. The response of a floating ice-sheet to rapid edge loading. Ice Mechanics, ASME AMD, Vol. 163, pp. 145–150.

Frederking, R. and Barker, A., 2002. Friction of sea ice on steel for condition of varying speeds. Proceedings of 12th International Offshore and Polar Engineering Conference (ISOPE), Kitakyushu, Japan, May 26–31, pp. 766–771.

Hopkins, M.A., 2004. A discrete element Lagrangian sea ice model. Engineering Computations, Vol. 21, No. 2/3/4, pp. 409–421.

ISO, 2010. Petroleum and Natural Gas Industries – Arctic Offshore Structures. International Organization for Standardization, ISO 19906, Geneva, Switzerland.

Izumiyama, K., Kitagawa, H., Koyama, K., and Uto, S., 1991. On the interaction between a conical structure and ice sheet, Proceedings of 11th International Conference on Port and Ocean Engineering under Arctic Conditions (POAC), St. John's, Canada, pp. 155–166.

Jansson, J.E., 1956(a). Ice-breakers and their design, Part I. European Shipbuilding, No. 5, pp. 112–128.

Jansson, J.E., 1956(b). Ice-breakers and their design, Part II. European Shipbuilding, No. 6, pp. 143–151.

Jardaan, I.J., Maes, M.A., Brown, P.W., and Hermans, I.P., 1993. Probabilistic analysis of local ice pressures. Journal of Offshore Mechanics and Arctic Engineering, Vol. 115, pp. 83–89.

Joensuu, A. and Riska, K., 1988. Contact between ice and structure (in Finnish) Helsinki University of Technology, Laboratory of Naval Architecture and Marine Engineering, Report M-88, Otaniemi, 1988.

Jones, S.J., 2004. Ships in ice – a review. 25th Symposium on Naval Hydrodynamics, St. John's, Newfoundland and Labrador, Canada, August 2004.

Juurmaa, K. and Segercrantz, H., 1981. On propulsion and its efficiency in ice. Proceedings of 6th STAR Symposium, Ottawa, 17–19 June, 1981. SNAME, New York, pp. 229–237.

Juurmaa, K., Wilkman, G., and Bäckström, M., 1995. New ice breaking tanker concept for the Arctic (DAT). Proceedings of the 13th International Conference on

Port and Ocean Engineering under Arctic Conditions (POAC), August 15–18, Murmansk, Russia.

Juurmaa, K., Mattsson, T., and Wilkman, G., 2001. The development of the new double acting ships for ice operation. Proceedings of 16th International Conference on Port and Ocean Engineering under Arctic Conditions (POAC), Ottawa, Canada, Vol. 2, pp. 719–726.

Juva, M. and Riska, K., 2002. On the power requirement in the Finish-Swedish ice class rules. Research Report No. 53, Helsinki University of Technology, Ship Laboratory, Espoo, Finland.

Kashteljan, V.I., Poznjak, I.I., and Ryvlin, A.J., 1968. Ice resistance to motion of a ship. Sudostroyeniye, Leningrad, Russia.

Keinonen, A., Browne, R.P., Revill, C.R., and Bayly, I.M., 1991. Icebreaker performance prediction. Transactions of Society of Naval Architects and Marine Engineers (SNAME), Vol. 99, pp. 221–248.

Kerr, A. D., 1975. The bearing capacity of floating ice plates subjected to static or quasi-static loads – a critical survey. Corps of Engineers, U.S. Army, Cold Regions Research and Engineering Laboratory.

Kitagawa, H. et al., 1986. A study of ship performance in ice-covered waters – effect of parallel mid-body. NRC, Institute for Marine Dynamics, Report No. LM-AVR-14.

Kurdyumov, V.A. and Kheisin, D.E., 1976. Hydrodynamic model of the impact of a solid on ice. International Applied Mechanics, Vol. 12(10), pp. 1063–1068.

Kotras, T.V., Baird, A.V., and Naegle, J.W., 1983. Predicting ship performance in level ice. Transactions of Society of Naval Architects and Marine Engineers (SNAME), Vol. 91, pp. 329–349.

Kujala, P., Suominen, M., and Jalonen, R., 2007. Increasing the safety of icebound shipping. Final Scientific Report: Volume 1, Ship Laboratory, Helsinki University of Technology. Espoo, Finland.

Langen, I. and Sigbjornsson, R., 1977. Dynamic analysis of structures, Tapir, Trondheim, Norway, 505 pp.

Leiviskä, T., 2004. The propulsion coefficients of ships in ice and in open water (in Finish). Helsinki University of Technology, Ship Laboratory, Report M-287, Espoo, Finland.

Lewis, J.W. and Edwards R.Y., 1970. Methods for predicting icebreaking and ice resistance characteristics of icebreakers. Transactions of Society of Naval Architects and Marine Engineers (SNAME), Vol. 78, pp. 213-249.

Lewis, J.W., Bulat V., Glen I.F., and Kotras T., 1983. A semi-empirical ice resistance model. Vol. 1, main report, ARCTEC Canada Ltd., Kanata (Ontario), Canada.

Lindqvist, G., 1989. A straightforward method for calculation of ice resistance of ships. Proceedings of 10th International Conference Port and Ocean Engineering under Arctic Conditions (POAC), Luleå, Sweden, pp. 722–735.

Liu, J., 2009. Mathematical modeling ice – hull interaction for real time simulations of ship manoeuvring in level ice. Ph.D. Thesis, Faculty of Engineering and Applied Science, Memorial University of Newfoundland, St. John's, Newfoundland, Canada.

Liu, Z., 2011. Analytical and numerical analysis of iceberg collisions with ship structures. Ph.D. Thesis, Department of Marine Technology, Norwegian University of Science and Technology, Trondheim, Norway.

Lu, W., Løset, S. and Lubbad, R., 2012. Simulating ice–sloping structure interactions with the cohesive element method. Proceedings of the 31st International Conference on Ocean, Offshore and Arctic Engineering (OMAE), July 1–6, Rio de Janerio, Brazil, Vol. 6, pp. 519–528.

Lubbad, R. and Løset, S., 2011. A numerical model for real-time simulation of ship–ice interaction. Cold Regions Science and Technology, Vol. 65, pp. 117–127.

Løset, S., 1994. Discrete element modelling of a broken ice field – Part I: model development. Cold Regions Science and Technology, Vol. 22 (4), pp. 339–347.

Martio, J., 2007. Numerical simulation of vessel's manoeuvring performance in uniform ice. Report No. M-301, Ship Laboratory, Helsinki University of Technology, Espoo, Finland.

Masterson, D. M. and Frederking, R., 1993. Local contact pressures in ship–ice and structure–ice interactions. Cold Regions Science and Technology, Vol. 21, pp. 169–185.

Masterson, D.M., Frederking, R.M.W., Wright, B., Kärnä, T., and Maddock,W.P., 2007. A revised ice pressure–area curve. Proceedings 19th International Conference on Port and Ocean Engineering under Arctic Conditions (POAC), Dalian University of Technology, Dalian, China, Vol. 1, pp. 305–314.

Matlock, H., Dawkins, P., and Panak, J., 1971. Analytical model for ice–structure interaction. Journal of the Engineering Mechanics Division, Vol. 97, No. 4, pp. 1083–1092.

Milano, V., 1973. Ship resistance to continuous motion in ice. Transactions of Society of Naval Architects and Marine Engineers (SNAME), No. 9.

Mäkinen, E., Lahti, A., and Rimppi, M., 1975. Influence of friction on ice resistance; search for low friction surfaces. Paper G, Society of Naval Architects and Marine Engineers (SNAME), IceTech 75, 9-11 April, 1975, Montreal, Canada.

Naegle, J.N., 1980. Ice resistance prediction and motion simulation for ships operating in the continuous mode of icebreaking. Ph.D. Thesis, University of Michigan, Michigan, USA.

Nguyen, D. T., Sørbø, A. H., and Sørensen, A. J., 2009. Modelling and control for dynamic positioned vessels in level ice. Proceedings of 8th International Conference on Maneuvering and Control of Marine Craft (IFAC), Casa Grande Hotel, Brazil, pp. 229–236.

Nguyen, D.H., Nguyen, D.T., Quek, S.T., and Sørensen, A.J., 2011. Position-moored drilling vessel in level ice by control of riser end angles. Cold Regions Science and Technology, Vol. 66(2-3), pp. 65–74.

Palmer, A., 1991. Ice forces and ice crushing. Proceedings of 11th International Conference on Port and Ocean Engineering under Arctic Conditions (POAC), St. John's, Canada.

Riska, K., 1987. On the mechanics of the ramming interaction between a ship and a massive ice floe. Ph.D. Thesis, Helsinki University of Technology, Espoo, Finland.

Riska, K., 1995. Models of ice–structure contact for engineering applications. Mechanics of Geomaterial Interfaces, Vol. 42, pp. 77–103.

Riska, K., Wilhelmson, M., Englund, K., and Leiviskä, T., 1997. Performance of merchant vessels in ice in the Baltic. Research Report No. 52, Ship Laboratory, Helsinki University of Technology, Espoo, Finland.

Riska, K., Leiviskä, T., Nyman, T., Fransson, L., Lehtonen, J., Eronen, H., and Backman, A., 2001. Ice performance of the Swedish multi-purpose icebreaker Tor Viking II. Proceedings of 16th International Conference on Port and Ocean Engineering under Arctic Conditions (POAC), Ottawa, Canada.

Riska, K., 2010. Design of ice breaking ships. Encyclopedia of Life Support Systems (EOLSS), Developed under the Auspices of the UNESCO, Eolss Publisher, Oxford, UK. [www. eolss.net].

Riska, K., 2011. Challenges and possibilities in Arctic marine operations. In: J. Grue and R.H. Gabrielsen (eds.), Marine Transport in the high north, Oslo: Novus, Norway.

Runeberg, R., 1888/89. On steamers for winter navigation and ice-breaking. Proc. of Institution of Civil Engineers, Vol. 97, Part III, pp. 277–301.

Saeki, H., Ono, T., Nakazawa, N., Sakai, M., and Tanaka, S., 1986. The coefficient of friction between sea ice and various materials used in offshore structures. Journal of Energy Sources Technology, Vol. 108, pp. 65–71.

Sawamura, J., Tsuchiya H., Tachibana, T., and Osawa, N., 2010. Numerical modeling for ship maneuvering in level ice. Numerical modeling for ship maneuvering in level ice. Proceedings of 20th International Symposium on Ice (IAHR), Lahti, Finland.

Sayed, M., Frederking, R.M.W., and Barker, A. (2000). Numerical simulation of pack ice forces on structures: a parametric study. Proceedings of the 10th International Offshore and Polar Engineering Conference (ISOPE), Seattle, USA, May 28–June 2.

Sayed, M., Kubat, I., and Wright, B., 2011. Numerical Simulations of ice forces on the Kulluk: the role of ice confinement, ice pressure and ice management. OTC Arctic Technology Conference, 3–5 December 2012, Houston, Texas, USA.

Scarton, H.A., 1975. On the role of bow friction in icebreaking. Journal of Ship Research, Vol. 19(1), pp. 34–39.

Shimanskii, Yu.A., 1938. Conditional standards of ice qualities of a ship. Transactions of Arctic Research Institute, Northern Sea Route Administration Publishing House, Vol. 130, Leningrad. Translation T-381-01 by Engineering Consulting and Translation Center (ECTC), P.O. Box 1377, Jackson Heights, New York, NY 11372.

Sodhi, D.S., Takahiro, T., Nakazawa, N., Akagawa, S., and Saeki, H., 1998. Medium-scale indentation tests on sea ice at various speeds. Cold Regions Science and Technology, Vol. 28, pp. 161–182.

Su, B., Riska, K., and Moan, T., 2010a. A numerical method for the prediction of ship performance in level ice. Cold Regions Science and Technology, Vol. 60, pp. 177–188.

Su, B., Riska, K., and Moan, T., 2010b. Numerical simulation of ship turning in level ice. Proceedings of 29th International Conference on Offshore Mechanics and Arctic Engineering (OMAE), Shanghai, China.

Su, B., Riska, K., and Moan, T., 2011. Numerical simulation of local ice loads in uniform and randomly varying ice conditions. Cold Regions Science and Technology, Vol. 65(2), pp. 145–159.

Su, B., 2011. Numerical predictions of global and local ice loads on ships. Ph.D. Thesis, Department of Marine Technology, Norwegian University of Science and Technology, Trondheim, Norway.

Tan, X., Su, B., Riska, K., and Moan, T., 2012. The effect of heave, pitch and roll motions to ice performance of ships. Proceedings of 21st International Symposium on Ice (IAHR), Dalian, China, June 11–15.

Tan, X., Su, B., Riska, K., and Moan, T., 2013. A six-degrees-of-freedom numerical model for level ice–ship interaction. Cold Regions Science and Technology, Vol. 92, pp. 1–16.

Tatinclaux, J. C., 1984. Model tests on two models of WTGB 140-ft icebreaker. U.S. Army CRREL Report, 84–3.

Timco, G. and Sudom, D., 2013. Revisiting the Sanderson pressure – area curve: defining parameters that influence ice pressure. Cold Regions Science and Technology, Vol. 95, pp. 53–66.

Tuhkuri, J., 1996. Experimental investigations and computational fracture mechanics modelling of brittle ice fragmentation. Ph.D. Thesis, Helsinki University of Science and Technology, Espoo, Finland.

USGS, Circum, – Arctic Resource Appraisal Estimates of Undiscovered Oil and Gas North of the Arctic Circle, 2008.

Valanto, P., 1989. Experimental study of the icebreaking cycle in 2-D. Proceedings of 8th International Conference on Offshore Mechanics and Arctic Engineering (OMAE), The Hague, Netherlands, pp. 343–349.

Valanto, P., 1992. The icebreaking problem in two dimensions: experiments and theory. Journal of Ship Research, Vol. 36, pp. 299–316.

Valanto, P., 1993. Investigation of the icebreaking pattern at the bow of the IB kapitan Sorokin on the Yenisei River Estuary in May 1991. Proceedings of 12th

International Conference on Offshore Mechanics and Arctic Engineering (OMAE), pp. 127–134.

Valanto, P., 2001. The resistance of ships in level ice. Transactions of Society of Naval Architects and Marine Engineers (SNAME), Vol. 109, pp. 53–83.

Vance, G.P., 1975. A scaling system for ships modelled in ice. Proc. Society of Naval Architects and Marine Engineers (SNAME), Ice Tech. Symposium, Montreal, Canada, Paper H1, 28pp.

Varsta, P., 1983. On the mechanics of ice load on ships in level ice in the Baltic Sea. Ph.D. Thesis, Helsinki University of Technology, Finland.

Veitch, B., 1995. Prediction of ice contact forces on a marine screw propeller during the propeller-ice cutting process. Acta Polytechnica Scandinavica, Mechanical Engineering Series, issue 118, Finish Academy of Technology, Espoo, Finland.

Vocke, M., Ranki, E., Uuskallio, A., Niini, M., and Wilkman, G., 2011. Experience from Vessels Operating in Ice in the Double Acting Principle. OTC Arctic Technology Conference, 7–9 February 2011, Houston, Texas, USA.

Voelker, R.P. and Geisel, F.A., 1984. Level ice resistance of USCGC Polar Sea in Antarctica. Report No. 872C-2. Arctec, Incorporated.

Wang, S., 2001. A dynamic model for breaking pattern of level ice by conical structures. Ph.D. Thesis, Department of Mechanical Engineering, Helsinki University of Technology, Espoo, Finland.

White, R.M., 1970. Prediction of icebreaker capability. Transactions of RINA, Vol. 112, No. 2, pp. 225–251.

World Energy Outlook (WEO), 2013. Organization for Economic, pp. 708.

Zahn, P.B., Humphreys, D., and Phillips, L., 1987. Full-scale towed resistance trials of the USCGC Mobile Bay in uniform level ice. Transactions of Society of Naval Architects and Marine Engineers (SNAME), vol. 95, pp. 45–77.

Appendix

Paper 1

A six-degrees-of-freedom numerical model for level ice–ship interaction

Xiang Tan, Biao Su, Kaj Riska and Torgeir Moan

Published in *Cold Regions Science and Technology*, Vol. 92(2013), pp. 1–16

Cold Regions Science and Technology 92 (2013) 1–16

Contents lists available at SciVerse ScienceDirect

Cold Regions Science and Technology

journal homepage: www.elsevier.com/locate/coldregions

A six-degrees-of-freedom numerical model for level ice–ship interaction

Xiang Tan [a,*], Biao Su [a,b], Kaj Riska [a,c], Torgeir Moan [a,b]

[a] Centre for Ships and Ocean Structures, Norwegian University of Science and Technology, N-7491, Trondheim, Norway
[b] Department of Marine Technology, Norwegian University of Science and Technology, N-7491, Trondheim, Norway
[c] TOTAL S.A. - DGEP/DEV/TEC/GEO - 06D55, Tour Coupole, 2, Place Jean Millier, La Défense 6 - Cedex 45, 92078 Paris La Défense, France

ARTICLE INFO

Article history:
Received 24 December 2012
Accepted 22 March 2013

Keywords:
Level ice
Ice resistance
Numerical model
Icebreaking pattern
Pressure–area relation

ABSTRACT

A new numerical model simulating ship–ice interaction is proposed in this paper. Since icebreaking is in its nature a three-dimensional nonlinear dynamic problem, the numerical model is developed to look into the intricate interaction process by considering ship motions in 6 degrees of freedom (DOFs). The effect on the icebreaking pattern and ship's performance of ship motions in heave, roll and pitch is investigated. Moreover, pressure–area relation is included in calculating the contact force. Semi-empirical method is used in developing the numerical model and the results are validated by comparing with full-scale data from an icebreaker.

1. Introduction

1.1. Review

Ship–ice interaction is a continuous process during which ship motions and the breaking of ice affect each other. Due to the lack of field observations and the insufficient understanding of the physics of icebreaking especially by moving structures, studies are usually done by combining rational theoretical analysis with information obtained empirically, i.e., semi-empirical methods. Global and local ice load models proposed in previous works (e.g. Daley, 1991; Enkvist, 1972; Kashteljan et al., 1968; Lewis and Edwards, 1970; Lindqvist, 1989; Milano, 1973; Varsta, 1983) describing various aspects of icebreaking process have been implemented by many researchers into numerical procedures. One of the basic assumptions that has commonly been accepted is that the total ice resistance can be taken as the superposition of several force components, i.e., icebreaking force, ice floe turning and submergence force and friction force associated with ice contact, although it could be questionable because the force components could be "complicatedly entangled in each other" (Enkvist et al., 1979). Moreover, since open water resistance is usually very small comparing to ice resistance at icebreaking speeds, the coupling between them could be neglected without causing significant error. Thus, the open water resistance and the pure ice resistance are separable (Riska et al., 1997).

One of the earliest attempts including rational analysis to evaluation of ice resistance is the work by Milano (1973), where ice was assumed to bend in a predictable manner, which was defined by the depth ($C_1 l$) and length ($C_2 l$) of cusps (Fig. 1) evaluated based on plate bending theory and full scale observations. Lewis et al. (1983) conducted a study based on a semi-empirical ice resistance model developed by Naegle (1980) which was in turn a further development of an earlier work carried out by Lewis and Edwards (1970). A large database of model– and full–scale tests was compiled to form the empirical coefficients for the analytical model. Enkvist's (Enkvist, 1972) method for evaluating ice resistance components was used significantly. Varsta (1983) developed a mathematical model analyzing the ice load during level ice–ship interaction process. Several aspects of the icebreaking process, such as average ice pressure formulation, effect of shell stiffness, dynamic bending of ice edge, etc., were especially investigated.

The early mathematical models mentioned above provide approaches to rational analysis of various aspects of the ice load. In general, the results showed good agreements with physical tests, and some of them are still being followed today. However, most of the early models are either based on static analysis of forces (as in Milano's and Lewis's model) or capable of simulating only a short period of time (one icebreaking cycle) or with a too simplified hull and ice edge geometry and contact algorithm.

In recent years, efforts have been put to the modification and refinement of the early models. For example, Valanto (2001a,b) presented a 3D finite element model with the hydrodynamic effects of the water underneath on the bending failure of ice taken into consideration. It was also suggested that the large motion of rotating floes after being bent from the ice cover could be modeled by a mixed Eulerian–Lagrangian formulation, which could further promote the direct calculation of ice floe turning and submergence forces. However, the focus was not yet

* Corresponding author. Tel.: +47 94224670.
E-mail address: tan.xiang@ntnu.no (X. Tan).

0165-232X/$ – see front matter © 2013 Elsevier B.V. All rights reserved.
http://dx.doi.org/10.1016/j.coldregions.2013.03.006

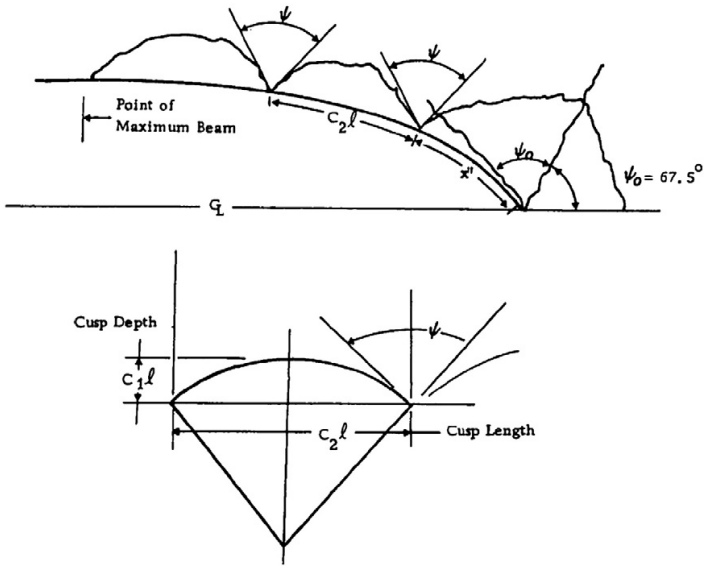

Fig. 1. Idealized bending model of icebreaking (l denotes the characteristic length of ice) (Milano, 1973).

on the study of continuous icebreaking process but on what's going on during one break–displace cycle.

Although the icebreaking cycles are essential elements of the continuous icebreaking process, individual icebreaking events do not act at the same tune. The hull may interact with a pattern of icebreaking, i.e., the process by which a hull's bow opens a sufficiently wide and cleared channel to enable the hull to transit the ice sheet, rather than individual breaking events. Hull motions may affect the cyclic processes by significantly altering contact geometry and loading pattern, resulting in different rates of ice sheet loading. Important noncyclical processes also occur due to non-simultaneous failure of ice around ship's hull (Ettema et al., 1987). These characteristics of icebreaking make it realistic to investigate the problem from a time domain point of view and examine the dynamic process by patterns of icebreaking instead of individual breaking events. Wang (2001) presented a numerical procedure aiming at a time domain solution. The model was based on geometric grid method simulating the continuous contact between a (flexible) fixed conical structure and a moving ice sheet. The work was a continuation of Daley's (Daley, 1991) framework of conceptual ice edge contact model where the ice failure process is, based on observed ice failure events at full scale and model scale, simplified as a nested hierarchy of discrete events including the three continuum processes of crushing, bending and rubble formation. In Wang's work, the focus was on crushing and bending failure, and the process of icebreaking is idealized as successive contact–crushing–bending cycles with predefined bending manner similar to that of Milano (1973). The strategy proposed by Wang (2001) is then followed up by many researchers dealing with different aspects of ships in ice such as dynamic positioning (Nguyen et al., 2009, 2011) and ice resistance and maneuvering (Martio, 2007; Sawamura et al., 2009; Su et al., 2010; Tan et al., 2012, etc.).

1.2. Present work

Since icebreaking is in its nature a three-dimensional nonlinear dynamic problem, it is of interest to look into the intricate interaction process by considering a general picture – that is, a ship moves with 6 degrees of freedom (DOF) – to include the effect of ship motions in heave, roll and pitch on the icebreaking pattern and ship's ice performance.

In this paper, a similar strategy to the one adopted by Wang (2001), which treats the process as successive contact–crushing–breaking cycles, is used; the numerical model is developed by extending the planar model of Su et al. (2010) to a 6-DOF model. First, the continuous icebreaking process is discretized into successive time steps. During each time step, the six coupled dynamic equations of motion for the ship are established, where the icebreaking forces and other external environmental forces are calculated according to the current state variables (orientation, location, velocity and acceleration) of the ship, the current ice edge shape and the ship–ice contact geometry. Then, the equations of motion are solved simultaneously, and incremental displacements are found correspondingly. Since the environmental forces, especially the ice forces, are coupled with the ship's movements, iterations are performed to achieve dynamic equilibrium at each temporal integration point. The state variables of the ship are then updated by the vector sum of the increment and the values at the beginning of the time step. During the icebreaking process, the ship is treated as a rigid body. True geometry of 3D ship hull was modeled using computational geometry methods. Newly formed ice edge due to bending failure is generated according to the indentation of ship's hull into the ice, local contact speed and material properties of ice. The numerical model is implemented into a FORTRAN program. The flow chart of the numerical procedure is illustrated in Fig. 2.

A case study consisting of a series of numerical simulations is then carried out with the icebreaker Tor Viking II. First, simulations with the 6-DOF model are carried out and the results are compared to the full-scale performance data. Then, two reduced-order models are generated by constraining desired degrees of freedom to investigate the effects from ship motions in corresponding directions. Finally, pressure–area relations are implemented to the 6-DOF model to investigate the effect of local contact pressure.

2. Kinematics

2.1. Reference frames

Motions and state variables of the ship and the ice in the model are expressed primarily with respect to two right-handed Cartesian coordinate systems, as illustrated in Fig. 3.

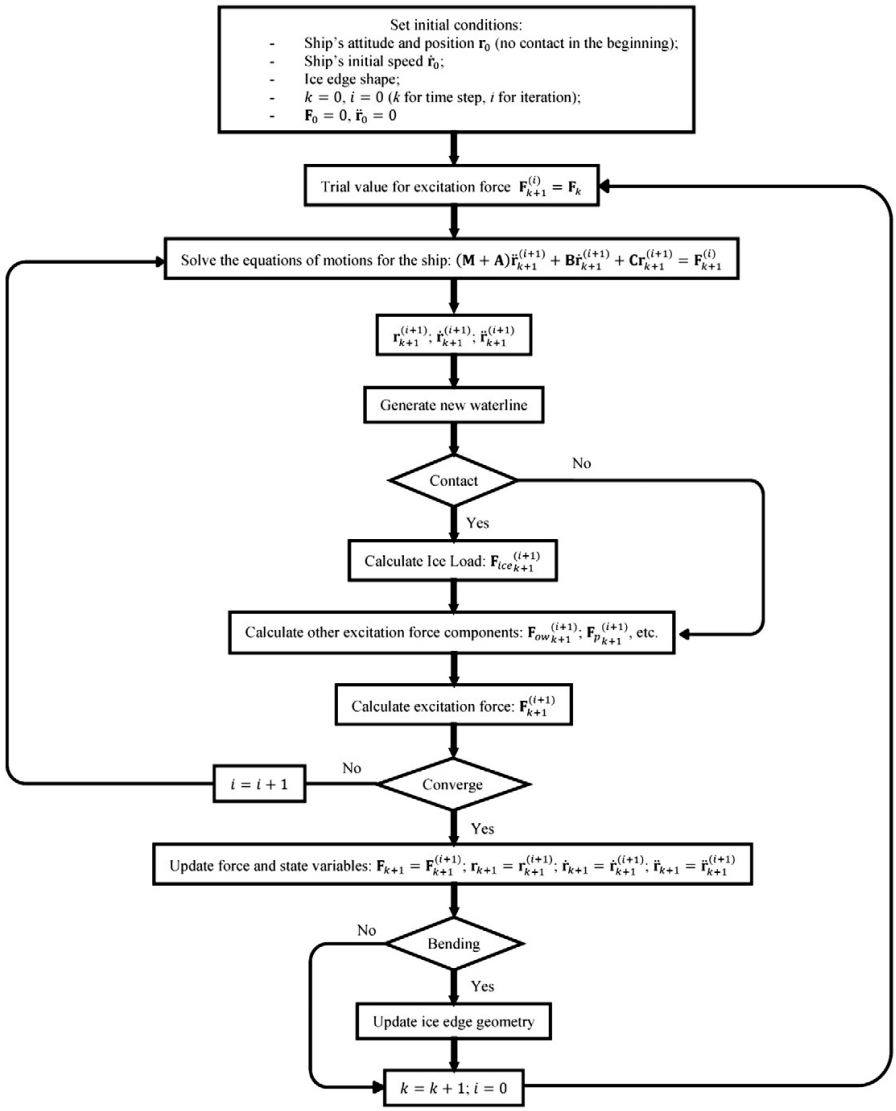

Fig. 2. Flow chart of the numerical procedure.

Earth-fixed frame: The trajectory of ship is expressed with respect to this reference frame, denoted as $\mathbf{x}_0\mathbf{y}_0\mathbf{z}_0$. The coordinates of its origin $\mathbf{O}_0$ could be any prescribed value with the vertical coordinate lying on the calm water plane which coincides with the coordinate plane $\mathbf{x}_0\mathbf{O}_0\mathbf{y}_0$. The ice sheet is defined with its top surface lying on the calm water plane.

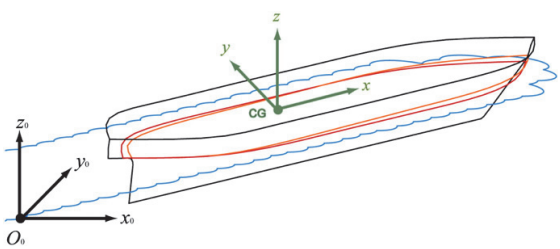

Fig. 3. Reference frames.

Body-fixed frame: Since hydrodynamic properties and inertial coefficients are constant with respect to the coordinate system that is parallel to the principal axes of inertia of the ship, a body-fixed reference frame **xyz** is defined with its origin fixed to the center of gravity (CG) of the ship and body axes **x**, **y**, **z** being longitudinal, transverse and vertical coordinates respectively. Linear and angular velocities and accelerations are expressed in this reference frame. Besides, several local coordinate systems were used to transform the intermediate variables used in the calculation.

The transformation of a vector between **xyz** and $\mathbf{x}_0\mathbf{y}_0\mathbf{z}_0$ is expressed by

$$\mathbf{a}^0 = \mathbf{U} + \mathbf{R}_b^0(\boldsymbol{\Theta})\mathbf{a}^b \tag{1}$$

where,

$\mathbf{a}^0$ and $\mathbf{a}^b$ are the expressions of an arbitrary vector $\mathbf{a}$ in $\mathbf{x}_0\mathbf{y}_0\mathbf{z}_0$ and **xyz** respectively;
$\mathbf{U}$ is the position vector of CG relative to $\mathbf{O}_0$;
$\mathbf{R}_b^0(\Theta)$ is the rotation matrix (Fossen, 2011).
$\mathbf{\Theta} = [\phi,\theta,\psi]$ are Euler angles, roll(ϕ), pitch(θ) and yaw(ψ), specifying the orientation of **xyz** relative to $\mathbf{x}_0\mathbf{y}_0\mathbf{z}_0$.

The relationship between the body-fixed angular velocity ($\boldsymbol{\omega}_{b/0}^b$) and the Euler rate ($\dot{\mathbf{\Theta}}$) is given by the transformation matrix $\mathbf{T}$:

$$\dot{\mathbf{\Theta}} = \mathbf{T}(\mathbf{\Theta})\boldsymbol{\omega}_{b/0}^b \tag{2}$$

where,

$$\mathbf{T}(\mathbf{\Theta}) = \begin{bmatrix} 1 & \sin\phi\tan\theta & \cos\phi\tan\theta \\ 0 & \cos\phi & -\sin\phi \\ 0 & \sin\phi/\cos\theta & \cos\phi/\cos\theta \end{bmatrix} \tag{3}$$

2.2. Ship kinematics, temporal discretization

The continuous icebreaking process is discretized into successive time steps which are short enough so that it can be assumed that the accelerations of ship vary linearly within each time step, thus by integrating accelerations, velocities and displacements are obtained being expressed in a discretized form (Langen and Sigbjornsson, 1977). In this paper, the components of all vectors are organized in the order of surge, sway, heave, roll, pitch and yaw.

The generalized acceleration, velocity and global position and orientation vectors are denoted as

$$\begin{aligned} \ddot{\mathbf{r}} &= [\dot{u},\dot{v},\dot{w},\dot{p},\dot{q},\dot{r}] \\ \dot{\mathbf{r}} &= [u,v,w,p,q,r] \\ \mathbf{r} &= [x,y,z,\phi,\theta,\psi] \end{aligned} \tag{4}$$

according to the nomenclature of SNAME (SNAME, 1950).

By linear acceleration assumption, the acceleration at any time instant τ in the $(k+1)$th time step $\ddot{\mathbf{r}}^k(\tau)$ is given by

$$\ddot{\mathbf{r}}^k(\tau) = \ddot{\mathbf{r}}_k^k + \left(\ddot{\mathbf{r}}_{k+1}^k - \ddot{\mathbf{r}}_k^k\right)\frac{\tau}{h} \tag{5}$$

where,

h is the time step length;
τ is time instant within each time step;

subscript indicates the time step; superscript indicates in which reference system the vector is expressed.

The time integration of Eq. (5) gives incremental velocity:

$$\Delta\dot{\mathbf{r}}^k(\tau) = \int_0^\tau \ddot{\mathbf{r}}^k(\xi)d\xi = \ddot{\mathbf{r}}_k^k\tau + \left(\ddot{\mathbf{r}}_{k+1}^k - \ddot{\mathbf{r}}_k^k\right)\frac{\tau^2}{2h} \tag{6}$$

thus, velocity at any time instant τ in the $(k+1)$th time step is:

$$\dot{\mathbf{r}}^k(\tau) = \dot{\mathbf{r}}_k^k + \Delta\dot{\mathbf{r}}^k(\tau) = \dot{\mathbf{r}}_k^k + \ddot{\mathbf{r}}_k^k\tau + \left(\ddot{\mathbf{r}}_{k+1}^k - \ddot{\mathbf{r}}_k^k\right)\frac{\tau^2}{2h} \tag{7}$$

Displacement could be obtained through a procedure similar to the one stated above:

$$\mathbf{r}^k(\tau) = \mathbf{r}_k^k + \int_0^\tau \dot{\mathbf{r}}^k(\xi)d\xi = \dot{\mathbf{r}}_k^k\tau + \ddot{\mathbf{r}}_k^k\frac{\tau^2}{2} + \left(\ddot{\mathbf{r}}_{k+1}^k - \ddot{\mathbf{r}}_k^k\right)\frac{\tau^3}{6h} \tag{8}$$

By letting $\tau = h$, the velocity and displacement at the end of each time step is obtained:

$$\dot{\mathbf{r}}_{k+1}^k = \dot{\mathbf{r}}_k^k + \left(\ddot{\mathbf{r}}_k^k + \ddot{\mathbf{r}}_{k+1}^k\right)\frac{h}{2} \tag{9}$$

$$\mathbf{r}_{k+1}^k = \mathbf{r}_k^k + \dot{\mathbf{r}}_k^k h + \ddot{\mathbf{r}}_k^k\frac{h^2}{3} + \ddot{\mathbf{r}}_{k+1}^k\frac{h^2}{6} \tag{10}$$

Equilibrium is required at the end of each time step:

$$(\mathbf{M}+\mathbf{A})\ddot{\mathbf{r}}_{k+1}^k + \mathbf{B}\dot{\mathbf{r}}_{k+1}^k + \mathbf{C}\mathbf{r}_{k+1}^k = \mathbf{F}_{k+1}^k \tag{11}$$

where

$\mathbf{M}$, $\mathbf{A}$, $\mathbf{B}$ and $\mathbf{C}$ are the general mass, added mass, damping and restoring force matrices;
$\mathbf{F}$ is the general excitation force vector with $\mathbf{F}(1)$, $\mathbf{F}(2)$ and $\mathbf{F}(3)$ being surge, sway and heave forces, and $\mathbf{F}(4)$, $\mathbf{F}(5)$ and $\mathbf{F}(6)$ being roll, pitch and yaw moments, respectively.

Linear hydrodynamic damping is not included because in ice covered water the ice load is considered to be the most major source of energy consumption.

Solving Eqs. (9)–(11) gives

$$\Delta\mathbf{r}_{k+1}^k = \dot{\mathbf{r}}_k^k h + \ddot{\mathbf{r}}_k^k\frac{h^2}{3} + (\mathbf{M}+\mathbf{A})^{-1}\left(\mathbf{F}_{k+1}^k - \mathbf{C}\mathbf{r}_{k+1}^k\right)\frac{h^2}{6} \tag{12}$$

Finally, state variables are updated and then used as initial values for the next time step:

$$\ddot{\mathbf{r}}_{k+1}^k = \frac{6}{h^2}\left(\Delta\mathbf{r}_{k+1}^k - \dot{\mathbf{r}}_k^k h - \ddot{\mathbf{r}}_k^k\frac{h^2}{3}\right) \tag{13}$$

$$\dot{\mathbf{r}}_{k+1}^k = \dot{\mathbf{r}}_k^k + \Delta\dot{\mathbf{r}}_{k+1}^k \tag{14}$$

$$\mathbf{r}_{k+1}^k = \mathbf{r}_k^k + \Delta\mathbf{r}_{k+1}^k \tag{15}$$

3. Kinetics, modeling the physical process of icebreaking

In order to solve Eqs. (9)–(11) in each time step, the general force vector $\mathbf{F}$ must be found according to the loading state at the current time step. In this paper, the force superposition principle as used by Lindqvist (1989) is followed: by assuming that ice floes are cleared by the advancing hull immediately after being broken from the intact ice sheet, the resistance arises from ice floe clearing and submergence can be considered not to interfere with the subsequent contact. Thus, this component, denoted as $\mathbf{F}^{sbmg}$, can be separated from the total resistance. Similarly, the open water resistance, $\mathbf{F}^{ow}$, is also separated as explained in Section 1.1. Finally, the expression for total resistance of ship in ice can be written as:

$$\mathbf{F} = \mathbf{F}^{brk} + \mathbf{F}^{sbmg} + \mathbf{F}^{p} + \mathbf{F}^{Euler} + \mathbf{F}^{ow} \tag{16}$$

where $\mathbf{F}^{brk}$ is the icebreaking component which accumulates due to crushing until bending failure happens; $\mathbf{F}^{p}$ is propulsion force; $\mathbf{F}^{Euler}$ is a fictitious force induced by a non-uniformly rotating frame (i.e. the body-fixed frame) relative to the inertial frame.

Since the focus of this paper is on the breaking of ice, in the numerical model, $\mathbf{F}^{brk}$, which is the immediate cause for the forming of breaking pattern, is calculated by integrating icebreaking forces along the icebreaking waterline, while other excitation force components are estimated by empirical formula, i.e., without knowing the spatial distribution. For example, the open water resistance is

calculated by crossflow theory given in Faltinsen (1990); $\mathbf{F}^{sbmg}$ is calculated by empirical formula given in Lindqvist (1989); propulsion force is estimated by net thrust in ice.

In this chapter, the numerical method for the realization of the physical process of icebreaking is introduced.

3.1. Geometry model, spatial discretization

When a ship advances into an intact level ice field, the hull at the instantaneous waterline comes into contact with the ice cover edge. Since it is always the waterline that is breaking the ice, the ship's hull, especially the region around the waterline, forms the rigid body boundary condition for ice in the process of icebreaking. At the contact zones along the waterline, individual ice wedges are broken off from the unbroken ice sheet as the ship's penetration increases. The possible contact zones for the ice as well as for the ship hull are found by geometry, i.e., by detecting any contact (or overlap) between the ship's waterline and the ice channel edge (Su et al., 2010).

Numerically, the ship's hull is modeled by spline interpolation based on information from lines drawing. When considering ship's motions in 6 DOFs, one of the important issues is to identify the waterline variation over time, given the ship's global position and orientation. This is done by searching for the intersection between the ship's hull and the water plane. Computational geometry principles (Farin, 1997) are applied to develop a subroutine to discretize the waterline into nodes (Fig. 6) which are updated at each time step according to the ship's current attitude. Ice is discretized into nodes too on the edge based on the ice edge shape from the previous time step or any given initial condition. The nodal model for the calculation of ice–ship interaction is illustrated in Fig. 4.

Once the contact zones are spotted, the local crushing force for each zone is then calculated based on the model of average contact pressure (Riska, 1995):

$$F_{cr} = p_{av} A_{cr} \tag{17}$$

where the local crushing force, F_{cr}, is idealized as the product of the average contact pressure, P_{av}, and the contact area, A_{cr}.

Two cases of contact interface are predefined following Su (2011) (Fig. 5a). In each of the cases, flat hull at contact point is assumed, and the contact area is described by the contact length, L_h, and the indentation depth, L_d:

$$A_{cr} = \begin{cases} \frac{1}{2} L_h \frac{L_d}{\cos\varphi}, & L_d \tan\varphi \le h_i \\ \frac{1}{2}\left(L_h + L_h \frac{L_d - h_i/\tan\varphi}{L_d}\right), & L_d \tan\varphi > h_i \end{cases} \tag{18}$$

where L_h and L_d are determined by contact geometry (Fig. 5b), and φ is the frame angle at the contact point determined by the ship's current attitude.

Frame angles of the waterline nodes are calculated at each time step in compliance with the ship's motions in heave, roll and pitch. In order to get information about the frame angle, φ, i.e., the slope angle, an extra auxiliary waterline below the instantaneous icebreaking waterline is created (Fig. 6) to help in constructing hull panels between the two waterlines. When the size of individual hull panel is small enough (of the order of cm^2), the slope angle, φ, could be represented by the directional cosine between the normal to the hull, **n**, and vertical axis on each waterline node.

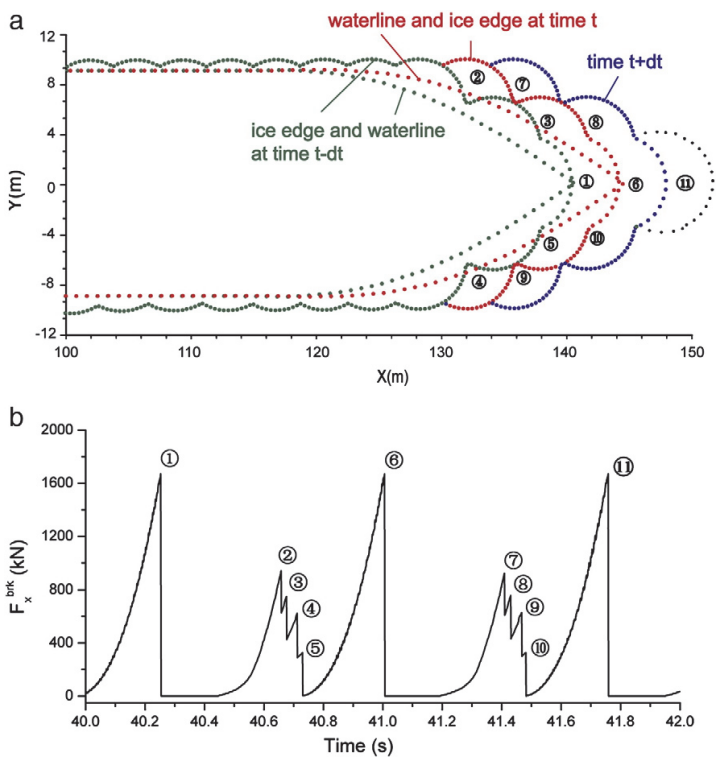

Fig. 4. Example of contact detection procedure (a), and corresponding breaking force (b).

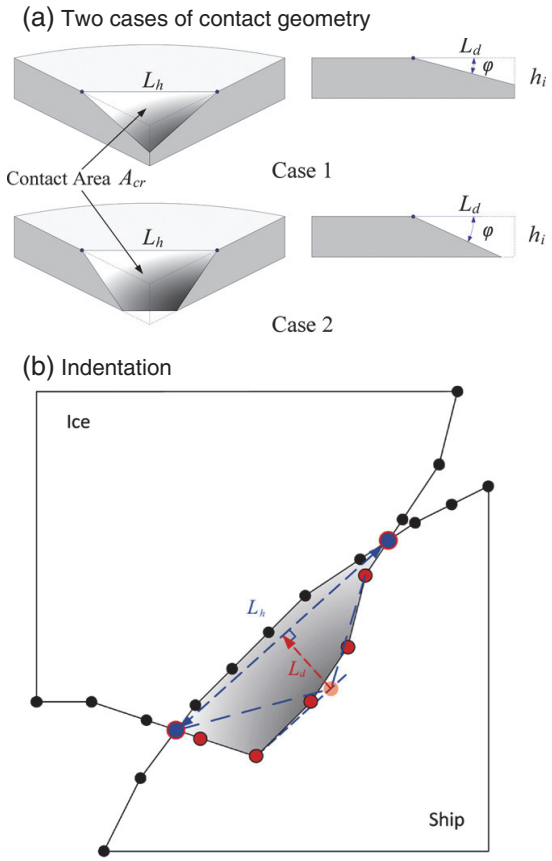

Fig. 5. Idealized contact interfaces (Su, 2011).

Field observations have shown that, when the slope angle of hull at the contact region is smaller than 90 degrees, ice piece with a curved edge is bent down from the intact ice cover as shown in Fig. 7. Then a new edge is formed and will be the basis for the next cycle of contact. In this paper, the shape of broken ice wedge is idealized as an arc whose size and curvature is controlled by the average breaking radius over one contact region. The calculation of breaking radius for an ice cusp was proposed by Wang (2001), where the size of cusp was considered to be dependent on speed, characteristic length of ice and the frame angle.

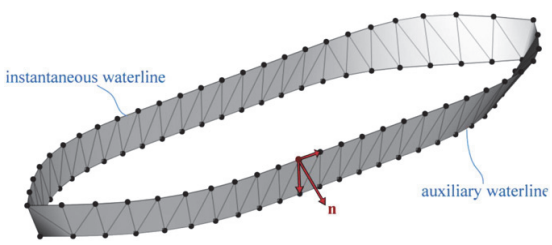

Fig. 6. Frame angle calculation.

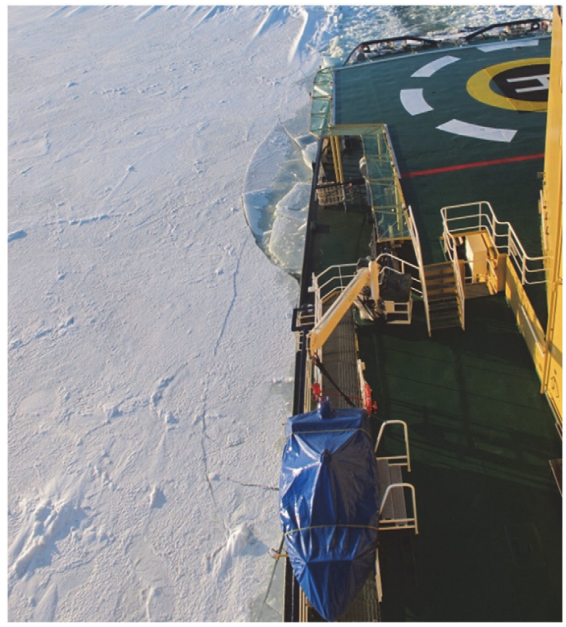

Fig. 7. Observed circular cracks in bending failure onboard YMER in March, 2011 (Photograph by X. Tan).

3.2. Local contact forces

Before the ice edges are bent off from the intact ice cover, local crushing occurs at the contact zones. The global ice load is obtained by integrating local contact loads over the contact zones acting on the ship simultaneously. In the present work, crushing failure is considered to be the most dominant local failure mode in ice, although model tests have shown that shearing or flaking could also occur (Riska, 1995). Fig. 8(a) shows the contact zones that the ship experiences; Fig. 8(b) illustrates the contact forces caused by the relative velocity between ice and hull. In order to calculate the nodal velocity, a local coordinate system is introduced, denoted as $\boldsymbol{\tau n z}$ (Fig. 8(a)). The normal relative velocity, v_2, gives the crushing force, F_{cr}, which is normal to the contact surface. In the contact plane, the tangential relative velocities, v_1 and v_τ, give a vertical and a horizontal frictional force, denoted as f_1 and f_τ, respectively. Compared to the planar model, an extra velocity:

$$v_z = \mathbf{R}^0_{b_{3i}}(\boldsymbol{\Theta})\mathbf{v}_{ship_i}(\dot{\mathbf{r}}) \tag{19}$$

is introduced in the 6-DOF model, which is brought about by the ship's orientation, $\boldsymbol{\Theta}$, and velocities, $\dot{\mathbf{r}}$, in 6 DOFs.

The crushing force, F_{cr}, together with the vertical frictional force component, f_1, contributes a contact force, F_z, pointing upwards, given by

$$F_z = F_{cr}\cos\varphi + f_1\sin\varphi \tag{20}$$

$$f_1 = -\mu F_{cr}\frac{v_n\cos\varphi + v_z\sin\varphi}{\sqrt{v_\tau^2 + (v_n\cos\varphi + v_z\sin\varphi)^2}} \tag{21}$$

Thus the dependency of F_z on the local velocity components is obtained by introducing Eq. (21) into Eq. (20):

$$F_z = F_{cr}\cos\varphi - \mu F_{cr}\frac{v_n\cos\varphi\sin\varphi + v_z\sin^2\varphi}{\sqrt{v_\tau^2 + (v_n\cos\varphi + v_z\sin\varphi)^2}} \tag{22}$$

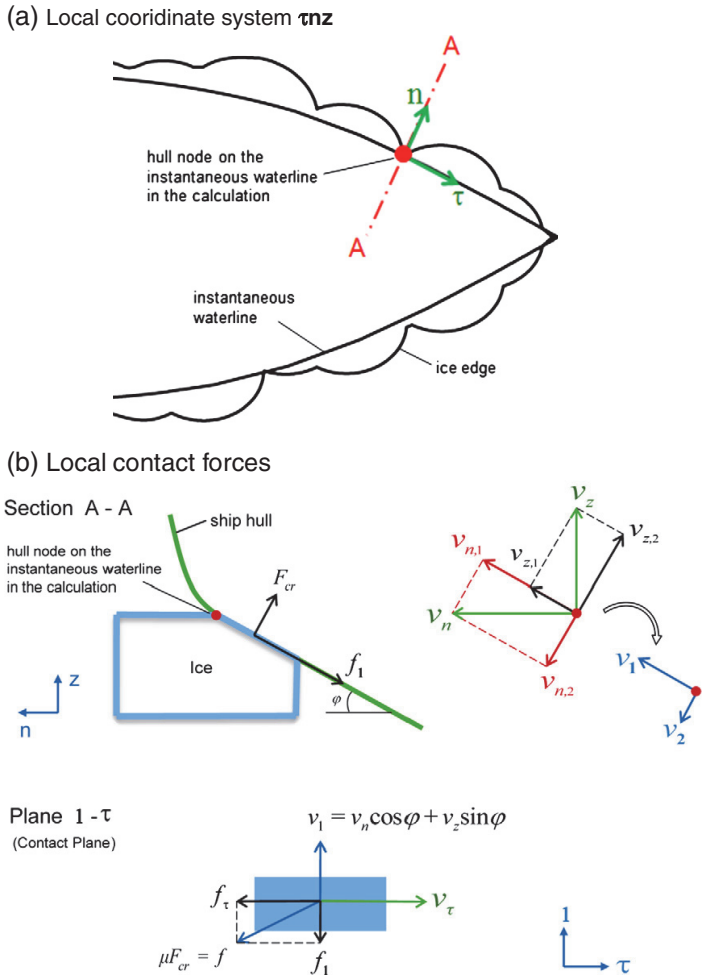

Fig. 8. Contact forces.

3.3. Bending failure criterion

As the ship penetrates further into the ice, the contact area and thus the forces increase. Radial and circumferential micro cracks would develop. This process will continue to the point when F_z, the controlling force in bending cusps off the ice cover, exceeds the bearing capacity, P_f, of the ice edge. Details about the expression for P_f are given by Kerr (1975). Once the ice edge is broken from the intact ice sheet, new ice edge is generated and the next icebreaking cycle begins.

3.4. Pressure–area relation

So far, the numerical model is established by approaches introduced in previous parts of the paper, with a constant contact pressure σ_{cr} being used. It interests the authors at this point to implement a pressure–area (p–a) dependency for local crushing to the established numerical model to examine the effect of p–a relation on ship's ice performance.

Most of the previous mathematical models mentioned in Section 1.1 (Except in Varsta (1983) where the effect of contact length was touched upon) treated the average pressure, P_{av}, in Eq. (17) as a constant evaluated by the crushing strength, σ_{cr}, of ice (the mean value of crushing pressure in Kujala (1994)) for simplicity. However, when considering local ice loads on ship hulls, the pattern of decreasing ice pressure with increasing (nominal) contact area has been observed by compilation of a large amount of in-service data, which implies that local ice loads could not be simply described by a "failure pressure" (Masterson et al., 2007; Sanderson, 1988). Usually, this relationship is given by pressure–area curves which are used as design loads based on the correct use of design area (ISO, 19906, 2010).

Analysis on full-scale measurements in published works show that p–a curves take the form of power relation (e.g. Masterson and Frederking, 1993; Sanderson, 1988):

$$p_{av} = kA_{cr}^{n} \tag{23}$$

where k and n are parameters, and n has a negative value.

Regarding the determination of k, n values, although various suggestions were given in those works based on full-scale data, they are not directly applicable to the numerical model due to the nature of the contact detection algorithm used in the model. In the numerical model, a nominal contact area refers to a geometrical domain without any discontinuity on the waterline, while in reality small gaps on

waterline could exist within one contact area, i.e., geometrical imperfections. The difference in the definition of contact area between the numerical model and full-scale measurements on ship hulls (usually strain gauges with standard sizes) leads to rather different degrees of dependency of average pressure on contact area.

A more relevant contact situation to that in the numerical model is the contact between a plate and a monolithic ice wedge, as is shown in Fig. 5(b). Even for a monolithic ice wedge, the pressure during crushing may not be a constant due to the mechanical properties of ice. Actually this kind of material property is shared by many brittle solids, e.g., in Bienawski (1968) measurements of the compressive strength of coal were done with different sample sizes and the average trend of decreasing strength with increasing area was found. Palmer (1991) proposed a simple mathematical model which quantified the p–a relation based on combination of fracture mechanics model of fragment breaking and fractal hierarchical distribution of fragment size. Since the mechanism of decreasing average pressure with increasing area is not fully understood, the work is carried out semi-empirically and parametric study on k, n values is conducted. Based on comparison of results from several selected k, n values to full-scale measurements, optimum values for the parameters of k and n are suggested and discussions are made in Section 4.4.

As depicted in Fig. 9, a pair of reference values for contact area and corresponding pressure is selected, denoted as A_0 and P_0 respectively. It is assumed that all of the parameterized p–a curves following power relation characterized by Eq. (23) pass through this reference point. Thus, n and k are now dependent on each other, and by varying n (or k) value only, a series of curves are constructed. Apart from simplifying the parametric study, the introduction of reference point is necessary also because a threshold value for contact area needs to be fixed below which the pressure is independent of contact area, implying a transition of material property from being governed by fracture mechanics to strength of material. In this paper, the values of A_0 and P_0 are determined empirically. In the Baltic Sea, the measured average pressure on a gauge with an area of 35×35 cm^2 has a mean value of 2.3 Mpa (Kujala et al., 2007). These values are adopted to represent the reference values in the parametric study. Four sets of p–a curves are calculated with n value equally spaced from -0.1 to -0.4. The case with no p–a relation included is equivalent to the special case when n is equal to 0 (represented by red horizontal line in Fig. 9). In Fig. 9, also marked is the p–a curve given by Palmer's model.

4. Numerical results

In this chapter, a case study is conducted and numerical results are presented. Section 4.1 outlines some parameters and coefficients for the vessel and the ice. In Section 4.2 and Section 4.3, simulations are done using constant contact pressure (σ_{cr}, Table 2); influences of ship motions on ship's ice performance are investigated. In Section 4.4, the numerical results with p–a relation included are presented and comparisons are made to those with constant contact pressure.

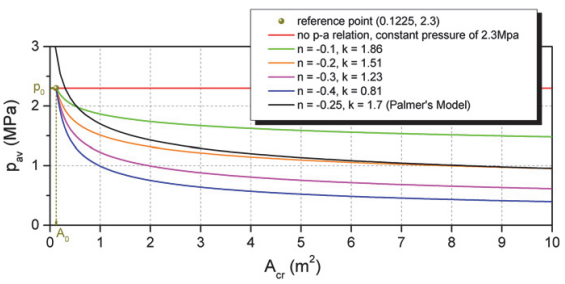

Fig. 9. Pressure–area curves.

Table 1
Ship parameters.

Parameter	Notation	Value	Dimension
Length over all	LOA	83.70	m
L. between perpendiculars	Lpp	75.20	m
Breath, molded	B	18.00	m
Draft, max icebreaking	D	6.50	m
Bollard-pull, ahead	T_B	202	t
Displacement	M	5.74×10^6	kg
Moment of inertia	I_{xx}	2.98×10^8	kg·m^2
	I_{yy}	2.03×10^9	kg·m^2
Added mass coefficients	A_{33}	1.83×10^7	kg
	A_{44}	5.36×10^7	kg·m^2
	A_{55}	4.47×10^9	kg·m^2
Restoring force coefficients	C_{33}	1.31×10^7	N/m
	C_{44}	1.38×10^8	N·m
	C_{55}	6.09×10^9	N·m
Propulsion output	P_D	13,440	kW
Open water speed	v_{ow}	16.40	knot

Since the numerical model is designed including ship motions in all directions, by constraining any of the degree(s) of freedom, reduced-order models can easily be generated. In order to investigate the influence on icebreaking from some specific motion(s), it is natural to follow the idea of elimination, i.e., comparing the results from models with and without the motion(s) in question. In this paper, several configurations are used to conduct numerical experiments on the influence from vertical motions and heading control:

- 6-DOF model, with ship motions in all directions;
- 3-DOF model, with ship motions in surge, sway and yaw, also known as planar model or PMM;
- 4-DOF model, with ship motions in surge, heave, roll and pitch.

Thus, by comparing simulations from the 6-DOF and 3-DOF models, the influences from vertical motions are easier to be analyzed. And also, by comparing results from the 4-DOF and 6-DOF models, added ice resistance from sway and yaw is looked into. Additionally, the model used by Su et al. (2010) is referred to as "previous planar model" in this paper, and is used to verify the 6-DOF model.

4.1. Ship and ice parameters

The Swedish multi-purpose Anchor Handling and Towing Supply vessel/Ice Breaker, AHTS/IB Tor Viking II, is adopted as the physical prototype in this paper to validate the numerical model. The ship parameters and ice properties are listed in Tables 1 and 2. For more information on the ice trials and the ship's operations please refer to Riska et al. (2001).

4.2. Interaction between icebreaking pattern, ship motions and ice resistance

The influence of breaking pattern on ice resistance was observed in Su et al. (2010), where the resistance is not only determined by the ice thickness but by the breaking pattern. In cases where shoulder crushing happens constantly, the ship would experience higher icebreaking resistance (mean value of icebreaking force in surge direction) even in a thin ice thickness. When considering ship's motions

Table 2
Ice properties.

Parameter	Notation	Value	Dimension
Density	ρ_i	880	kg/m^3
Young's modulus	E	5.40×10^9	Pa
Poisson ratio	ν	0.33	
Crushing strength	σ_{cr}	2.30×10^6	Pa
Bending strength	σ_f	0.58×10^6	Pa
Frictional coefficient	μ	0.15	

in 6 degrees of freedom, the varying waterline and frame angle due to ship's vertical motions bring more complexity to the situation by altering the loading condition. In Tan et al. (2012), the interaction between breaking pattern and ship's motions was studied. The loading rates of ice edge are significantly altered by the introduction of the new rate component, v_z, given by Eq. (19). Moreover, the loading rates v_r, v_n and v_z are functions of ship's global orientation ($\boldsymbol{\Theta}$) which causes the change in frame angles, $\varphi(\boldsymbol{\Theta})$, as well as the node's location with respect to CG. All these highly coupled relations on local level make it difficult to express the dependencies explicitly. Numerical models that simulate the dynamic icebreaking process in a continuous mode provide a versatile tool to look into the problem.

A typical simulation result of motions is shown in Fig. 10, where T stands for the period. The undamped natural frequencies for heave, roll and pitch in water can be calculated by Eq. (24) (Lewandowski, 2004):

$$\begin{aligned} T_{03} &= 2\pi\sqrt{\frac{M+A_{33}}{C_{33}}} = 8.5s \\ T_{04} &= 2\pi\sqrt{\frac{I_{xx}+A_{44}}{C_{44}}} = 10.0s \\ T_{05} &= 2\pi\sqrt{\frac{I_{yy}+A_{55}}{C_{55}}} = 6.5s \end{aligned} \tag{24}$$

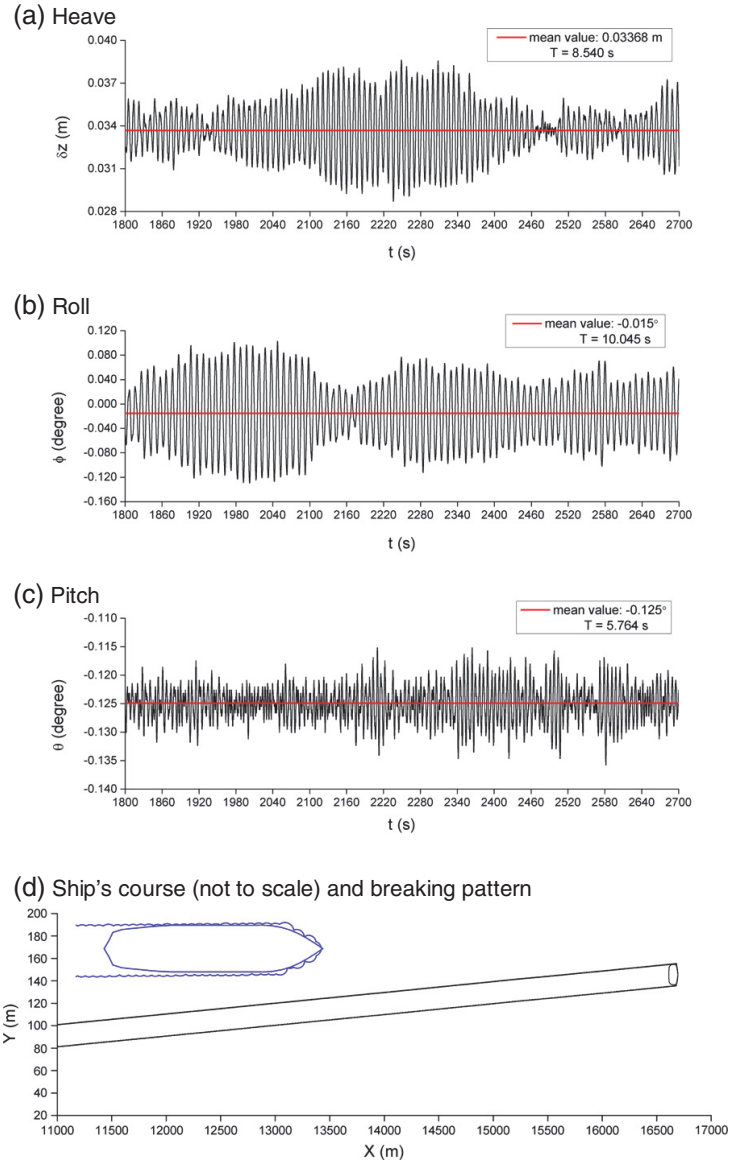

Fig. 10. Simulated motions in ice thickness 0.6 m at full power from 6-DOF model.

When ships advance in level ice, the loading conditions on the port and the starboard side are usually asymmetric due to different loading rates, ship's vertical motions, asymmetric waterline geometry and hull sloping angles. This dynamic effect of breaking pattern–waterline–frame angle interaction usually brings an extra transverse force and yaw moment which cause the ship to drift, as illustrated in Fig. 10(d) (note that in this paper the figures showing the ship's courses are not to scale due to the large aspect ratio as well as the limited space; the figures are only intended to illustrate the trend over a relatively long simulation time). Heading control strategies should be incorporated here to keep the ship going straight ahead (Zhou et al., 2012).

In addition to the influence on the planar motions, breaking pattern will also affect the vertical motions. Fig. 11 shows the results in ice thickness 0.5 m, where the simulated breaking pattern shows a lot of difference to the one in 0.6 m ice: the course of ship (Fig. 11(d)) is much "rougher", and a close-up indicates that the loading regions are more unevenly distributed along the hull, and also shoulder crushing is more severe in this case. The vertical motions in ice thickness 0.5 m have much larger vibration amplitudes although the mean values are lower than those in ice thickness 0.6 m.

Since icebreaking pattern represents a dynamic contact process between ship and ice, time histories of contact loads could also show the

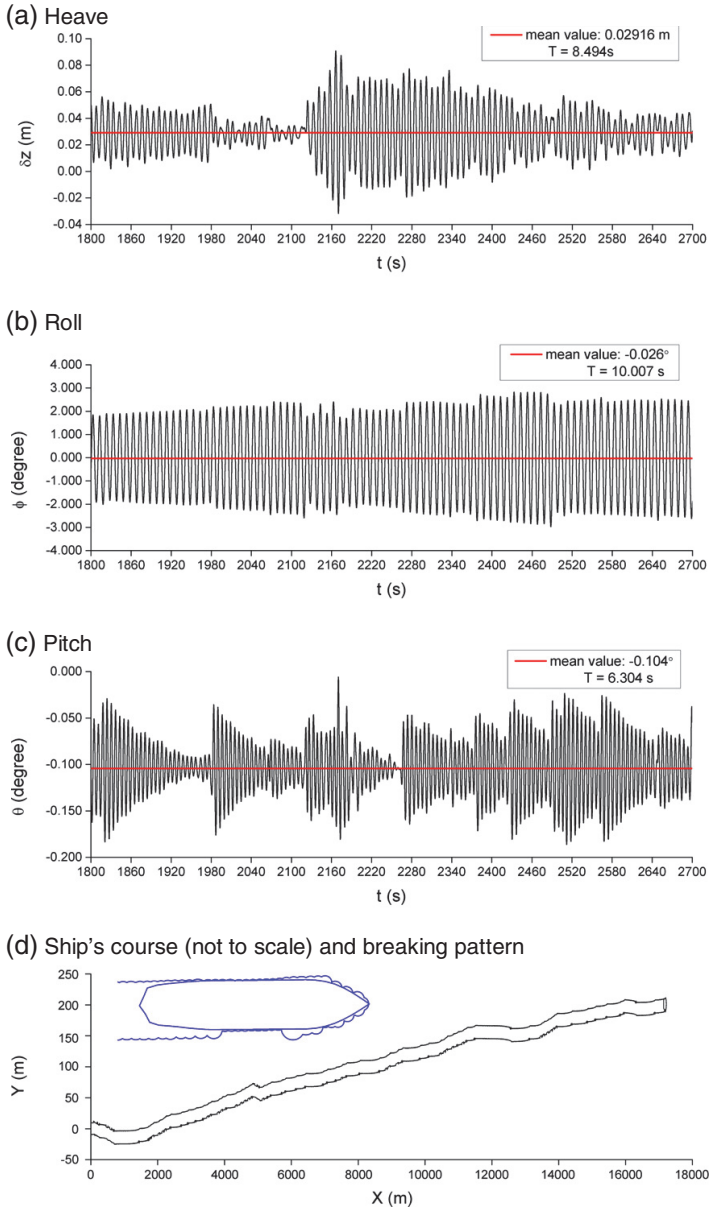

Fig. 11. Simulated motions in ice thickness 0.5 m at full propulsion power from 6-DOF model.

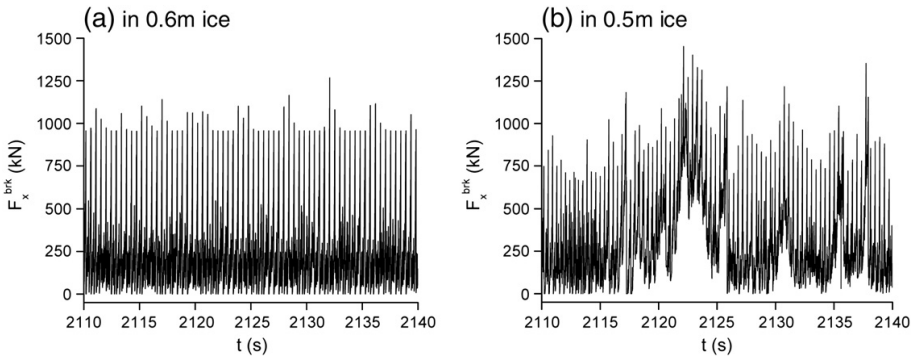

Fig. 12. Comparison of simulated ice breaking force in two cases ((a) in 0.6 m ice; (b) in 0.5 m ice).

difference in characteristics of breaking patterns in terms of the frequencies of different hull regions exposed to contact and the varying breaking radius of ice cusps. Fig. 12 gives the time histories of icebreaking forces in surge direction for ice thicknesses 0.6 m and 0.5 m calculated by 6-DOF model. It is observed that in the case of 0.6 m-thick ice, the curve shows some regularity, while in 0.5 m-thick ice the loading history is more dynamic and irregular. When the ice fails simultaneously around the bow and the channel is sufficiently wide to let the ship transit (Fig. 12(a)), the resistance drops momentarily before subsequently increasing. While in 0.5 m-thick ice, nonsimultaneous failure is dominant, and the breaking force could continue increasing for several seconds before it drops (Fig. 12(b)).

In order to investigate the influence of ship's course on ship motions and resistance, calculations are also done with a 4-DOF reduced-order model by constraining the degrees of freedom in sway and yaw to eliminate the possible drift effect. Since the ship's course in the case of ice thickness 0.4 m shows a clear zigzag pattern, this could become an interesting case for the study of ship course influence. The courses of ship from 6-DOF and 4-DOF model in ice thickness 0.4 m are given in Fig. 13. In contrast to the breaking pattern in the 6-DOF model, the one obtained from the 4-DOF model shows more symmetry and regularity, and shoulder crushing barely happens in this case. The difference in breaking pattern also corresponds to the performance for ice thickness 0.4 m in Fig. 15, where ship speed at full propulsion from the 6-DOF model is a bit lower than that from the 4-DOF model.

The breaking pattern is quite sensitive to the vertical motions for some ice thicknesses. Fig. 14(a) to (c) show the ice edge shapes calculated by the 6-DOF model, the present planar model and the 4-DOF model, respectively, in ice thickness 0.7 m.

Although shoulder crushing (red circles in Fig. 14(a) and (c), and almost the whole parallel body in Fig. 14(b)) is quite severe in all of the models compared to other ice thicknesses, result from the present planar model has much smaller breaking radius than the other two. Actually, in the planar model, the ice along the parallel body is

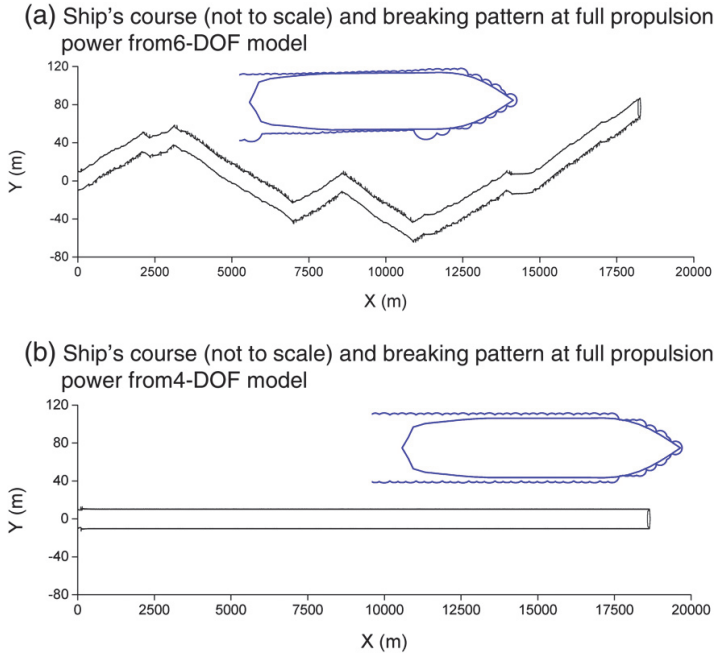

Fig. 13. Comparison of ship courses from 6-DOF and 4-DOF models in ice thickness 0.4 m.

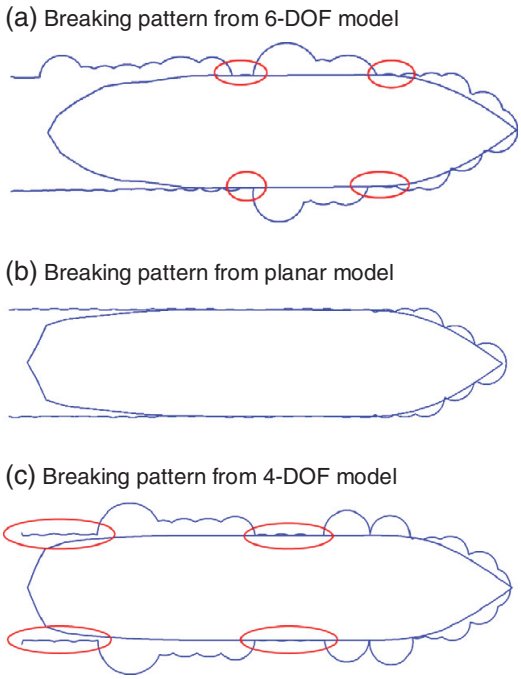

Fig. 14. Breaking pattern in ice thickness 0.7 m at full propulsion power.

broken by crushing only, and the ice edge is almost always flat. It indicates that the introduction of vertical motions, by changing the frame angle and the local velocity, could change the breaking pattern significantly.

4.3. Ship's performance, h-v curve

The *h-v* curve derived from numerical models as well as field data are shown in Fig. 15. Although for most ice thicknesses (except in the case of ice thickness 1.1 m) the ship speeds from 6-DOF model are slightly higher than those from the present planar model, the results from these two models agree well generally. One of the reasons for the higher ship speed in 6-DOF model could be that when there are no extra artificial constraints in the vertical motions, the ship breaks ice in all optimal manners with respect to energy among the 6 DOFs. By comparing the performance with different model configurations (DOFs), the effect of vertical motions on ice performance can be investigated. The higher ship speed obtained in 6-DOF model as compared to the planar model implies that the introduction of vertical DOFs is beneficial to the icebreaking in general. Moreover, this also implies that the numerical method can be used to interpret model tests which are often done with planar models.

As stated in Section 4.2, the ship's performance is influenced by the ship's course, ship's geometry at the waterline, the breaking pattern and consideration of vertical motions. These factors interact with each other too. Regarding comparison between 6-DOF and 4-DOF models, the physical meaning of heading control, i.e., ship's course, and its influence on breaking pattern is the motivation. In several cases, the general trend of higher velocity from 6-DOF as stated in the last paragraph is not followed. The reason could be that although comparing to the 4-DOF model the 6-DOF model has less artificial constraints which means that with more efficient energy use, the relieved DOFs in sway and yaw do not contribute to icebreaking as much as the DOFs in vertical directions do. Actually, when the ship's parallel body is quite vertical (even if the effect of roll is considered) transverse motions could only cause difficulty in icebreaking because ice is more easily bent than crushed. The advantage of energy use in 6-DOF is somehow canceled by the added resistance caused by the ship's drift, as in the case of 0.4 m-thick ice in Section 4.2.

In some cases the h-v curves from the previous planar model and the present planar model show some inconsistency, and the reason could be that the ship's lines are digitized manually by different persons, and the different calculation method of frame angles, which are important factors to change breaking pattern as stated in Section 4.2. It is also noted that the scatter is larger in thicker ice. This is partially due to the fact that the same difference in frame angles gives much larger difference in contact area than in small ice thicknesses. The results given by the present models show a trend of leveling off implying that the speed is more sensitive to ice thickness in thicker ice.

4.4. Effect of pressure–area relation

As shown in Fig. 16, the simulated mean values of vertical motions increase with decreasing *n* value. This effect becomes more obvious in thick ice. Fig. 17 shows the mean values of total ice resistance, and Lindqvist's empirical ice resistance is also calculated and plotted. Similar

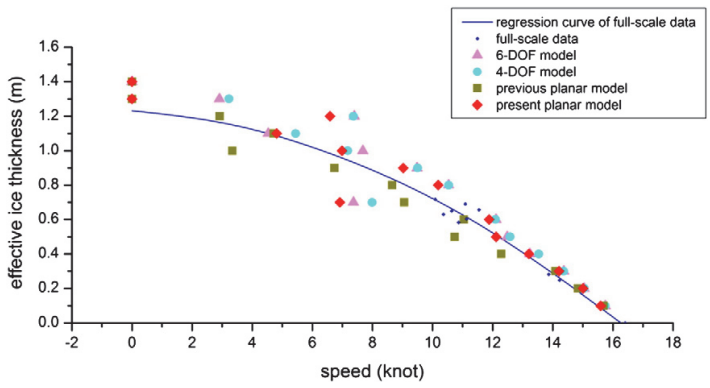

Fig. 15. *h-v* curve.

to the motions, the ice resistance is quite sensitive to p–a dependency especially in thick ice. The reason for the increase in motions and ice resistance is that for a certain contact area, when n value decreases from −0.1 to −0.4, the local contact pressure decreases (Fig. 9). This implies that for a stronger dependency of pressure on contact area (meaning a lower n value), a larger contact area should be attained to produce the force required to fail the ice. Thus for a stronger dependency, the triangular force peaks for the icebreaking force component have a larger area, hence a large energy consumption.

In general, the ship speeds after considering that p–a relations (Fig. 18) are lower than before; ship speeds decrease with decreasing n value due to the same reason stated above. It is also noted in Figs. 17 and 18 that in some cases (e.g. 0.7 m) the results are influenced by breaking pattern and show more irregularity.

A general analysis on information given in Figs. 17 and 18 suggests that the results given by the n values between −0.3 and −0.2 (with a k value between 1.23 and 1.51) show smaller discrepancies to the empirical calculations and field data than the results given by other p–a relations. Moreover, this agrees very well with the k, n values derived by Palmer (1991) introduced in Section 3.4. The results from n values of −0.2 and −0.22 are plotted in Fig. 19 in comparison with the results without p–a relation; generally a smaller discrepancy is achieved especially in thick ice.

5. Conclusions

A numerical model for simulating the ships' performance in level ice including ship motions in 6 DOFs is developed and compared with a previous model for planar motions as well as full-scale ice trial data of the icebreaker Tor Viking II. The model is devised based on similar strategies and assumptions as used in the previous planar model which is extended by including fully coupled 6-DOF motions as well as by considering excitation forces in 3 dimensions. The key issue is to capture instantaneous waterlines and frame angles at each time step based on the true geometry of the ship's hull. Individual ice wedges are assumed to bend in a predefined manner; the icebreaking pattern inherently involves the major assumptions in the analytical treatment of the problem. A slight perturbation to the system may alter dynamic behavior

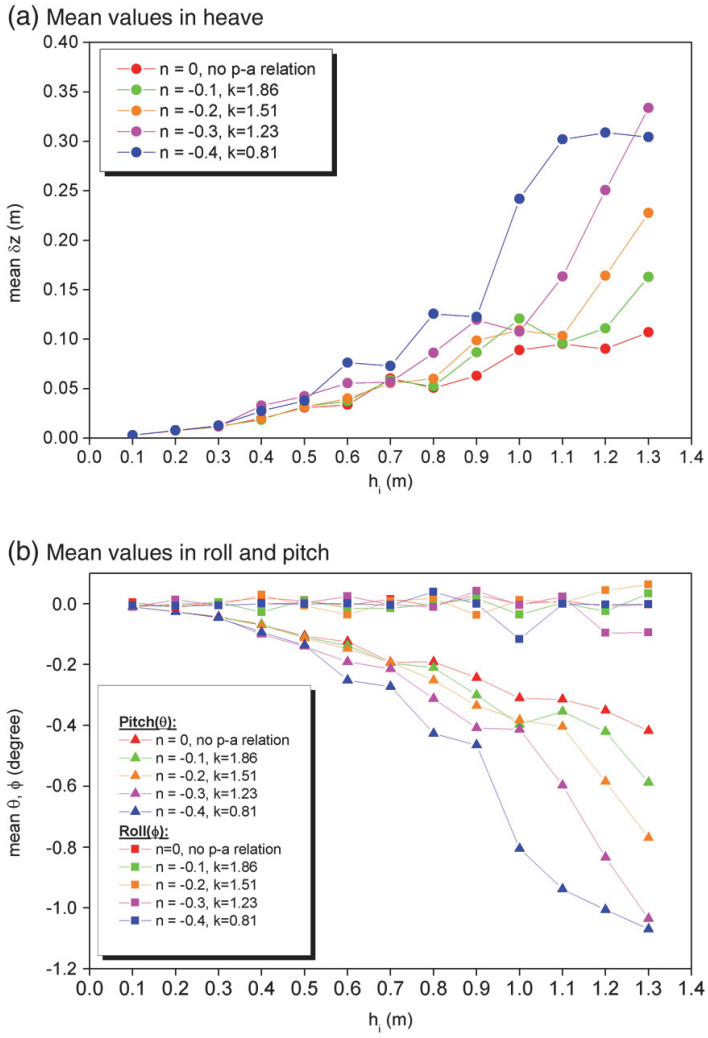

Fig. 16. Mean values of vertical motions.

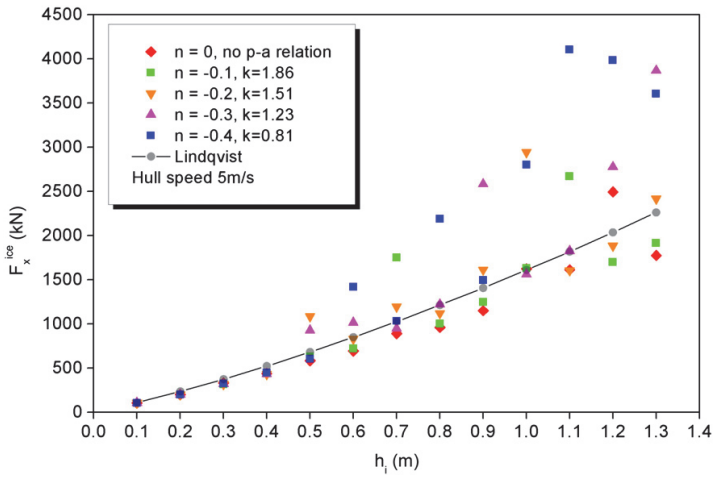

Fig. 17. Mean ice resistance in surge direction at the hull speed of 5 m/s.

significantly. Moreover, the influence of local contact pressure is investigated. Pressure–area curves for local contact are implemented, and parametric study on the degree of dependency is carried out.

The main conclusions are as follows:

(1) As is shown in Fig. 15, for a ship running at full-power, a general trend for the maximum attainable speeds in different ice thicknesses is that the ship's speed decreases with increasing ice thickness. However, icebreaking pattern plays an important, sometimes dominating role in influencing the ship's motions, ice resistance and thus the ship's ice performance. In situations when shoulder crushing is severe (e.g., in the case of 0.7 m thick ice), the ship experiences lower speed than would be expected.

(2) Ship speeds are in most cases slightly higher in the 6-DOF model than the results coming from the 3-DOF model. The explanation of this observation is that relieving artificial constraints on the vertical DOFs is beneficial to breaking of ice since more velocity components have participated in determining the loading rates.

(3) Comparison of results among *p–a* relations (Figs. 16 to 18) shows that ice resistance and mean values of motions increase with decreasing *n* value, i.e., with increasing dependency of contact pressure on contact area. This is because for a stronger dependency, the pressure is lower for the same contact area; since the force required to bend the ice remains the same, a larger contact area has to be attained. Thus the triangular force peaks for icebreaking component have larger area over the contact-break time history, hence larger energy consumption and lower resistance. This trend is more obvious in thick ice due to the fact that a larger contact height (ice thickness) causes bigger change in contact area. Moreover, the breaking pattern effect may even override this trend, for instance in the case of 0.7 m ice.

(4) Inclusion of pressure–area relation would generally result in larger responses and ice resistance. In Fig. 19, it is seen that when *n* value is around −0.2, and *k* is around 1.5, the results show smaller discrepancy to the full-scale regression curve comparing to the results where no *p–a* relation is included, especially for thick ice. These values also agree well with the ones (−0.25 and 1.7) derived in Palmer's model based on fracture mechanics and fractal analysis.

(5) In the real world, the process of icebreaking in level ice includes a breaking pattern of ice which seems quite chaotic (Ettema et al., 1991). The word “chaotic” is chosen because on the one hand, the icebreaking process does evolve a pattern which is followed and repeated during the whole process; on the other hand, the evolved patterns after a long time could be so unpredictable. It is interesting to find that the numerical results for icebreaking pattern somehow show a similar character. It is observed from the simulated results that the evolvement of

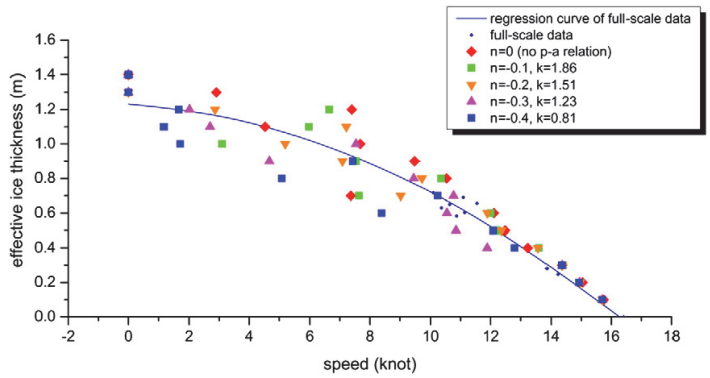

Fig. 18. *h-v* curve with *p–a* relation included.

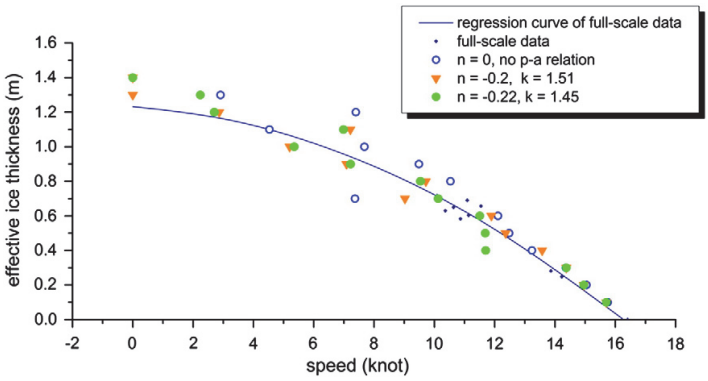

Fig. 19. *h–v* curve with *p–a* relation included.

breaking pattern is so unpredictable, even if the ice is bent in a predefined manner and all of the elements in the model are deterministic since no randomness is introduced to the model. It is also sensitive to initial conditions, e.g., a change in ice thickness could sometimes lead to severe shoulder crushing. Since breaking pattern is important in influencing ship motions and ice resistance, further work needs to be done to look into the characteristics of the chaotic system instead of following the evolution of individual breaking events.

(6) The numerical model is designed in the way that it enables easy generation of derivative models with reduced-order degrees of freedom. By choosing the DOF(s) as needed, not only could the conditions for model tests be realized, but a variety of numerical tests can be conducted. For example, in this paper, a preliminary work is done by using the 3-DOF and 4-DOF models to investigate the effect of vertical motions (heave, roll and pitch) and transverse motions (sway and yaw) on icebreaking. Further work is to be done by first studying influence from each vertical motion and then their coupled effects on breaking pattern, the ship's ice resistance and thus the dynamic process of icebreaking.

Acknowledgments

The discussion with Dr. Yanlin Shao on hydrodynamics and ship modeling is gratefully acknowledged. The authors would also like to acknowledge the Research Council of Norway and the Centre for Ships and Ocean Structures in the Norwegian University of Science and Technology for the funding of the research.

References

Bienawski, Z.T., 1968. The effect of specimen size on compressive strength of coal. International Journal of Rock Mechanics and Mining Engineering 5, 325–335.
Daley, C., 1991. Ice edge contact – A brittle failure process model. Ph.D. Thesis, Laboratory of Naval Architecture and Marine Engineering, Espoo, Finland.
Enkvist, E., 1972. On the ice resistance encountered by ships operating in the continuous mode of icebreaking. Report No. 24. The Swedish Academy of Engineering Science in Finland.
Enkvist, E., Varsta, P., Riska, K., 1979. The ship–ice interaction. Proceedings of POAC 1979. 977–1002.
Ettema, R., Stern, F., Lazaro, J., 1987. Dynamics of continuous mode icebreaking by polar-class icebreaker hull. IIHR Report.Lowa Institute of Hydraulic Research, Lowa City, Lowa.
Ettema, R., Sharifi, M.B., Georgakakos, K.P., Stern, F., 1991. Chaos in continuous-mode icebreaking. Cold Regions Science and Technology 19, 131–144.
Faltinsen, O.M., 1990. Sea Loads on Ships and Offshore Structures. Cambridge University Press, Cambridge, UK.
Farin, G.E., 1997. Curves and Surfaces for Computer-aided Geometric Design – A Practical Guide. Academic Press, New York (429 pp.).
Fossen, T.I., 2011. Handbook of Marine Craft Hydrodynamics and Motion Control. John Wiley & Sons, Ltd., Chichester, UK (596 pp.).
ISO 19906, 2010. Petroleum and Natural Gas Industries — Arctic Offshore Structures.
Kashteljan, V.I., Poznjak, I.I., Ryvlin, A.J., 1968. Ice Resistance to Motion of a Ship. Sudostroyeniye, Leningrad, Russia.
Kerr, A.D., 1975. The Bearing Capacity of Floating Ice Plates Subjected to Static or Quasi-Static Loads-A Critical Survey. Corps of Engineers, U.S. Army, Cold Regions Research and Engineering Laboratory (1975, 43 pp.).
Kujala, P., 1994. Modelling of the ice-edge failure process with curved failure surfaces. Annals of Glaciology 19, 158–164.
Kujala, P., Suominen, M., Jalonen, R., 2007. Increasing the safety of icebound shipping. Final Scientific Report, vol. 1. Ship Laboratory, Helsinki University of Technology, Espoo.
Langen, I., Sigbjornsson, R., 1977. Dynamic Analysis of Structures. Tapir, Trondheim, Norway (505 pp.).
Lewandowski, E.M., 2004. The Dynamics of Marine Craft: Maneuvering and Seakeeping. World Scientific, River Edge, NJ (300 pp.).
Lewis, J.W., Edwards, R.Y., 1970. Methods for predicting icebreaking and ice resistance characteristics of icebreakers. SNAME Transactions 78, 213–249.
Lewis, J.W., Bulat, V., Glen, I.F., Kotras, T., 1983. A semi-empirical ice resistance model, vol. 1, main report. ARCTEC Canada Ltd., Kanata (Ontario).
Lindqvist, G., 1989. A straightforward method for calculation of ice resistance of ships. Proceedings of POAC 1989. 722–735.
Martio, J., 2007. Numerical simulation of vessel's manoeuvring performance in uniform ice. Report no. M-301. Ship Laboratory, Helsinki University of Technology.
Masterson, D.M., Frederking, R., 1993. Local contact pressures in ship–ice and structure–ice interactions. Cold Regions Science and Technology 21, 169–185.
Masterson, D.M., Frederking, R.M.W., Wright, B., Kärnä, T., Maddock, W.P., 2007. A Revised Ice Pressure–Area Curve. Proceedings of POAC, vol. 1. Dalian University of Technology Press, pp. 305–314.
Milano, V.R., 1973. Ship resistance to continuous motion in ice. SNAME Transactions 81, 274–306.
Naegle, J.N., 1980. Ice resistance prediction and motion simulation for ships operating in the continuous mode of icebreaking, Ph.D. Thesis, University of Michigan.
Nguyen, D.T., Sørbø, A.H., Sørensen, A.J., 2009. Modeling and control for dynamic positioned vessel in level ice. Preprints of the 8th IFAC International Conference on Manoeuvring and Control of Marine Craft, September 16–18, 2009. Casa Grande Hotel, Guarujá (SP), Brazil, pp. 229–236.
Nguyen, D.H., Nguyen, D.T., Quek, S.T., Sørensen, A.J., 2011. Position-moored drilling vessel in level ice by control of riser end angles. Cold Regions Science and Technology 66 (2–3), 65–74.
Palmer, A., 1991. Ice forces and ice crushing. The 11th International Conference on Port and Ocean Engineering under Arctic Conditions, St. John's, Canada.
Riska, K., 1995. Models of ice–structure contact for engineering applications. Mechanics of Geomaterial Interfaces 42, 77–103.
Riska, K., Wilhelmson, M., Englund, K., Leiviskä, T., 1997. Performance of merchant vessels in ice in the Baltic. Research report no. 52.Ship Laboratory, Helsinki University of Technology.
Riska, K., Leiviskä, T., Fransson, L., et al., 2001. Ice performance of the Swedish multipurpose icebreaker TOR Viking II. Proceedings of POAC, Ottawa, pp. 849–866.
Sanderson, T.J.O., 1988. Ice Mechanics: Risks to Offshore Structures. Graham and Trotman, London 272.
Sawamura, J., Riska, K., Moan, T., 2009. Numerical simulation of breaking patterns in level ice at ship's bow. Proceedings of ISOPE 2009.
SNAME, 1950. Nomenclature for treating the motion of a submerged body through a fluid, The Society of Naval Architects and Marine Engineers. Technical and Research Bulletin No. 1-5.
Su, B., 2011. Numerical predictions of global and local ice loads on ships, Ph.D. Thesis, Department of Marine Technology, NTNU.
Su, B., Riska, K., Moan, T., 2010. A numerical method for the prediction of ship performance in level ice. Cold Regions Science and Technology 60, 177–188.
Tan, X., Su, B., Riska, K., Moan, T., 2012. The effect of heave, pitch and roll motions to ice performance of ships. Proceedings of IAHR 2012.

Valanto, P., 2001a. The resistance of ships in level ice. SNAME Transactions 109, 53–83.
Valanto, P., 2001b. On the cause and distribution of resistance forces on ship hulls moving in level ice: Proceedings of POAC, Ottawa, Canada, vol. 2, pp. 803–813.
Varsta, P., 1983. On the mechanics of ice load on ships in level ice in the Baltic Sea. Ph.D. Thesis, Helsinki University of Technology, Finland.
Wang, S., 2001. A dynamic model for breaking pattern of level ice by conical structures, Ph.D. Thesis, Department of Mechanical Engineering, Helsinki University of Technology, Espoo, Finland.
Zhou, L., Su, B., Riska, K., Moan, T., 2012. Numerical simulation of moored structure station keeping in level ice. Cold Regions Science and Technology 71, 54–66.

Paper 2

Effect of dynamic bending of level ice on ship's continuous-mode icebreaking

Xiang Tan, Kaj Riska and Torgeir Moan

Revised manuscript submitted to *Cold Regions Science and Technology*.

Effect of Dynamic Bending of Level Ice on Ship's Continuous-Mode Icebreaking

Xiang Tan[1,2*], Kaj Riska[1, 3] and Torgeir Moan[1, 2]

1. Centre for Ships and Ocean Structures
Norwegian University of Science and Technology
N-7491, Trondheim, Norway
2. Department of Marine Technology
Norwegian University of Science and Technology
N-7491, Trondheim, Norway
3. TOTAL S.A. - DGEP/DEV/ED/EC
92400 Paris La Défense – France
* tan.xiang@ntnu.no

Abstract

This paper focuses on the influences of the dynamic effects of ship–ice–water interaction on ship performance, ship motions and ice resistance. The influences of the dynamic bending of ice wedges and ship speeds are especially investigated. The study is carried out using a numerical procedure simulating ship operations in level ice with ship motions in six degrees of freedom (DOFs). A case study is conducted with the Swedish icebreaker Tor Viking II. The 3-D hull geometry of the ship is modeled based on the lines drawing. The predicted performance of the ship is compared with data from full-scale ice trials.

Keywords: numerical model; dynamic bending; ice resistance; ship motions; icebreaking pattern; ship performance

1. Introduction

1.1 Overview of the Dynamic Process of Continuous-Mode Icebreaking

Continuous-mode icebreaking of ships operating in level ice is a process composed of repeated crushing–bending events of the edge of the channel. The ice edge is subjected to contact loads from the ship hull which moves in six degrees of freedom (DOFs). Model- as well as full-scale investigations (e.g., Lewis and Edwards, 1970;

Kotras et al., 1983; Ettema et al., 1987; Ettema et al., 1991; Izumiyama et al., 1991; Valanto, 1993) have shown that the failure of ice by bending and the emergence of a new ice edge follow a seemingly regular pattern comprised of sequential breaking-off of wedge- and cusp-shaped ice pieces from the intact ice sheet. The geometry of the ice edge created by the repeated icebreaking is often referred to as the "icebreaking pattern" (e.g., Fig. 1).

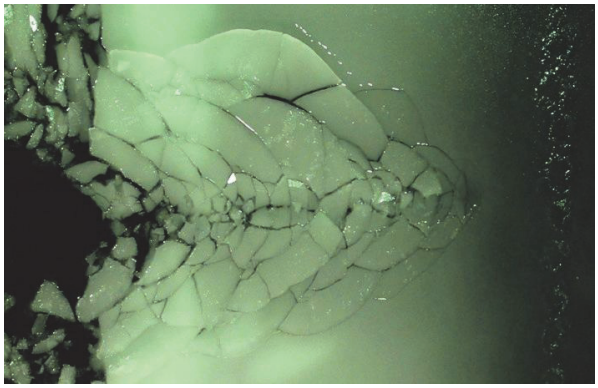

(a) Observed icebreaking pattern in Aalto ice tank in Feb., 2012 (Photograph by X. Tan)

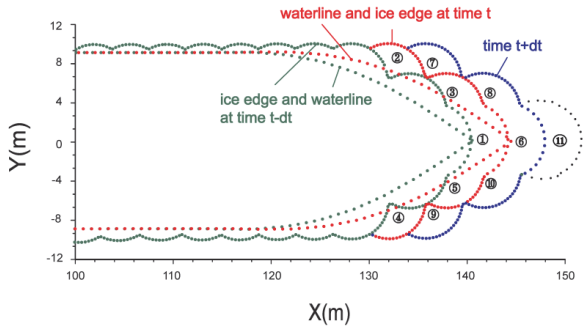

(b) Simulated icebreaking pattern

Fig. 1 Example of the icebreaking pattern

Although the repeating cycles of icebreaking are essential elements to the continuous icebreaking process, individual icebreaking events do not act in unison. The ship hull may interact with a whole pattern of icebreaking rather than the individual events.

Moreover, hull motions shape the process by significantly altering the loading conditions, namely, the loading rates and loading directions.

Due to these characteristics, the ice resistance experienced by a ship, i.e., the mean value of the longitudinal force induced by breaking and clearing the ice, is determined primarily by the way how the ship interacts with the pattern of icebreaking, i.e., by the characteristics of the ship–icebreaking pattern system. To be more specific, ice resistance is influenced by the material properties of ice, hull geometry, ship motions and ship speeds. In nature, these factors are intertwined with each other, which brings more complexity to the dynamic system.

The first ice resistance formulations (e.g., Kashteljan, 1968; Lewis and Edwards, 1970; Enkvist, 1972) used to relate resistance directly to a few "primary parameters" characterizing ice properties (thickness, strength and friction), hull size (beam, displacement, etc.), hull form (stem angle, waterline angle, etc.) and ship speed via single formula. These models have been practical engineering tools for early (performance) design of ice-capable ships and generally achieved passable agreements with full-scale measurements.

However, the detailed ship–ice–water interaction mechanisms from where ice resistance arises are included only when they aid the determination of ice resistance. Designers were forced to treat the problem from a macroscopic point of view (Lewis and Edwards, 1970). Effects such as ship motions, icebreaking pattern, ice friction, local ice pressure distribution and local loading rates were either rarely touched upon or represented by empirical constants implicitly. Moreover, some of the early models could sometimes be too ship-specific to be extrapolated to different types of ships and thus to satisfy the demands for innovative ship (structure) types and optimizing

designs. Later researches have been dedicated to a better understanding of the mechanism and physical nature of the dynamic process of icebreaking (e.g., Varsta, 1983; Riska, 1987; Valanto, 1989; Daley, 1991; Tuhkuri, 1996).

Developments in computational mechanics and graphics have stimulated numerical implementations of mathematical models and made it possible to study the ship–ice–water interaction using bottom-up approaches which enable consideration of detailed ice action mechanisms. Since ice loads are in general both (quasi) periodic and variable, a mean value from analyzing only one icebreaking cycle is not always reliable. Solutions are further sought in the time domain to simulate the whole icebreaking process (e.g., Wang, 2001; Liu, 2009; Aksnes, 2010; Su, 2011; Lubaed and Løset, 2011).

1.2 Present Work

Former time domain simulations simulate the repeating icebreaking process using static bending failure criteria of the ice wedge, where the influence of loading rates on the bending failure load was not taken into consideration.

The dynamic effects of ship–ice–water interaction may be of great significance to the icebreaking process in that the ice bending failure load as well as the size of ice pieces is influenced by local loading rates. Moreover, ship's forward speed together with the size of the ice pieces determines the frequency of load peaks and thus influences the dynamic response of the ship.

This paper focuses mainly on the effect of ship speed dependent phenomena in icebreaking on ice resistance and ship performance in ice. In particular, the effect of dynamic bending of ice wedge due to ship impact is investigated. The investigation is carried out by implementing a dynamic bending failure criterion into a previously

93 developed numerical procedure which simulates the continuous-mode icebreaking in
94 the time domain. This forms the novelty of the paper because a time domain simulator
95 with a dynamic bending failure criterion has not been addressed before. Speed
96 dependence of the icebreaking resistance is investigated using the numerical
97 procedure with a dynamic failure criterion for the bending of the ice edge adopted
98 (referred to as the "dynamic bending model" hereinafter).

99 The numerical procedure, proposed by Tan et al. (2012) and further developed by Tan
100 et al. (2013), simulates continuous-mode icebreaking with ship motions in six degrees
101 of freedom (DOFs). A static bending failure criterion was then used. However, the
102 application of static solutions to icebreaking speeds has been questioned. The inertial
103 force of the ice and the hydrodynamics of the water foundation, which are sensitive to
104 loading rates, are important factors in determining ice bending failure loads and thus
105 ship performance.

106 In this paper, these factors related to the dynamic ice bending are taken into
107 consideration. First, a dynamic bending failure criterion for ice is developed based on
108 the semi-empirical studies provided by Varsta (1983). This is then incorporated into
109 the previously developed numerical procedure. The results from using the dynamic
110 bending model are compared with those from the static model, in a wide range of ice
111 thicknesses and ship speeds. The effects of dynamic bending of ice edge on ice
112 resistance and ship motions are investigated by comparing the results from these two
113 groups of simulations.

114 The main assumptions and simplifications made in the numerical procedure are as
115 follows:

116 1) The force superposition principle is applied

It is assumed that ice floes are cleared by the advancing hull immediately after the bending failure from the intact ice sheet. The resistance from ice floe clearing and submersion is considered not to interfere with the next contact. Similarly, open water resistance is also separated from ice resistance. Thus, the expression for the total resistance of a ship experiences in icebreaking can be written in vector form as:

$$\mathbf{R}_{\mathrm{T}} = \underbrace{\mathbf{R}_{\mathrm{brk}} + \mathbf{R}_{\mathrm{sbmg}}}_{\mathbf{R}_{\mathrm{I}}} + \mathbf{R}_{\mathrm{ow}} \tag{1}$$

where, $\mathbf{R}_{\mathrm{T}}$ denotes the total resistance in ice; $\mathbf{R}_{\mathrm{I}}$ denotes ice resistance; $\mathbf{R}_{\mathrm{sbmg}}$ is the resistance caused by clearance and submersion of broken ice floes; $\mathbf{R}_{\mathrm{brk}}$ is the icebreaking resistance arising from the crushing–bending actions; $\mathbf{R}_{\mathrm{ow}}$ is open water resistance.

The icebreaking force, $\mathbf{R}_{\mathrm{brk}}$, which is the immediate cause for the formation of icebreaking patterns, is calculated numerically by integrating contact forces (obtained via a contact algorithm) along the icebreaking waterline. The magnitude of $\mathbf{R}_{\mathrm{sbmg}}$ is calculated by the empirical formula given by Lindqvist (1989). Propulsion force is estimated by the net thrust in ice, T_{net}, which is determined by bollard pull and ship speeds for a given propulsion power.

2) Ship's open water maneuvering coefficients are constant, i.e., frequency independent.

The total excitation force given by Eq. (1) is then applied to solving the ship's dynamic equations of motion (EOM):

$$(\mathbf{M}+\mathbf{A})\ddot{\mathbf{r}}+\mathbf{B}\dot{\mathbf{r}}+\mathbf{C}\mathbf{r}=\mathbf{F} \quad (2)$$

where, **M**, **A**, **B** and **C** are the mass, added mass, linear damping and hydrostatic restoring force matrices, respectively; **F** denotes the general force vector determined by resistances (as defined in Eq. (1)) and propulsion force.

Eq. (2) is formulated with respect to a ship-fixed coordinate system so that the coefficient matrices are constant. In this paper, the maneuvering coefficients, **M**, **A** and **C**, are calculated by 3-D boundary element method. Linear hydrodynamic damping is not included because in ice covered water, icebreaking is considered to be the major source of energy consumption.

3) Ice is considered as an elastic brittle material due to the high strain rates associated with icebreaking especially at the forebody (Enkvist et al., 1979). Therefore, lateral deflections for the loaded ice wedges are not considered in the contact algorithm. Local failure mode is assumed to be uniform crushing only, although in nature flaking and shearing failures are possible. The ship is considered as a rigid body moves in six DOFs.

2. Numerical Modeling of the Icebreaking Process

2.1 Description of the Icebreaking Process

When a ship is advancing in a level ice field, the hull, especially the forebody (bow), comes into contact with the edge of the intact ice. Local failures such as crushing, shearing or (and) flaking could occur at the loaded areas of the ice edge depending on loading conditions and ice properties. As the ship penetrates continuously into the ice, some loaded sub-areas of the ice edge start to fail in bending when the downward bending loads exceed the bearing capacity of the edge.

161 In most cases, the bow opens a channel wide enough for the maximum beam to pass
162 through. But there are also occasions when bow shoulders or even the side hull of the
163 ship have to force themselves through what is left of the ice edge after the bow
164 breaking. In this situation, i.e., shoulder crushing, the hull behind the bow shoulders is
165 constantly in contact with the ice edge with relatively large contact area and low
166 indenting speed; frictional forces make significant contribution to the ice resistance.

167 Model- as well as full-scale observations have shown that the ice edge breaks in
168 pieces in half moon shape (cusps) as well as in wedge shape (wedges), which leads
169 the continuous icebreaking process to take on some pattern (as shown in Fig. 1). The
170 broken ice pieces could either be cleared aside then pushed under the unbroken ice or
171 simply continue to glide along the bottom line of the ship and emerge again in the
172 channel from behind the ship.

173 **2.2 Introduction to the Contact Algorithm**

174 In this section, the mathematical modeling of the icebreaking process is briefly
175 introduced. A more thorough description is presented by Tan et al. (2013).

176 Two primary coordinate systems are used in the numerical model. One is fixed to the
177 ship, denoted as ***xyz***; the other one is Earth-fixed, denoted as $\boldsymbol{x}_0\boldsymbol{y}_0\boldsymbol{z}_0$.

178 The six coupled dynamic equations of motion given by Eq.(2) are solved by step-by-
179 step integration method; coefficients and variables are organized in matrix and vector
180 form. Iterations are performed during each time step to solve the interaction between
181 the icebreaking force and ship motions. The generalized acceleration, velocity and
182 displacement vectors are denoted as:

183 $$\ddot{\mathbf{r}} = \left[\dot{u}, \dot{v}, \dot{w}, \dot{p}, \dot{q}, \dot{r}\right]$$

184 $$\dot{\mathbf{r}} = [u, v, w, p, q, r] \quad (3)$$

185 $$\mathbf{r} = [x, y, z, \phi, \theta, \psi]$$

186 where, the components are arranged in the order of surge (x), sway (y), heave (z), roll
187 (ϕ), pitch (θ) and yaw (ψ). Newmark's numerical integration scheme (see, e.g.,
188 Langen and Sigbjornsson, 1977) is adopted to solve the dynamic EOM, with
189 modifications made to suit the condition of moving body-fixed frames.

190 In order to solve the dynamic EOM in each time step, the general force vector, **F**, has
191 to be determined first. In the numerical procedure, the icebreaking and crushing force
192 component, $\mathbf{R}_{\text{brk}}$, is calculated by a contact algorithm developed in the previous
193 works (see, Su et al., 2010a; Tan et al., 2012; Tan et al., 2013). First, the instantaneous
194 icebreaking waterline is modeled (Fig. 2); then, overlaps between the waterline and
195 the ice edge are identified as contact zones.

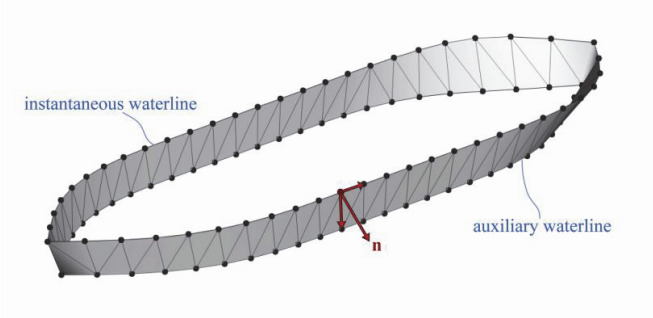

196
197 Fig. 2. Modelling hull form at the waterline

198 Contact area, A_{cr}, for each contact zone is calculated based on the indentation depth,
199 frame angle of the local hull and the ice thickness.

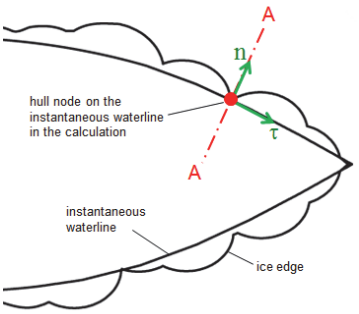

(a). Local contact zone and coordinate system **τnz**

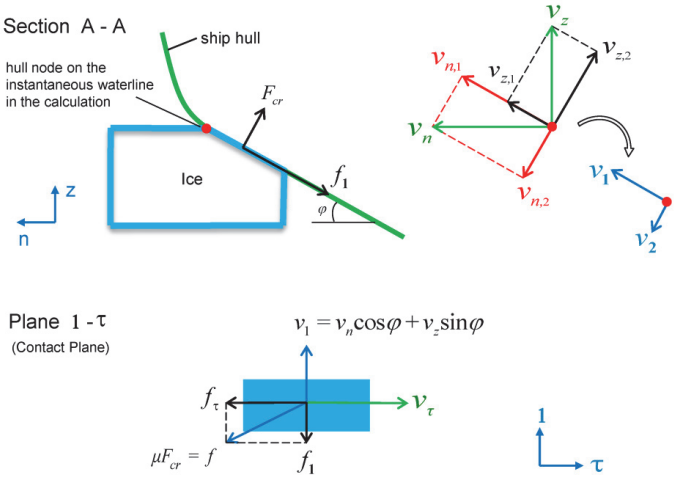

(b). Local contact forces on ship

Fig. 3. Contact

Before analyzing the contact forces, a local coordinate system, denoted as **τnz** (Fig. 3(a)), is introduced to transform the rigid body velocities to hull nodal velocities:

$$\mathbf{v}_i^{\{\tau nz\}} = \begin{bmatrix} v_\tau \\ v_n \\ v_z \end{bmatrix} = \begin{bmatrix} \cos\alpha_i & -\sin\alpha_i & 0 \\ \sin\alpha_i & \cos\alpha_i & 0 \\ 0 & 0 & 1 \end{bmatrix} \begin{bmatrix} v_x \\ v_y \\ v_z \end{bmatrix} = \mathbf{M}(\alpha_i) \cdot \mathbf{v}_i^{\{ship\}} \tag{4}$$

where, α_i denotes waterline angle at node *i*.

209 Eq. (4) is an important relation specifying the transformation from ship's rigid body
210 velocities to local nodal velocities.

211 Then the velocities are decomposed into components that are tangential (v_1) and
212 normal (v_2) to the contact surface, as depicted in Fig. 3(b). As a result, the nodal
213 velocities are expressed in vector form as:

214 $$\mathbf{v}_i^{\{\tau 12\}} = \begin{bmatrix} v_\tau \\ v_1 \\ v_2 \end{bmatrix} = \begin{bmatrix} 1 & 0 & 0 \\ 0 & \cos\varphi_i & \sin\varphi_i \\ 0 & \sin\varphi_i & -\cos\varphi_i \end{bmatrix} \begin{bmatrix} v_\tau \\ v_\mathrm{n} \\ v_\mathrm{z} \end{bmatrix} \tag{5}$$

215 where, φ_i is the frame angle at node *i*.

216 The magnitude of the normal crushing force, F_{cr}, caused by the indentation into the ice
217 edge is determined by the contact area and the average crushing pressure:

218 $$F_{\mathrm{cr}} = \begin{cases} -p_{\mathrm{av}} A_{\mathrm{cr}}, & v_2 \le 0 \\ 0 \quad , & v_2 > 0 \end{cases} \tag{6}$$

219 where, the negative sign means the force is always in the opposite direction to v_2.

220 On the contact plane (plane **1 - τ** in Fig. 3(b)), the tangential relative velocities, v_1 and
221 v_τ, give rise to a vertical and a horizontal frictional force, denoted as f_1 and f_τ,
222 respectively:

223 $$f_1 = \mu F_{\mathrm{cr}} \frac{v_1}{\sqrt{v_\tau^2 + v_1^2}} \tag{7}$$

224 $$f_\tau = \mu F_{\mathrm{cr}} \frac{v_\tau}{\sqrt{v_\tau^2 + v_1^2}} \tag{8}$$

225 The nodal forces on the ship hull expressed in **τnz** are obtained through:

226 $$\mathbf{F}_i^{\{\tau nz\}} = \begin{bmatrix} F_\tau \\ F_n \\ F_z \end{bmatrix} = \begin{bmatrix} 1 & 0 & 0 \\ 0 & \cos\varphi_i & \sin\varphi_i \\ 0 & \sin\varphi_i & -\cos\varphi_i \end{bmatrix} \begin{bmatrix} f_\tau \\ f_1 \\ F_{cr} \end{bmatrix} \quad (9)$$

227 Finally, the force in **τnz**, $\mathbf{F}_i^{\{\tau nz\}}$, is transformed back to ship's coordinate system by:

228 $$\mathbf{F}_i^{\{ship\}} = \mathbf{M}^{-1}(\alpha_i) \cdot \mathbf{F}_i^{\{\tau nz\}} \quad (10)$$

229 The global ice crushing and breaking loads on the ship are obtained by integrating
230 $\mathbf{F}_i^{\{ship\}}$ over all of the contact zones in the current time step.

231 **2.3 Dynamic Bending of Ice Wedge**

232 The forces exerted on the ice wedge by the ship hull are reactions to the forces shown
233 in Fig. 3(b). The normal crushing force, denoted as F'_{cr}, together with the vertical
234 frictional force, denoted as f'_1, gives rise to a vertical force component, F'_z:

235 $$F'_z = -(F'_{cr}\cos\varphi - f'_1\sin\varphi) \quad (11)$$

236 By introducing

237 $$f'_1 = -f_1 = \mu F'_{cr} \frac{v_n\cos\varphi + v_z\sin\varphi}{\sqrt{v_\tau^2 + (v_n\cos\varphi + v_z\sin\varphi)^2}} \quad (12)$$

238 into Eq. (11), and by knowing that $F'_{cr} = -F_{cr} = P_{av} \cdot A_{cr}$, we arrive at:

239 $$F'_z = -\left[\cos\varphi - \mu \frac{v_n\cos\varphi\sin\varphi + v_z\sin^2\varphi}{\sqrt{v_\tau^2 + (v_n\cos\varphi + v_z\sin\varphi)^2}}\right] \cdot P_{av}(A_{cr}) \cdot A_{cr} \quad (13)$$

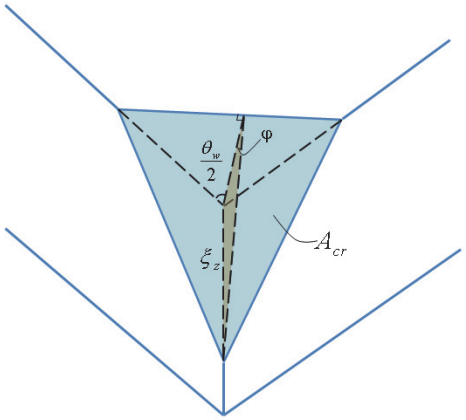

Fig. 4 Illustration of the idealized indentation depth and crushing area

Ice is assumed to be brittle meaning that the lateral deflection is small relative to ice thickness before bending failure happens. The contact area, A_{cr}, could then be expressed by the vertical crushing depth, $\xi_{\mathrm{z}} = \xi_{\mathrm{z}}(\mathbf{v}_i^{\{\tau n z\}})$, and the ice wedge's opening angle, θ_{w}, as (Fig. 4):

$$A_{\mathrm{cr}} = \frac{\tan(\frac{\theta_{\mathrm{w}}}{2})}{\sin\varphi\tan\varphi}\xi_{\mathrm{z}}^2 \tag{14}$$

By inserting Eq. (14) into Eq. (13), a simplified dependence of the vertical load on the vertical crushing depth as well as the local contact velocities are obtained:

$$F_{\mathrm{z}}' = \bar{K}_{\mathrm{d}}(\mathbf{v}_i^{\{\tau n z\}}, \xi_{\mathrm{z}}) \cdot \xi_{\mathrm{z}} \tag{15}$$

where,

$$\bar{K}_{\mathrm{d}} = -\left[\cos\varphi - \mu\frac{v_{\mathrm{n}}\cos\varphi\sin\varphi + v_{\mathrm{z}}\sin^2\varphi}{\sqrt{v_\tau^2 + (v_{\mathrm{n}}\cos\varphi + v_{\mathrm{z}}\sin\varphi)^2}}\right] \cdot \frac{\tan(\frac{\theta_{\mathrm{w}}}{2})}{\sin\varphi\tan\varphi} \cdot P_{\mathrm{av}}(A_{\mathrm{cr}}) \cdot \xi_{\mathrm{z}} \tag{16}$$

252 is the equivalent dynamic stiffness of an ice element defined by two adjacent ice
253 nodes.

254 In the numerical procedure, bending failure of an ice wedge occurs when F_z' exceeds
255 the bending failure load (also known as the bearing capacity), denoted as P_f, of the
256 ice wedge.

257 In the previous works (see, Tan et al., 2012; Tan et al., 2013), a static bending failure
258 criterion was used in the numerical procedure. Field tests have shown that for an ice
259 sheet with a vertical loading on the edge, an increase in the vertical load causes
260 fractures which begin with the formation of radial cracks. The cracks grow in both
261 number and length and propagate from the loaded area into the ice field until the ice
262 ultimately fails due to the formation of circumferential cracks. This character of a
263 semi-infinite ice field loaded on the edge suggests that it is feasible to transform from
264 the plate bending problem to the (non-uniform) beam bending problem (Nevel, 1958)
265 by assuming that the adjacent ice wedges divided by radial cracks are independent.
266 The studies on the static bending failure load for a vertically loaded ice sheet was
267 comprehensively surveyed by Kerr (1975) where the model given by Kashtelyan
268 based on observations was introduced:

269 $$P_f^{static} = c_f \sigma_f h_i^2 (\frac{\theta_w}{\pi})^2 \quad (17)$$

270 Eq. (17) proposed by Kashtelyan is an empirical formula where the static bearing
271 capacity of an ice wedge is proportional to the bending strength (σ_f) and the square
272 of thickness (h_i) of the ice, which is consistent with observations from experiments
273 (e.g., Lau and Williams, 1991) and results given by beam theory. The less studied

factor of wedge geometry was assumed to be represented by the term, $(\frac{\theta_w}{\pi})^2$, where θ_w is the opening angle at the vertex. The non-dimensional analysis thus leaves one empirical coefficient, c_f, to be determined by field tests, in theory.

However, the application of the static bending failure criterion to the icebreaking process is not proper as speeds clearly influence the load. Both experimental and theoretical studies (e.g., Varsta, 1983; Valanto, 1989; Valanto, 1992) imply that the bending failure load of an ice wedge subjected to a rapid loading increases with increasing loading rates. The inertial force of the ice and the hydrodynamics of the water foundation, which are associated with loading rates, influence the ice bending failure load.

When an ice wedge is loaded by an icebreaker hull at a relatively high speed, it is crushed and bent at the same time and obtains an acceleration instantly. This acceleration then causes an effect similar to "slamming", only in this case the water entering object is the ice (see, e.g., Lu et al., 2012). Since water is incompressible, the deflecting ice wedge with certain acceleration causes an increase in the hydrodynamic and possibly hydrostatic pressures in the water foundation. This increased supporting pressure from the water foundation acts in the opposite direction to the hull loading and thus increases the load required for bending failure. The increased water pressure leads to an increased "stiffness" in the loaded ice–water system.

The physical effects taking place during the dynamic bending of the ice wedge are complicated considering the coupling between ice and water. Although simplified solutions have been proposed based on analytical models (e.g. Sørensen, 1977) to account for inertial and hydrodynamic forces by introducing "inertial constants",

297 considering the variation of the added mass of the ice over in time and space, this
298 method has also been questioned (Dempsey and Zhao, 1993).

299 Elastohydrodynamic theory (see, e.g., Fox, 1993; Fox and Squire, 1994; Dempsey et
300 al., 1999; Fox and Chung, 2002; Lubbad et al., 2008) has been drawing more and
301 more attentions due to its ability to include the hydrodynamic effects. But no quickly
302 applicable solutions exist.

303 Varsta (1983) developed a numerical procedure to study the mechanics of ice loads on
304 ships in level ice in the Baltic. In particular, the non-linear dynamic bending behavior
305 of an ice wedge was investigated. Fig. 5 shows a schematic illustration of the ice
306 wedge geometry, which is idealized based on full-scale measurements. The main
307 dimensions are the contact length (l_c), contact depth (l_d) and the wedge angle (φ_w).
308 The normal crushing force applied on the wedge is obtained by the product of the
309 contact area and the average crushing pressure.

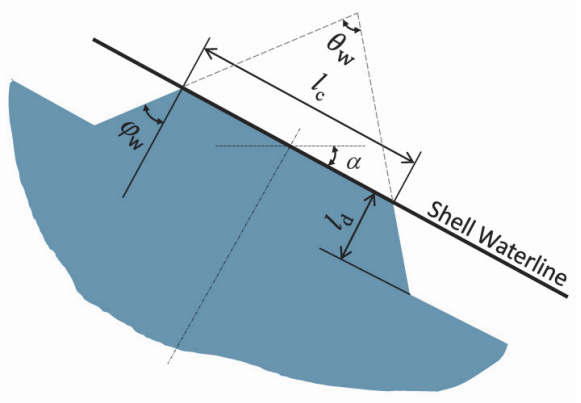

310
311 Fig. 5. Idealized wedge geometry (reproduced from Varsta, 1983)

312 In Varsta (1983), the problem was solved by fluid–structure interaction (FSI) finite
313 element method, which is a finite-element realization of the elastohydrodynamic
314 theory. The ice wedge and the water underneath are fully coupled on the ice–water

interface. Tsai–Wu failure criterion was adopted to define ice failure, with the mechanical constants for a macroscopic failure criterion being determined experimentally by the procedure developed by Riska (1980).

The calculation results were compared with full-scale tests of ice impact on a landing craft bow, which was especially designed to measure the dynamic ice loads. The calculation results along with the test data are shown in Fig. 6. Although the measured ice failure loads show quite a scatter, the average values correlate well with the calculated curves. The calculated curves and the measured data show that bending failure loads increase with increasing loading rates.

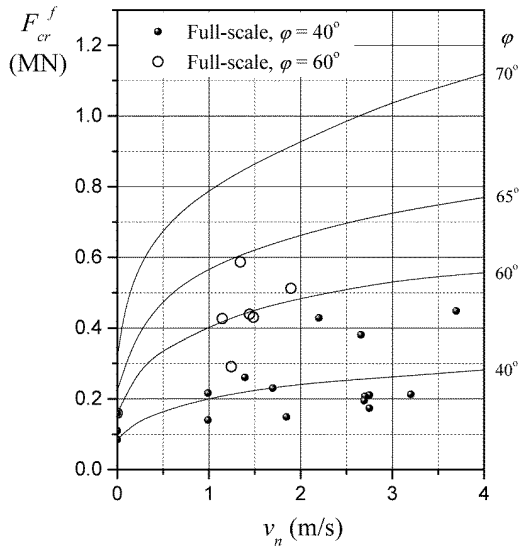

Fig. 6. Normal crushing force at failure vs. ship speed (reproduced from Varsta, 1983. Notations for force, speed and frame angle are changed to be consistent with the present work)

The information given by Fig. 6 is processed in the present work to formulate the dependence of ice bending failure load on loading rates. The procedure is given in the forthcoming part.

By using the relationships:

$$P_{\mathrm{f}} = F_{\mathrm{cr}}^{\mathrm{f}} \cos\varphi - \mu F_{\mathrm{cr}}^{\mathrm{f}} \sin\varphi \tag{18}$$

$$v_2 = v_{\mathrm{n}} \sin\varphi \tag{19}$$

the dependence of the vertical load at failure, P_{f}, on normal relative speeds, v_2, for different frame angles is obtained, as presented in Fig. 7. It is shown in Fig. 7 that the $P_{\mathrm{f}} - v_2$ relations for the four tested frame angles (40°, 60°, 65°, 70°) are very close to each other. Thus, it seems justified to believe that the v_2 dependence of P_{f} for different frame angles can be reduced to a common base (the "average" curve in Fig. 7) which is independent of frame angles.

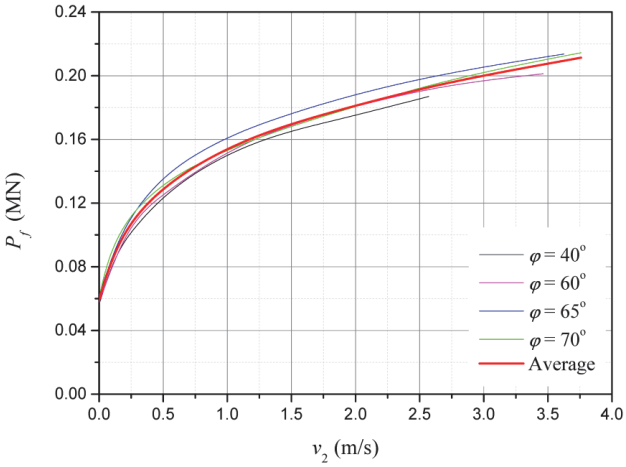

Fig. 7. Vertical failure load vs. normal relative speeds

Then, a non-dimensional analysis is carried out assuming, based on the static model proposed by Kashtelyan, that the dynamic bearing capacity, P_{f}, is proportional to the bending strength (σ_{f}), the square of thickness (h_{i}^2) of the ice and the geometry factor, $(\frac{\theta_{\mathrm{w}}}{\pi})^2$, specifying the wedge size in the circumferential dimension. The result is then a dimensionless coefficient function of the normal relative speed, defined as:

$$\lambda_t(v_2) = \frac{P_f(v_2)}{\sigma_f h_i^2 \left(\frac{\theta_w}{\pi}\right)^2} \tag{20}$$

λ_t is plotted versus v_2 in Fig. 8.

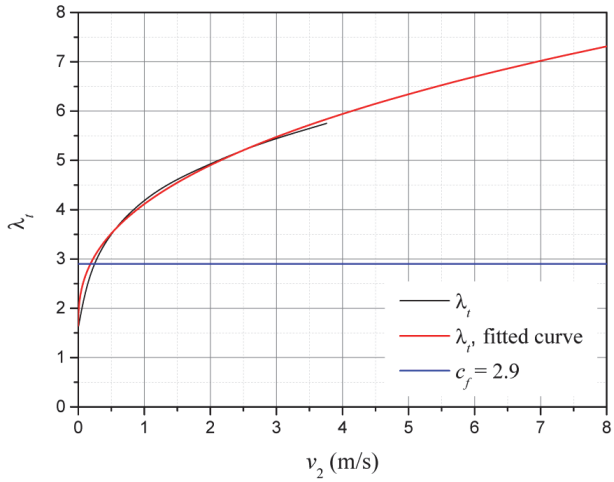

Fig. 8. Coefficient λ_t as a function of crushing speed v_2 (h_i=0.35m, σ_f = 1.2MPa, $\theta_w = 90^o$)

After curve fitting for λ_t shown in Fig. 8, Eq. (20) is then expressed numerically as:

$$P_f(v_2) = (1.65 + 2.47 v_2^{0.40}) \sigma_f h_i^2 \left(\frac{\theta_w}{\pi}\right)^2 \tag{21}$$

Eq. (21) is used as the dynamic bending failure criterion and implemented into the numerical procedure to investigate the speed effect on icebreaking resistance and ship motions. It should be noted that Eq. (21) is a semi-empirical formula based partially on finite element method and partially on physical tests.

2.4 Icebreaking Pattern

In the present work, individual ice wedges are assumed to bend in a predefined manner. A series of successive individual icebreaking events develop a pattern of

361 icebreaking which interacts with the motions of the ship and influences the resistance
362 a ship experiences. The icebreaking pattern involves some major assumptions in the
363 analytical treatment of the bending problem. Both full-scale and model-scale data (see,
364 e.g., Lewis and Edwards, 1970; Enkvist, 1972; Varsta, 1983) suggest that the size of
365 broken ice pieces generally decreases with increasing ship speeds and increases with
366 increasing ice thicknesses. This is attributed to the fact that the loaded end of the ice
367 beam, as compared to the location that is far away from the free end, receives less
368 support from the dynamic water flow underneath (because the water underneath the
369 loaded free end is under free surface condition). When loaded at higher rates, the
370 location where maximum bending moment occurs in the ice beam moves closer to the
371 end. In addition to ship speeds and ice properties, the size of broken ice pieces is also
372 influenced by the bow form of the ship. In Wang (2001), a relationship describing the
373 geometry and the size of the ice floe was proposed with rational justifications.
374 Comparison was made with test data given by Izumiyama et al. (1991). Based on the
375 studies of Enkvist (1972) and Varsta (1983), Wang (2001) suggested that the shape of
376 the circumferential bending crack can be modeled as a circular arc and the size of the
377 broken ice floe be controlled by the quantity "ice floe radius", which is expressed as:

378 $$R = C_{\mathrm{l}} l (1 + C_{\mathrm{v}} v_2) \tag{22}$$

379 where, l is the characteristic length of the ice; C_{l} and C_{v} are empirical constants.

380 Static theory of a plate on elastic foundation gives the solution of l as:

381 $$l = \left(\frac{E h_{\mathrm{i}}^3}{12(1-\nu^2)\rho_{\mathrm{w}} g}\right)^{\frac{1}{4}} \tag{23}$$

382 It is shown theoretically in Fox (2001) that the characteristic length derived from
383 static cases gives the appropriate length scale for both static and dynamic responses.

384 In nature, the crack shape could be more complicated and radial cracks could happen.
385 Based on previous studies (Tan et al., 2012; Tan et al., 2013), the authors believe that
386 Eq. (22) is able to describe the most typical shape of the bending cracks observed in
387 physical tests. The two major factors – loading rates and ice thicknesses – are taken
388 into account empirically by tuning the empirical constants C_1 and C_v.

389 The shape of the ice edge in contact with the hull can be quite irregular, which has
390 been observed in icebreaking patterns from both nature and numerical simulations.
391 The "ice floe radius" model given by Wang (2001) specifies only one dimension (the
392 radial, or, the depth) of the broken floe. In the present paper, an additional relationship
393 is used together with Wang's model to describe the geometry by which the ice cover
394 fails. Milano (1973) suggested, based on full-scale tests, that the ratio between the
395 length (denoted as $c_2 l$ in Fig. 9) and the depth (denoted as $c_1 l$ in Fig. 9) of the cusp
396 for sea ice ranges from about 3 to 6.

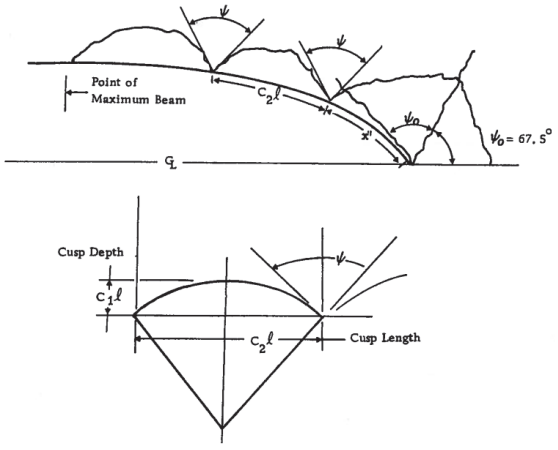

397
398 Fig. 9 Example of icebreaking pattern (Milano, 1973)
399 (l denotes the characteristic length of ice)

In this paper, a coefficient C_r, following Milano (1973):

$$C_r = \frac{c_2 l}{c_1 l} \tag{24}$$

is introduced to represent the length-to-depth ratio of broken ice cusps.

Thus, based on the length and depth of the ice floe, the ice edge in contact with ship hull will be deleted if the vertical load exceeds the dynamic bending failure load developed in Section 2.3. A new edge will be generated by interpolating an arc at the location of the circumferential crack.

3. Numerical Results

3.1 Ship and Ice Properties

The ship parameters and ice material properties adopted in the numerical model are listed in Table 1 and Table 2.

Table 1. Ship parameters

Parameter	Notation	Value	Dimension
Length over all	*LOA*	83.70	m
Length between perpendiculars	*L*pp	75.20	m
Breath, moulded	*B*	18.00	m
Draught, max icebreaking	*D*	6.50	m
Bollard pull, ahead	T_B	202	t
Displacement	*M*	5.74×10^6	kg
Moment of inertia	I_{xx}	2.98×10^8	$kg\cdot m^2$
	I_{yy}	2.03×10^9	$kg\cdot m^2$
Added mass coefficients	A_{33}	1.83×10^7	kg
	A_{44}	5.36×10^7	$kg\cdot m^2$
	A_{55}	4.47×10^9	$kg\cdot m^2$
Restoring force coefficients	C_{33}	1.31×10^7	N/m
	C_{44}	1.38×10^8	$N\cdot m$
	C_{55}	6.09×10^9	$N\cdot m$
Propulsion output	P_D	13440	kW
Open water speed	v_{ow}	16.40	knot

412 Table 2. Ice properties

Parameter	Notation	Value	Dimension
Density	ρ_i	880	kg/m^3
Young's modulus	E	5.40	GPa
Poisson ratio	ν	0.33	
Crushing strength	σ_{cr}	2.30	MPa
Bending strength	σ_f	0.58	MPa
Coefficient of friction	μ	0.15	

413

414 **3.2 Ship Performance**

415 The numerical predictions of ship performance with the static and the dynamic
416 bending models are shown in Fig. 10 and Fig. 11, where full-scale measurements are
417 also included. It is shown in Fig. 10 that the *h–v* curve derived by the dynamic
418 bending model correlates better to full-scale curve than the static one, especially in the
419 cases where ice thickness is above 0.4m. It is also noticed in Fig. 11 that in very thick
420 ice (1.1m and 1.2m), the resistance given by the static bending model is much higher
421 (ship speed gets much lower) than that given by the dynamic bending model. This can
422 be attributed to the fact that thick ice corresponds to low ship speeds and thus low
423 normal speed for local impact, given an certain propulsion power. According to Fig. 8,
424 the bending failure load given by the dynamic bending model is more sensitive to
425 loading rates at the low velocity range. The dynamic modulation could result in a
426 lower bending failure load than given by the static bending model.

427 In the case of ice thickness 0.6m, the result for ship speed diverges from the others. A
428 closer examination of the breaking pattern shows a large contact area between the
429 parallel midbody and the ice edge. Due to the large frame angle (nearly vertical) at the
430 side hull, ice is continuously crushed rather than fail in bending. The corresponding
431 high ice resistance shown in Fig. 11 indicates the "shoulder crushing" effect.

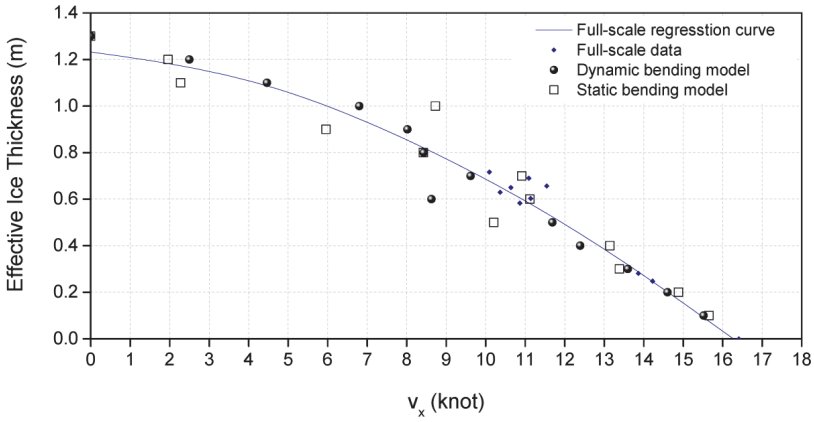

Fig. 10. *h*–*v* curve

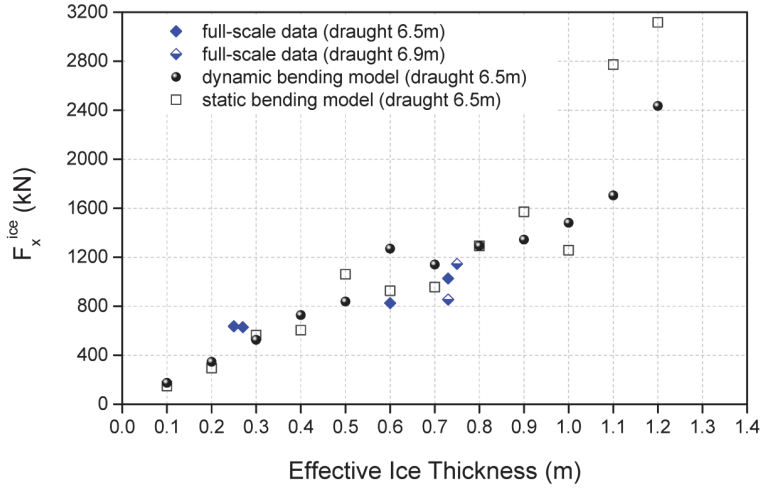

Fig. 11. Mean surge ice resistance at full propulsion power

It is worth noticing that in Fig. 8, the value of λ_t for zero speed (1.65), which seems supposed to correspond to the static case, is not equal to the c_f value used in the static model (which is 2.9), as may be expected. Technically, the c_f value is to be obtained either by direct field tests or by tune-up according to measurements (e.g., *h*–*v* curve and ice resistance as shown in Fig. 10 and Fig. 11) or at least some analytical resistance formulae. Especially, when developing numerical models, tuning is

commonly used due to insufficient field data and the complexity in conducting such measurements as the one conducted by Varsta (1983) with special designed set-up.

A literature study reveals a quite a big scatter of c_f values in former works. For example, Kashtelyan, who proposed the static bending failure criterion, used a value of 1.04 (Kerr, 1975); in Wang (2001) the same value was used for a wedge with apex angle of 90^o; while Nguyen et al. (2009) adopted a value of 4.5 and the calculations were validated with Lindqvist's resistance model; in Su et al. (2010a) a value of 3.1 was selected by validation with Lindqvist's resistance model too; in a later work, Su et al. (2010b) readjusted it to 2.9 by validation with full-scale measurements and this is then followed by Tan et al. (2012). The scatter implies that the numerical adjustment of c_f were made to agree with either full-scale measurement, where the influence of dynamic bending is already included in the measured results, or with empirical resistance formulae, where many details of the icebreaking cycle discussed in Chapter 2 were roughly represented by a few main particulars of ships.

Thus, it is reasonable to believe that the c_f values suggested by former works mentioned above is a result of balancing calculation results over the particular speed ranges associated with each model. In other words, for each of the numerical simulations listed above, the loading rates encountered may lie in different speed ranges in Fig. 8, which gives quite scattered c_f values.

3.3 Mean Ice Resistance vs. Ship Speed

For ship design, it is practical to relate the mean value of resistance to ship speeds as well as other primary parameters of ice and hull geometry. Regression analysis and dimensional studies typically include the ship speed effect by relating mean ice

resistance (or its components) to Froude numbers based on ice thickness or (and) ship waterline length (e.g. Lewis et al., 1982; Lindqvist, 1989). For example, Lindqvist (1989) proposed an ice resistance formula:

$$F_{\mathrm{x}}^{\mathrm{ice}} = (F_{\mathrm{c}} + F_{\mathrm{b}})(1 + 1.4F_{\mathrm{n}}^{\mathrm{h}}) + F_{\mathrm{s}}(1 + 9.4F_{\mathrm{n}}^{\mathrm{L}}) \tag{25}$$

which accounted for hull speed effect by multiplying static ice resistance components for crushing, breaking and submersion, denoted as F_{c}, F_{b} and F_{s}, respectively, by Froude numbers, $F_{\mathrm{n}}^{\mathrm{h}}$ and $F_{\mathrm{n}}^{\mathrm{L}}$:

$$\begin{aligned} F_{\mathrm{n}}^{\mathrm{h}} &= \frac{v_{\mathrm{x}}}{\sqrt{g h_{\mathrm{i}}}} \\ F_{\mathrm{n}}^{\mathrm{L}} &= \frac{v_{\mathrm{x}}}{\sqrt{g L_{\mathrm{wl}}}} \end{aligned} \tag{26}$$

Typically, empirical formulae based on regression and dimensional analyses indicate linear dependence of mean ice resistance on ship speeds.

The numerical results showing relations between ship speed and mean resisting force and moment from ice in surge and pitch directions at steady speed are presented in Fig. 12. Regarding the numerical results obtained by the dynamic bending model, the mean values of resisting forces and moments increase linearly with ship speed, which agrees with the trend predicted by most ice resistance formulae. The values for surge ice resistance (Fig. 12(a)) calculated by Lindqvist's are however lower than that given by the dynamic bending model especially for thick ice. For the static bending model, the main ice resisting force component that is speed dependent is the ice floe clearing and submersion force. It is noticed in Fig. 12(a) that in very thick ice (e.g., 1.1m), where the icebreaking component has became dominant over the clearing and

485 submersion component, resistance given by the static bending model does not seem to
486 show much sensitivity to ship speeds. In thin ice, however, the total ice resistance
487 from the static bending model is influenced more by the ice clearing and submersion
488 component and thus shows a linear dependence on ship speeds as depicted in Fig.
489 12(a).

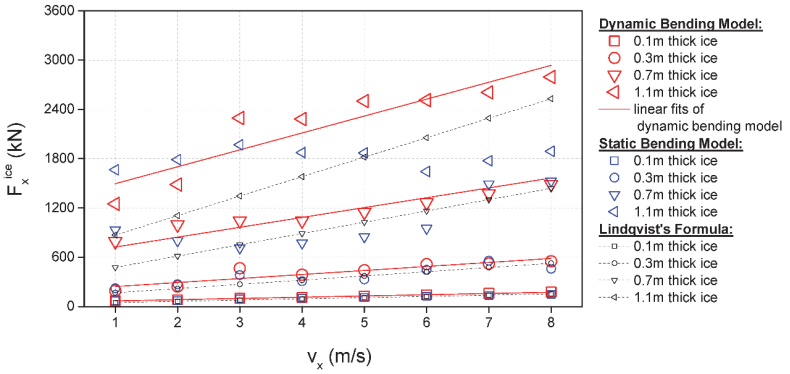

490
491 (a). Mean surge ice resistance vs. ship speed

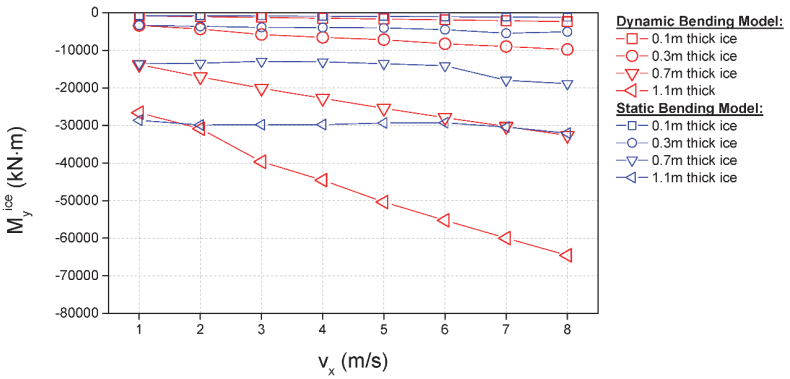

492
493 (b). Mean pitch moment vs. ship speed

494 Fig. 12. Simulated mean values of ice resistance vs. ship speed

495 Comparison between numerical results from the dynamic and the static bending
496 models shows that for a certain ice thickness, the ice resisting force and moment given
497 by the static bending model is slightly higher than that given by the dynamic bending
498 model at very low speed (1.0m/s). The reason is explained in Section 3.2. In the high

speed range, the situation is reversed due to the same reason. As shown in Fig. 8, the bending failure load given by the dynamic bending model increases with colliding speeds which are associated with the ship's forward speed, whereas in the static bending model, it is independent of ship speeds.

Fig. 13 shows the dependence of surge ice resistance on ice thickness with the lowest and the highest speeds that are covered in this paper. The fitted curves of numerically predicted data as well as Lindqvist's calculations show a power relation between mean values of surge ice resistance and ice thicknesses:

$$F_{\mathrm{x}}^{\mathrm{ice}} = a h_{\mathrm{i}}^{\mathrm{b}} \tag{27}$$

Both Lindqvist's calculation and the numerical predictions indicate that the coefficient a increases with ship speeds, which is a trend also observed in the model tests conducted by Ettema et al. (1987). The values of a given by Lindqvist are lower than the ones given by the dynamic bending model, which is the main cause for a lower resistance as seen in Fig. 12(a). The smaller sensitivity to ship speeds of the static bending model is reflected in Fig. 13 too. The exponent b for the dynamic bending model is in the range of 1.2 ~ 1.4 for the speed range covered; Lindqvist's gives values of b between 1.2 ~ 1.3, and it is 1.9 ~ 2.1 given by Ettema et al. (1987).

Although Eq. (25) is somewhat simplified and empirically based especially with respect to hull geometry and contact mechanism, it is however illustrative and helpful when trying to understand the relations between ice thickness, ship speed and ice resistance. The resistance components given by Lindqvist in Eq. (25) can be expressed concisely as:

$$F_c = c_h h_i^2$$
$$F_b = b_h h_i^{1.5} \quad (28)$$
$$F_s = s_h h_i$$

where c_h, b_h and s_h are coefficients associated with hull geometry, ice flexural strength and friction, i.e., independent of ice thickness and ship speeds. By inserting Eq. (26) and Eq. (28), Eq. (25) can be rewritten as:

$$F_x^{ice} = c_h h_i^2 + (b_h + \frac{1.4 c_h}{\sqrt{g}} v_x) h_i^{1.5} + (s_h + (\frac{1.4 b_h}{\sqrt{g}} + \frac{9.4 s_h}{\sqrt{g L_{wl}}}) v_x) h_i \quad (29)$$

Eq. (29) reveals that in addition to the dependence on h_i^2, other lower-order terms may exist. Moreover, v_x and h_i may be entangled with each other. This explains why the coefficient a increases with v_x, which is observed in three different studies. The overall power dependence, i.e., the b value, is determined by parameters in Eq. (29), on which ship speeds has an influence too.

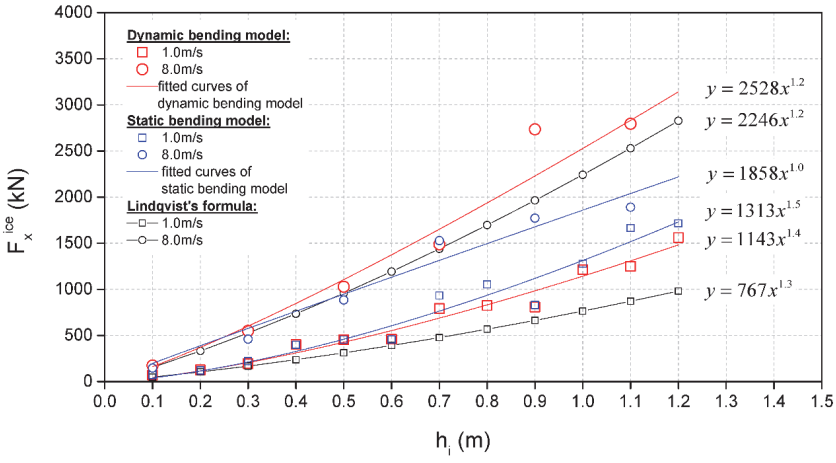

Fig. 13. Simulated mean surge ice resistance vs. ice thickness

3.4 Ship Motions

The simulated mean values of heave, roll and pitch are presented in Fig. 14. Similar to the characters of forces and moments, the motions given by the static bending model are not as sensitive to ship speeds as those given by the dynamic bending model.

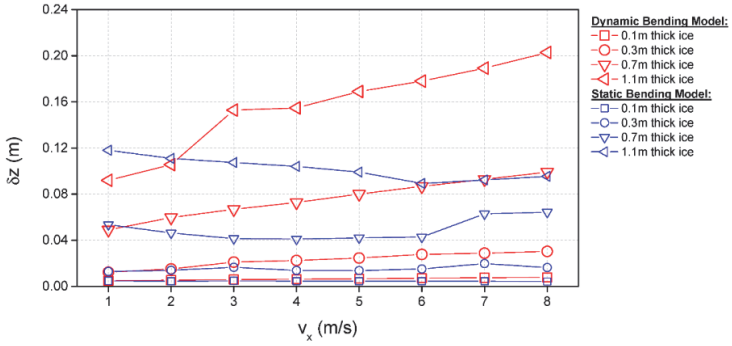

(a) Mean heave vs. ship speed

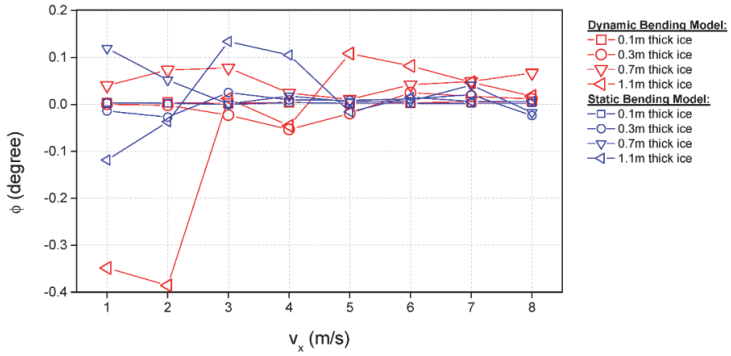

(b) Mean roll vs. ship speed

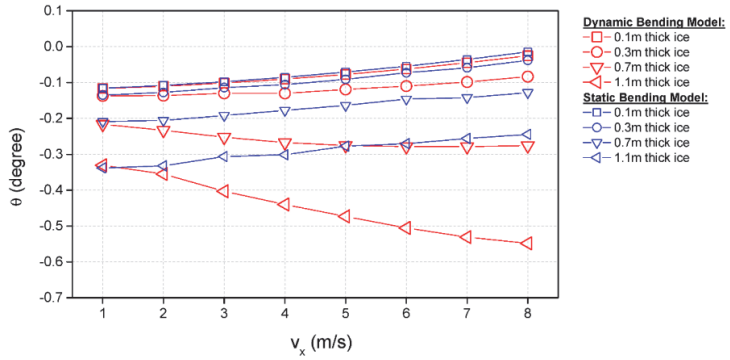

(c) Mean pitch vs. ship speed

Fig. 14. Simulated mean values of motions vs. ship speed

544 Fig. 14(b) indicates that roll is not influenced by ship speeds. However, several major
545 jumps of roll angle are spotted in thick ice for both the static and the dynamic bending
546 models. The ice loads around the bow is not laterally symmetric especially for thick
547 ice where icebreaking radii (floe sizes) are larger and thus the ship is loaded more
548 non-uniformly. Transverse responses may under some circumstances be significant in
549 determining the icebreaking pattern and the ice resistance. Large amplitudes of roll
550 and correspondingly high values of ice resistance have also been reported in the
551 model tests conducted by Ettema et al. (1987).

552 The pitch angles given by the static bending model decrease linearly with ship speeds
553 for all ice thicknesses calculated. For the dynamic bending model, however, the pitch
554 angles decrease with ship speeds for thin ice while increase with ship speeds for thick
555 ice (Fig. 14(c)). It is interesting to note that in medium thick ice for the dynamic
556 bending model (e.g., 0.5m and 0.7m), an increase in low speed range is followed by a
557 decrease with speeds in high speed range. The natural frequency of pitch for Tor
558 Viking II is estimated to be 0.15Hz. Spectral analysis on the time histories of pitch
559 moment at 1.0m/s ship speed (i.e., the lowest speed) gives the frequency values of
560 1.31Hz and 0.20Hz in 0.1m and 1.1m ice, respectively. As the ship speed increases,
561 the frequency of pitch moment increases and thus goes further away from the natural
562 frequency of pitch. This leads to a general decrease of pitch as shown by results given
563 by the static bending model. For the dynamic bending model, however, the magnitude
564 of pitch moment in thick ice increases dramatically as compared to that in thin ice as
565 well as to the case in the static model. Therefore, the value of pitch angle is influenced
566 by the magnitude of pitch moment and its frequency. A similar trend for the mean
567 values of pitch and heave variations with ship speeds is reported in the model tests by
568 Ettema et al. (1987), as is shown in Fig. 15.

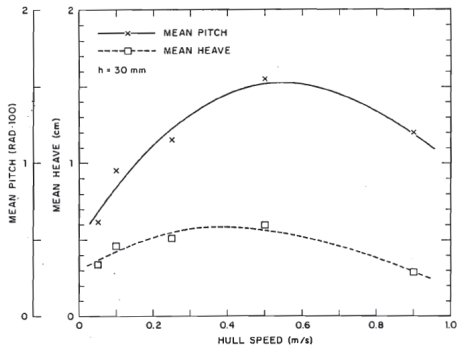

Fig. 15. Mean pitch and heave vs. ship speed from a model test with an USCGC Polar-Class Icebreaker (Ettema et al., 1987)

3.5 Spatial Distribution of Icebreaking Forces

The spatial distributions of the icebreaking forces with various ice thicknesses and ship speeds are inspected. The ship's waterline is discretized into 50 nodes and segments. The time histories of the normal icebreaking loads on each of the hull segments are recorded, and examples of typical load histories for different hull areas are shown in Fig. 16Fig. 17.

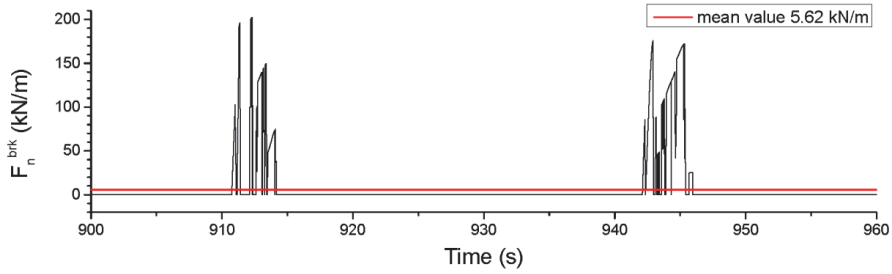

(a) Normal icebreaking force on segment #9 – #10 (side hull)

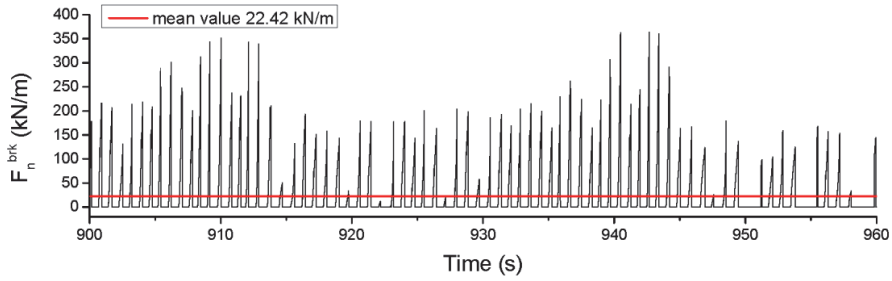

(b) Normal icebreaking force on segment #21 – #22 (bow shoulder)

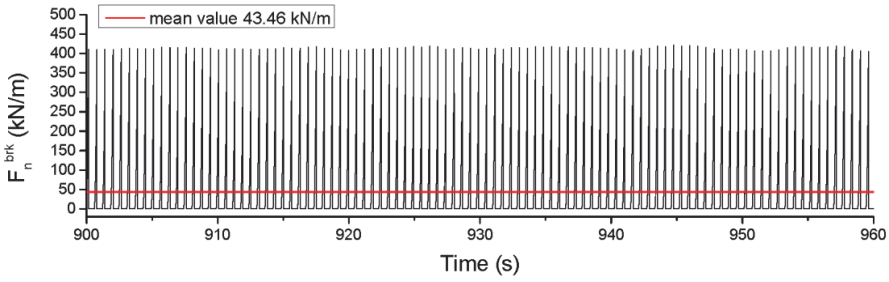

582

583 (c) Normal icebreaking force on segment #26 – #27 (bow)

584 Fig. 16 Examples of time histories of local icebreaking forces ($h_i = 0.7$m, $v_x = 5$m/s)

585 The mean values of the icebreaking forces on each of the segments are calculated and

586 plotted in Fig. 17.

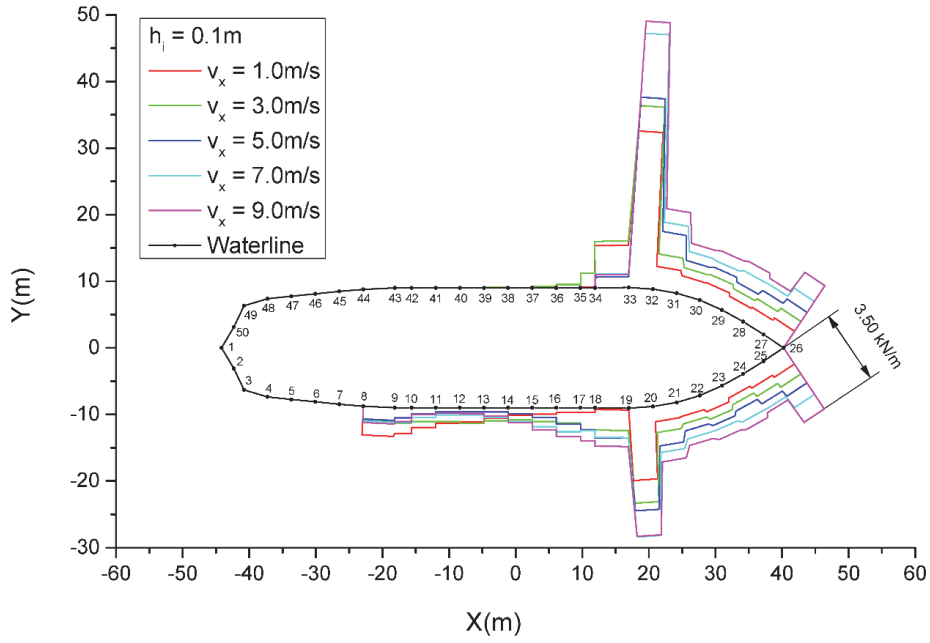

587

588 (a)

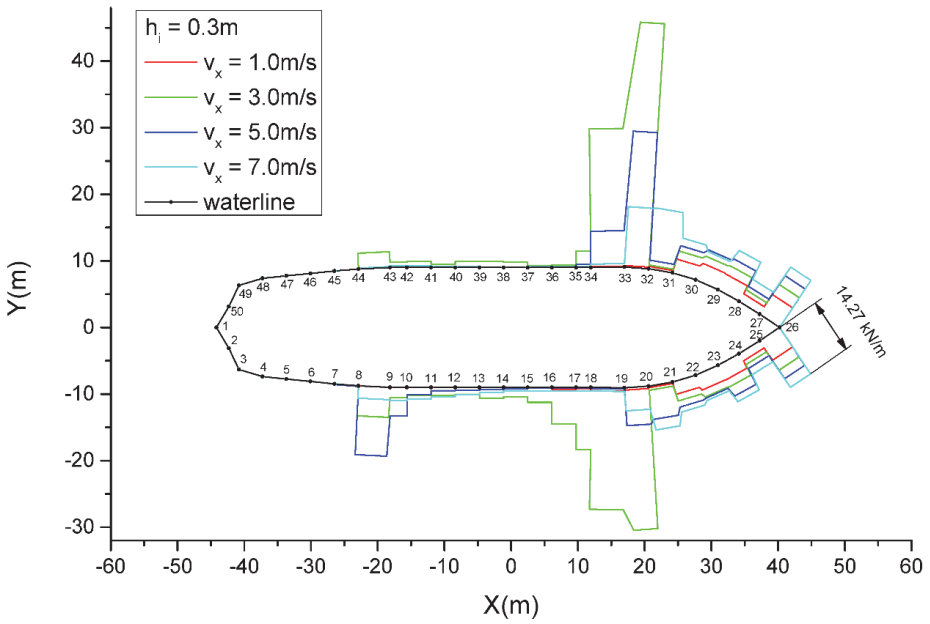

589

590 (b)

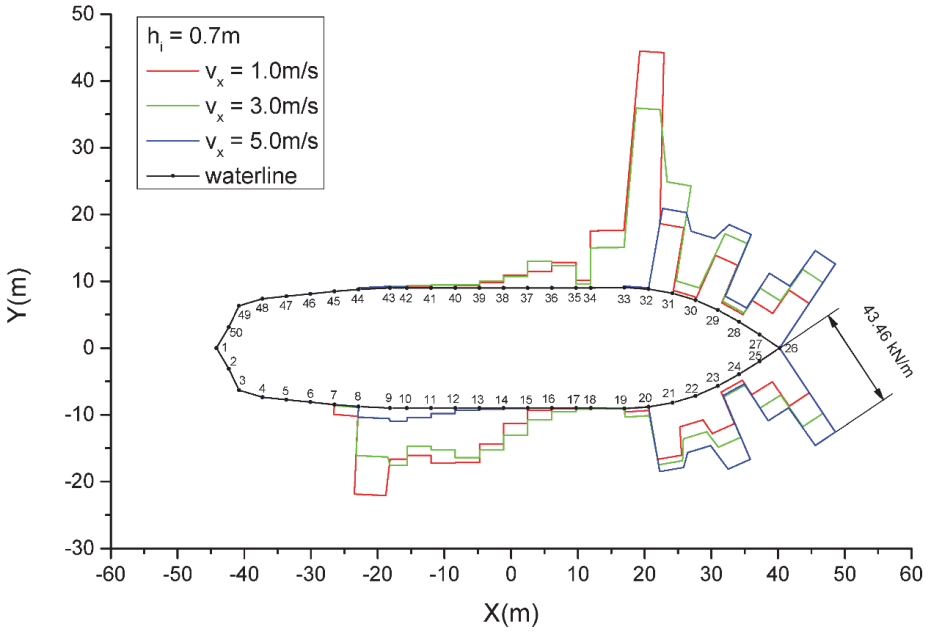

591

592 (c)

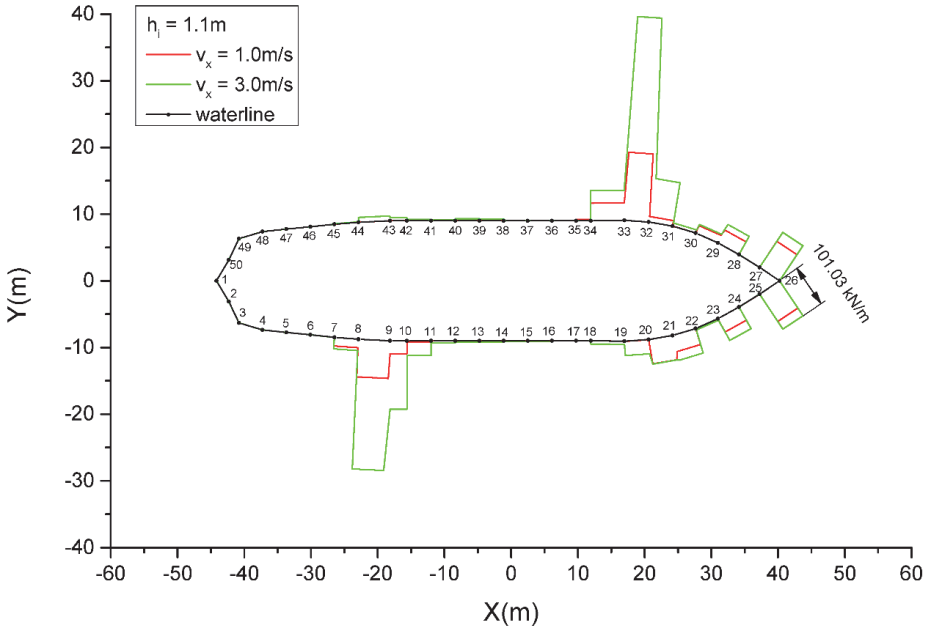

(d)

Fig. 17 Spatial distribution of the mean normal ice force on the hull (the magnitudes are represented by the "heights" of the "load rectangles" associated with each segment)

The forces on the bow area, especially on the segments between nodes #25, #26 and #26, #27, show a distinct dependence on ship speeds. For the shoulder and the side hull areas, however, the distribution is more irregular as compared to the bow area due to the drastically increased frame angles. Additionally, since at the bow shoulder and the side hull areas the ship hull is sliding along the ice edge rather than indenting directly into it, the normal relative speed is much smaller than that for the bow area. Ice is more often crushed than bent. This makes the frictional force the major contribution to the hull loading. When the channel opened by the bow is not sufficiently wide to avoid constant contact between the hull and the ice edge, crushing may be significant, as in the case of 0.3m–3.0m/s, 0.7m–1.0m/s & 3.0m/s and 1.1m–3.0m/s. These cases correspond to the high resistance points in Fig. 12(a). Thus, the inspection of spatial distributions of ice forces explains how, in some cases, despite

610 the relatively small ice thickness and low ship speed, the total ice resistance is much
611 higher than expected, and how the occurrence of shoulder crushing could increase the
612 total ice resistance by increasing the local ice loads.

613 **4. Conclusions**

614 The dynamic bending effect of the ice edge is investigated and implemented into a
615 numerical procedure simulating the interaction between level ice and ships. The *h–v*
616 curve reflecting ship performance is calculated and compared with full-scale data.
617 Based on the mechanism of dynamically bent ice edge, the relations between ice
618 resistance, ship motions and ship speeds are examined. Conclusions are listed as
619 follows:

620 1) The bending failure load of a wedge shaped ice edge is dependent on loading rates,
621 which is associated with ship's forward speed, via power relation as given by Fig. 8
622 and Eq. (21).

623 2) The *h–v* curve given by the dynamic bending model correlates better to full-scale
624 ice trial than does the one derived by the static bending model due to the ability of the
625 dynamic bending model to dynamically modulate the local failure load of the ice edge.

626 3) The ice resistance and pitch moment given by the dynamic bending model increase
627 linearly with ship's forward speed.

628 4) Roll motion could under certain conditions bring about extra resistance in ice,
629 especially when the bow does not open a channel sufficiently wide to let the
630 maximum beam transit through.

631 5) An inspection of the spatial distribution of the icebreaking resistance reveals that
632 for some cases the shoulder areas experience much higher ice loads locally than other

633 area of the hull. The occurrence of shoulder crushing is determined by the icebreaking
634 pattern which assumes ice bending in a predefined manner in the numerical model;
635 the icebreaking pattern inherently involves the major assumptions in the analytical
636 treatment of the problem. A further study on the correlation between the mathematical
637 model of the icebreaking pattern and the channel width and ship motions needs to be
638 carried out.

639 6) Pitch angles given by the dynamic bending model decrease with ship speeds for
640 thin ice while increase with ship speeds for thick. In medium ice thicknesses (e.g.,
641 0.7m), pitch angle increases more rapidly in low speed range (1m/s~3m/s) than in
642 high speed range. This is a result of both the magnitude and frequency of pitch
643 moment.

644 (7) The speed dependence of the ice wedge failure load proposed in this paper is
645 based on limited information and idealized conditions. For example, the speed
646 dependent term, λ_t, is derived under a certain ice thickness (0.35m), flexural failure
647 strength (1.2MPa) and wedge opening angle (90°). By assuming that the failure load
648 is proportional to the square of ice thickness and that it is linearly proportional to the
649 flexural strength of ice, the limited information given by Varsta's tests are
650 extrapolated to be used for different thickness and strength conditions. Although the
651 assumed proportional relationships are consistent with former works conducted by
652 various researchers, its adequacy to describe the picture for other ice thicknesses and
653 flexural strengths needs to be verified in future works. The influence of the geometry
654 of the ice wedge also needs to be investigated. For this purpose, more extensive
655 investigations, both theoretically and experimentally, on the problem of ice–water–
656 ship interaction are expected.

657 **Acknowledgement**

658 The authors would like to acknowledge TOTAL E&P NORGE AS for funding of the
659 research. The support of the Research Council of Norway through the Centre for
660 Ships and Ocean Structures in the Norwegian University of Science and Technology
661 is also acknowledged.

662 **References**

663 Aksnes, V., 2010. A simplified interaction model for moored ships in level ice. Cold
664 Regions Science and Technology, Vol. 63, pp. 29–39.

665 Daley, C., 1991. Ice edge contact – A brittle failure process model. Ph.D. Thesis,
666 Laboratory of Naval Architecture and Marine Engineering, Helsinki University of
667 Technology, Espoo, Finland.

668 Dempsey, J. P., Fox, C., and Palmer, A. C., 1999. Ice-Slope interaction: Transitions in
669 failure mode. Proc. 18th International Conference on Offshore Mechanics and Arctic
670 Engineering (OMAE), St John's, Newfoundland, Canada.

671 Dempsey, J.P., Zhao, Z., 1993. Elastohydrodynamic response of an ice sheet to forced
672 sub-surface uplift. Journal of the Mechanics and Physics of Solids. Vol. 41, pp487-
673 506.

674 Enkvist, E., 1972. On the ice resistance encountered by ships operating in the
675 continuous mode of icebreaking. Report No. 24. The Swedish Academy of
676 Engineering Science in Finland.

677 Enkvist, E., Varsta, P., Riska, K., 1979. The ship-ice interaction. Proc. 5th
678 International Conference on Port and Ocean Engineering under Arctic Conditions
679 (POAC), Trondheim, Norway. pp. 977–1002.

680 Ettema, R., Stern, F. and Lazaro, J., 1987. Dynamics of continuous-mode icebreaking
681 by a Polar-class icebreaker hull. IIHR report No. 314.

682 Ettema, R., Sharifi, M.B., Georgakakos, K.P. and Stern, F., 1991. Chaos in
683 continuous-mode icebreaking. Cold Regions Science and Technology, Vol. 19, pp.
684 131–144.

685 Fox, C., 1993. The Response of a Floating Ice-sheet to Rapid Edge Loading. Ice
686 Mechanics. ASME AMD. Vol. 163, pp. 145-150.

687 Fox, C., Squire, V., 1994. On the oblique reflexion and transmission of ocean waves
688 at shore fast sea ice. Philosophical Transactions: Physical Sciences and Engineering.
689 Vol. 347, No. 1682.

690 Fox, C., 2001. A scaling law for the flexural motion of floating ice. Solid mechanics
691 and its applications. Vol. 94, pp 135-148.

692 Fox, C. and Chung, H., 2002. Harmonic deflections of an infinite floating plate. Vol.
693 485 of Report series. Department of Mathematics, School of Mathematical and
694 Information Sciences, University of Auckland.

695 Izumiyama, K., Kitagawa, H., Koyama, K. and Uto, S., 1991. On the interaction
696 between a conical structure and ice sheet, Proc. 11st International Conference on Port
697 and Ocean Engineering under Arctic Conditions (POAC), St. John's, Canada. pp155-
698 166.

699 Kashteljan, V.I., Poznjak, I.I. and Ryvlin, A.J., 1968. Ice resistance to motion of a
700 ship. Marine Computer Application Corporation， Sudostroyeniye, Leningrad, Russia.

701 Kerr, A. D., 1975. The Bearing Capacity of Floating Ice Plates Subjected to Static or
702 Quasi-Static Loads-A Critical Survey. Corps of Engineers, U.S. Army, Cold Regions
703 Research and Engineering Laboratory, 1975, 43pp.

704 Kotras, T.V., Baird, A.V., and Naegle, J.W., 1983. Predicting ship performance in
705 level ice. Transactions of Society of Naval Architects and Marine Engineers
706 (SNAME), Vol. 91, pp. 329–349.

707 Langen, I. and Sigbjornsson, R., 1977. Dynamic analysis of structures, Tapir,
708 Trondheim, Norway, 505 pp.

709 Lau, M. and Williams, F., 1991. Model ice forces on a downward breaking cone. the
710 eleventh international conference on Port and Ocean Engineering under Arctic
711 Conditions (POAC), St,. John's, Canada.

712 Lewis, J.W. and Edwards R.Y., 1970. Methods for predicting icebreaking and ice
713 resistance characteristics of icebreakers. Transactions of Society of Naval Architects
714 and Marine Engineers (SNAME), Vol. 78, pp. 213-249.

715 Lewis, J.W., DeBord, F.W. and Bulat, V.A., 1982. Resistance and propulsion of ice-
716 worthy ships. Transactions of Society of Naval Architects and Marine Engineers
717 (SNAME), No. 8.

718 Lindqvist, G., 1989. A straightforward method for calculation of ice resistance of
719 ships. Proc. 10th International Conference on Port and Ocean Engineering under
720 Arctic Conditions (POAC), Luleå, Sweden. pp. 722–735.

721 Liu, J., 2009. Mathematical modeling ice–hull interaction for real time simulations of
722 ship manoeuvring in level ice. Ph.D. Thesis, Faculty of Engineering and Applied
723 Science, Memorial University of Newfoundland, St. John's, Newfoundland, Canada.

724 Lu, W., Løset, S. and Lubbad, R., 2012. Ventilation and backfill effect during ice–
725 sloping structure interactions. Proc. 21st International Symposium on Ice (IAHR),
726 Dalian, China. pp. 826–841.

727 Lubbad, R., Geir, M., Løset, S., 2008. Static and dynamic interaction of floating
728 wedge-shaped ice beams and sloping structures. Proc. 19th International Symposium
729 on Ice (IAHR), Vancouver, British Columbia, Canada.

730 Lubbad, R. and Løset, S., 2011. A numerical model for real-time simulation of ship–
731 ice interaction. Cold Regions Science and Technology, Vol. 65, pp. 117–127.

732 Milano, V., 1973. Ship resistance to continuous motion in ice. Transactions of Society
733 of Naval Architects and Marine Engineers (SNAME), No. 9.

734 Nevel, D. E., 1958. The narrow infinite wedge on elastic foundation. Transactions of
735 the Engineering Institute of Canada, Vol.2, No.3, pp. 132-140.

736 Nguyen, D. T., Sørbø, A. H. and Sørensen, A. J., 2009. Modelling and control for
737 dynamic positioned vessels in level ice. Proc. 8th International Conference on
738 Maneuvering and Control of Marine Craft (IFAC). Casa Grande Hotel, Brazil. pp.
739 229-236.

740 Riska, K., 1980. On the role of failure criterion of ice in determining ice loads.
741 Technical Research Centre of Finland (VTT), Ship Laboratory, Helsinki University of
742 Technology, Espoo, Finland. Report 7, 31p.

743 Riska, K., 1987. On the mechanics of the ramming interaction between a ship and a
744 massive ice floe. Ph.D. Thesis, Helsinki University of Technology, Espoo, Finland.

745 Riska, K., 1995. Models of ice-structure contact for engineering applications,
746 Mechanics of Geomaterial Interfaces, Vol. 42, pp. 77-103.

747 Sørensen, C., 1977. Dynamic Bending Failure of a Semi-Infinite Ice Floe Hitting a
748 Sloping Plane. Proc. 4th International Conference on Port and Ocean Engineering
749 under Arctic Conditions (POAC), Newfoundland, Memorial University, Canada, Vol.
750 1, pp. 580-592.

751 Su, B., Riska, K. and Moan, T., 2010a. A numerical method for the prediction of ship
752 performance in level ice. Cold Regions Science and Technology. Vol. 60, pp. 177-188.

753 Su, B., Riska, K. and Moan, T., 2010b. Numerical simulation of ship turning in level
754 ice. Proc. 29th International Conference on Offshore Mechanics and Arctic
755 Engineering (OMAE), Shanghai, China.

Su, B., 2011. Numerical predictions of global and local ice loads on ships, Ph.D. Thesis, Department of Marine Technology, NTNU, Trondheim, Norway.

Tan, X., Su, B., Riska, K. and Moan, T., 2012. The Effect of Heave, Pitch and Roll Motions to Ice Performance of Ships. Proc. 21st International Symposium on Ice (IAHR), Dalian, China. pp. 1080-1093.

Tan, X., Su, B., Riska, K. and Moan, T., 2013. A six-degrees-of-freedom numerical model for level ice–ship interaction. Cold Regions Science and Technology. Vol. 92, pp. 1-16.

Tuhkuri, J., 1996. Experimental investigations and computational fracture mechanics modelling of brittle ice fragmentation. Ph.D. Thesis, Helsinki University of Science and Technology, Espoo, Finland.

Valanto, P., 1989. Experimental study of the icebreaking cycle in 2-D. Proc. 8th International Conference on Offshore Mechanics and Arctic Engineering (OMAE), The Hague, Netherlands. pp. 343-349.

Valanto, P., 1992. The icebreaking problem in two dimensions: experiments and theory. Journal of Ship Research. Vol. 36. pp. 299-316.

Valanto, P., 1993. Investigation of the icebreaking pattern at the bow of the IB kapitan Sorokin on the Yenisei River Estuary in May 1991. Proceedings of 12th International Conference on Offshore Mechanics and Arctic Engineering (OMAE), pp. 127–134.

Varsta, P., 1983. On the mechanics of ice load on ships in level ice in the Baltic Sea. Ph.D. Thesis, Helsinki University of Technology, Espoo, Finland.

Wang, S., 2001. A dynamic model for breaking pattern of level ice by conical structures, Ph.D. Thesis, Department of Mechanical Engineering, Helsinki University of Technology, Espoo, Finland.

Paper 3

Performance simulation of a dual-direction ship in level ice

Xiang Tan, Kaj Riska and Torgeir Moan

Under Review in the *Journal of Ship Research*

Performance simulation of a dual-direction ship in level ice

Xiang Tan[1,2*], Kaj Riska[1, 3] and Torgeir Moan[1, 2]

1. Centre for Ships and Ocean Structures
Norwegian University of Science and Technology
N-7491, Trondheim, Norway
2. Department of Marine Technology
Norwegian University of Science and Technology
N-7491, Trondheim, Norway
3. TOTAL S.A. - DGEP/DEV/ED/EC
92400 Paris La Défense – France
* tan.xiang@ntnu.no

Abstract

The ice performance of a dual-direction ship is investigated through a numerical procedure developed to simulate the continuous-mode icebreaking in level ice. The effect of propeller–hull–ice interaction for running astern is included by applying the knowledge obtained from model tests to the numerical procedure. The numerical procedure is in turn used as a performance prediction tool to supplement the model test data to investigate the thrust deduction in ice.

Keywords: numerical model, dual-direction ships, propeller–hull–ice interaction, thrust deduction in ice

1. Introduction

1.1 Dual-Direction Ship Concept

The experience with the “bow propellers” for icebreaking dates back to late 1800s, when captains operating ships in ice bound waters discovered that sometimes it was easier to break through ice by running their vessels astern (Juurmaa et al., 1995). These findings then resulted in the adoption of bow propellers in older icebreakers operating in the Great Lakes and the Baltic Sea (see e.g. Jansson, 1956a; Jansson, 1956b; Jones, 2004). However, the steering ability of a ship with traditional shaftline propeller–rudder system is greatly reduced when running astern. Moreover, forward-facing propellers have very low propulsion efficiency and they considerably increase the ship's open water resistance. These shortcomings of conventional propulsion systems made running astern not a main operation mode at that time.

The dual-direction concept advantage was not fully unleashed until the application of electric podded propulsion units (e.g. Fig. 1) to ice-capable ships. Such propulsions systems combine the advantages of diesel-electric powertrain with azimuthing

thrusters, offering enhanced propulsion efficiency, great maneuverability and better hull space usage.

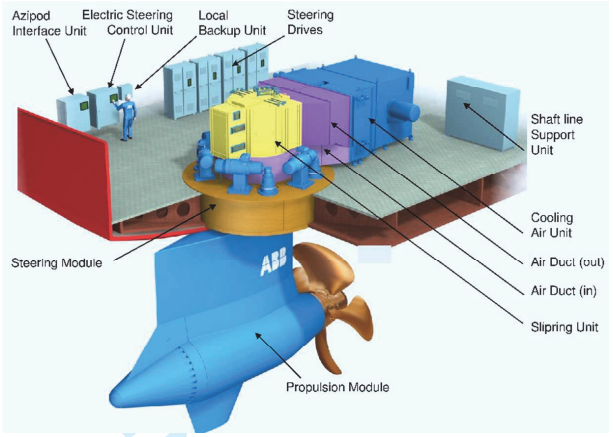

Fig. 1 The Azipod® XO system (source: www.abb.com)

The basic idea is that the ship runs in bow first mode in open water and light ice conditions; in heavy ice it runs in stern first mode. When running ahead, with the bow designed for open water operations, the ship achieves better performance in open water than it does when being installed with icebreaking bows. When heavy ice conditions are encountered, the ship turns around and attacks the ice with the stern designed for icebreaking. More importantly, when running astern with propeller first, the flushing effect the propeller brings about lowers the ice resistance by flushing the ice floes backwards and decreasing the water pressure under the ice cover (Vocke et al., 2011). As a result, the icebreaking performance in heavy ice conditions when running astern is better even if the open water resistance in this mode is higher. Thus, a better overall performance and economic effect may be achieved considering the relatively long open water voyage along the Arctic sea routes.

1.2 Theory of Dual-Direction Ships

1.2.1 Thrust Deduction in Open Water

It has been observed in open water tests that the thrust force of a ship at self-propulsion point, i.e., free running at the maximum speed attainable without external towing force, exceeds the towing force measured when the ship is towed at the same speed. The propeller therefore alters the hull resistance by an amount, for which the force equilibrium equation can be expressed as:

$$T_{\mathrm{T}} = R_{\mathrm{ow}}^{[\mathrm{h}]} + \Delta R_{\mathrm{ow}} \tag{1}$$

where T_T denotes the total thrust, i.e., the thrust measured on propeller shaft; R_{ow} is open water resistance, the superscript [h] indicates the resistance of bare hull (towed resistance); ΔR_{ow} is hull resistance augmentation caused by the interaction between the hull and propeller flow.

The physical origin of ΔR_{ow} lies in the fact that propeller accelerates flow in front and behind of it resulting in an increased rate of shear in boundary layer (meaning an increased frictional resistance on propeller blades) as well as an increased pressure over the rear of the hull (meaning an increased pressure resistance on the hull). In practice, this is viewed as a thrust deduction:

$$T_T \cdot (1 - t_{ow}) = R_{ow}^{[h]} \tag{2}$$

ΔR_{ow} is usually expressed as a fraction of the total thrust by a thrust deduction factor defined as:

$$t_{ow} = \frac{\Delta R_{ow}}{T_T} \tag{3}$$

Generally, the value of t_{ow} in the ahead mode (approximately 0.03) is much smaller than that in the astern mode (approximately 0.2) due to the different hull shapes in the bow and stern areas.

1.2.2 Thrust Deduction in Ice

Similar to the open water case, in ice covered waters, the force equilibrium equation for a ship breaking ice can be expressed as:

$$T_T = \underbrace{R_I^{[h]} + R_{ow}^{[h]}}_{R_T^{[h]}} + \Delta R_T \tag{4}$$

where $R_I^{[h]}$ is bare hull ice resistance; $R_T^{[h]}$ is the bare hull total resistance; ΔR_T is the hull resistance augmentation caused by the interaction between the ship hull, propeller flow and the ice.

Unlike the added resistance in open water, ΔR_T is often observed to be negative when the ship is running propeller first. In fact, when the ship is running propeller first in ice covered waters, the propeller on the one hand causes an increase in hull resistance (a positive ΔR_{ow}) due to the interaction between the stern and the propeller flow; on the other hand, the broken ice floes attached to the bottom of the hull would be flushed backwards (towards the bow) by the flow generated by propeller which causes a decrease (denoted as ΔR_I) in the hull resistance component associated with carrying the broken ice floes. The experiences with icebreaking when running astern suggest

that often the overall effect of propeller is to reduce the total hull resistance even if the open water thrust deduction is higher than when running ahead, implying a larger effect of ΔR_I which overrides the effect of ΔR_{ow}.

Since the added resistances, ΔR_{ow} and ΔR_I, originate from different regions of hull due to different physical backgrounds, it is assumed that ΔR_T is a superposition of ΔR_{ow} and ΔR_I:

$$\Delta R_T = \Delta R_I + \Delta R_{ow} \tag{5}$$

Thus, Eq. (4) becomes:

$$T_T = R_I^{[h]} + \Delta R_I + R_{ow}^{[h]} + \Delta R_{ow} \tag{6}$$

By introducing the concept of net thrust in ice, T_{net}:

$$T_{net} = T_T \cdot (1 - t_{ow}) - R_{ow}^{[h]} \tag{7}$$

Eq. (6) could be expressed alternatively as:

$$T_{net} = R_I^{[h]} + \Delta R_I \tag{8}$$

The thrust deduction factor in ice in this paper is defined as:

$$t_I = \frac{\Delta R_I}{T_T} \tag{9}$$

Thus,

$$T_T \cdot (1 - t_{ow} - t_I) = R_{ow}^{[h]} + R_I^{[h]} \tag{10}$$

Besides, an overall thrust deduction factor could be defined as:

$$t_{TOT} = \frac{\Delta R_T}{T_T} \tag{11}$$

Thus,

$$T_T \cdot (1 - t_{TOT}) = R_{ow}^{[h]} + R_I^{[h]} \tag{12}$$

1.2.3 Knowledge from Model Tests

A series of model tests were conducted by Leiviskä (2004) to clarify the issue of propeller–hull–ice interaction with the model of M/T Uikku. Several distinct types of tests were performed.

Propeller open water tests were used to measure the propeller characteristics including the thrust and torque coefficients, denoted as K_T and K_Q respectively:

$$K_T = \frac{T}{\rho n^2 D_p^4} \tag{13}$$

$$K_Q = \frac{Q}{\rho n^2 D_p^5} \tag{14}$$

where T and Q denote thrust and torque respectively; ρ is water density; n is propeller shaft speed and D_p is propeller diameter.

The propulsion power delivered is described by the measured n and Q as:

$$P_D = 2\pi n Q \tag{15}$$

Open water overload tests were conducted over a wide range of shaft speeds and ship speeds to obtain the thrust deduction factor in open water (t_{ow}) which is usually described as a function of the advance ratio, J:

$$J = \frac{V_A}{nD_p} \tag{16}$$

where V_A is the advance speed of the propeller.

The test results and regression curves of open water thrust deduction factors, t_{ow}, for ahead and astern modes are plotted in Fig. 2 and Fig. 3, respectively.

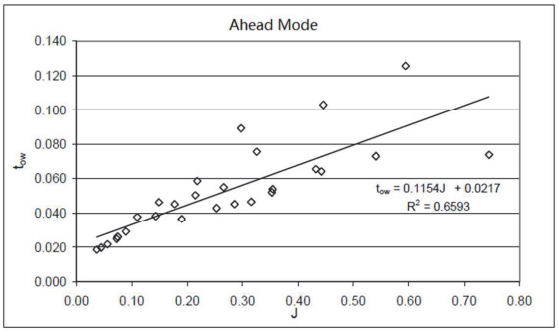

Fig. 2 Open water thrust deduction factor for ahead mode (Leiviskä, 2004)

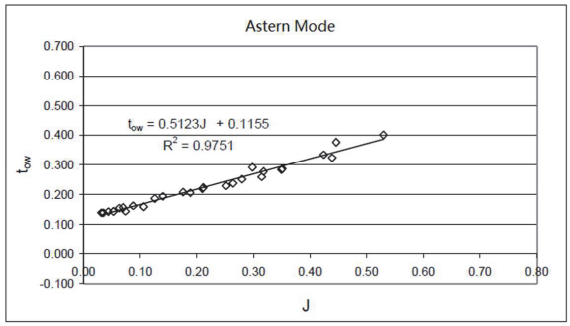

Fig. 3 Open water thrust deduction factor for astern mode (Leiviskä, 2004)

In addition to the model tests mentioned above, self-propelled as well as corresponding towed tests in open water, level ice and brash ice were conducted for the purpose of determining the resistances under different conditions. These tests provide an insight into the physical nature of the pheromone of bow propellers.

Especially, model tests in level ice were conducted under towed as well as self-propulsion conditions in astern mode to investigate the influence of propeller flow on the broken ice resistance component. In the towed tests, the bare hull resistance, $R_T^{[h]}$, was measured at the same speed as in the self-propulsion condition. The level ice model tests were conducted in two ice thicknesses, 18mm and 29mm. For each of the ice thicknesses, four tests were carried out with different power outputs which enclose the installed propulsion power of the full-scale ship. Since the test results provided by Leiviskä (2004) are somewhat raw, the authors extend the results for further use in the present paper. The added resistances caused by the flushing effect of propeller flow in level ice in astern mode are calculated and listed in Table 1 and Table 2 based on the measured quantities.

Table 1 Hull resistance augmentation in 18mm level ice, astern mode*

v [m/s]	P_D [W] Eq.(15)	T_T [N]	$R_T^{[h]}$ [N]	$R_{ow}^{[h]}$ [N]	$R_I^{[h]}$ [N] Eq.(17)	t_{ow} Fig. 3	ΔR_{ow} [N] Eq. (3)	ΔR_T [N] Eq. (4)	ΔR_I [N] Eq. (5)
0.36	27.6	12.6	18.2	2.0	16.2	0.219	2.8	-5.6	-8.4
0.55	60.6	19.9	25.8	4.4	21.4	0.241	4.8	-5.9	-10.7
0.74	95.1	29.9	35.7	8.0	27.7	0.257	7.7	-5.8	-13.5
0.91	146.7	41.0	45.2	11.6	33.6	0.264	10.8	-4.2	-15.0

Table 2 Hull resistance augmentation in 29mm level ice, astern mode*

v [m/s]	P_D [W] Eq.(15)	T_T [N]	$R_T^{[h]}$ [N]	$R_{ow}^{[h]}$ [N]	$R_I^{[h]}$ [N] Eq.(17)	t_{ow} Fig. 3	ΔR_{ow} [N] Eq. (3)	ΔR_T [N] Eq. (4)	ΔR_I [N] Eq. (5)
0.26	57.9	19.6	23.0	1.1	21.9	0.179	3.5	-3.4	-6.9
0.38	66.8	22.6	29.2	2.2	27.0	0.203	4.6	-6.6	-11.2
0.53	119.4	32.0	37.5	4.1	33.4	0.217	6.9	-5.5	-12.4
0.73	181.4	42.3	49.6	7.6	42.0	0.235	9.9	-7.3	-17.2

* The originally recorded quantities in the model tests given directly by Leiviskä (2004) are: v, T_T, $R_T^{[h]}$, $R_{ow}^{[h]}$ and t_{ow}, which are highlighted in yellow. The rest quantities in the tables are calculated by the authors based on the measurements and equations introduced in this paper.

The relations between the added resistance obtained from Table 1 and Table 2 and ship speed are plotted in Fig. 4.

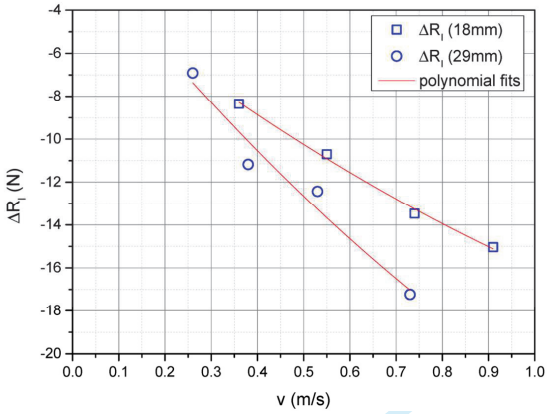

Fig. 4 Hull resistance augmentation in astern mode

The negative ΔR_T and ΔR_I calculated in Table 1 and Table 2 indicates that when the ship is running astern in level ice, the propeller has such an effect as lowering the total hull resistance. The reason is that the propeller flow flushes some of the broken ice floes away, which would otherwise be attached to, or sliding along, the bottom of the hull, and thus decreases the area of the hull covered by the broken ice pieces. As a result, the broke ice resistance component is lowered.

The maximum ship speeds at the full installed power (P_D in Table 4) in each of the ice thicknesses are calculated and listed in Table 3.

Table 3 Maximum ship speed attainable at full power, astern mode*

Ice thickness	mm	0	18	29
Ship speed	m/s	0.97	0.59	0.33

* The values of ship speed listed in Table 3 are calculated by the authors based on self-propulsion test results given by Leiviskä (2004).

1.3 Present Work

In this paper, a dual-direction ship behavior is studied through a numerical procedure developed in previous works simulating level ice–ship interaction during continuous-mode icebreaking. The detailed methodology is introduced by a case study carried out with the model of the icebreaking tanker M/T Uikku. Since the propeller–ice–hull interaction, especially for astern mode, involves really complicated physical processes, direct modeling is not pursued in the present work. Instead, this effect is incorporated into the numerical model by calibrating the numerical model with model tests conducted by Leiviskä (2004) introduced in section 1.2.3. Then, the performance of the ship in both ahead and astern modes is predicted by the numerical procedure. The numerical prediction of the bare hull ice resistance is verified by model test results. In addition, the thrust deduction factor in ice is discussed.

2. The Numerical Procedure

The numerical procedure was developed and further improved over the authors' previous works to simulate the icebreaking process in the time domain. Due to the lack of sufficient understanding of physics of icebreaking especially by moving structures, the work was conducted by combining rational theoretical analysis with knowledge obtained empirically, i.e., semi-empirically. The icebreaking pattern observed in model- and full-scale tests is reproduced by the formation of bending cracks during an icebreaking run. Having been validated with full-scale trials, the numerical procedure can be used as a tool for performance prediction. In this chapter, the basic idea of the numerical model is briefly introduced; more detailed description is presented in Tan et al. (2013).

2.1 Ship Motions

In the numerical model, the interaction between ship motions and the ice load is simulated by solving the ship's dynamic equations of motion in the time domain with a step-by-step integration scheme. Iterations are performed during each time step to solve the interdependence between ship motions and the ice load. The ship is able to move in six degrees of freedom (Fig. 5) with the coupling between motions included.

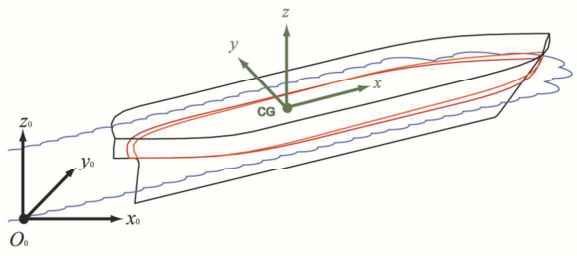

Fig. 5 Reference frames

2.2 Resistance Components in Ice

It is assumed that ice floes are cleared by the advancing ship hull immediately after the bending failure of the intact ice sheet. The resistance from ice floe clearing and submergence is considered not to interfere with the next contact. Similarly, the open water resistance is also separated. Thus the total resistance acting on the ship during icebreaking can be broken down into the following parts (see e.g. Spencer and Jones, 2001):

$$R_{\mathrm{T}} = \underbrace{R_{\mathrm{brk}} + R_{\mathrm{sbmg}}}_{R_{\mathrm{I}}} + R_{\mathrm{ow}} \tag{17}$$

where R_{brk} is the ice resistance arising from breaking, i.e., crushing and bending, of the intact ice; R_{sbmg} is the resistance due to the interaction between ship hull and the broken ice floes; R_{I} is the total ice resistance; R_{ow} is the open water resistance.

In the numerical model, the icebreaking component, R_{brk}, which is the immediate cause for the forming of breaking pattern, is calculated numerically by integrating the pressure induced by the contact with the ice edge along the waterline. R_{sbmg} is calculated as a global load with the empirical formula given by Lindqvist (1989). The open water resistance, R_{ow}, is measured in open water towed tests.

2.3 Icebreaking Force

By assembling the ice load models describing various aspects of icebreaking proposed by past works (e.g. Kashteljan, 1968; Enkvist, 1972; Milano, 1973; Varsta, 1983; Izumiyama et al., 1991), the icebreaking force is obtained through a contact algorithm which detects the contact zones between the ship hull and the ice edge by computational geometry algorithms.

2.3.1 Ice Crushing Failure

The crushing force, F_{cr}, which is normal to the contact plane on each of the contact zones, is calculated by the product of the average crushing pressure, p_{av}, and the crushing area, A_{cr}. The average crushing pressure is observed to be dependent on the crushing area, which is often known as the "pressure–area relation". The pressure–area relation is investigated by Tan et al. (2013) through a parametric study.

2.3.2 Ice Bending Failure

At each of the contact zones, the wedge shaped ice edge is loaded by the ship hull at a certain loading speed and hull frame angle. If the vertical force on the ice wedge exceeds the bending failure load, then the ice bends and the wedge is deleted. An example of the ice edge update procedure is shown in Fig. 6.

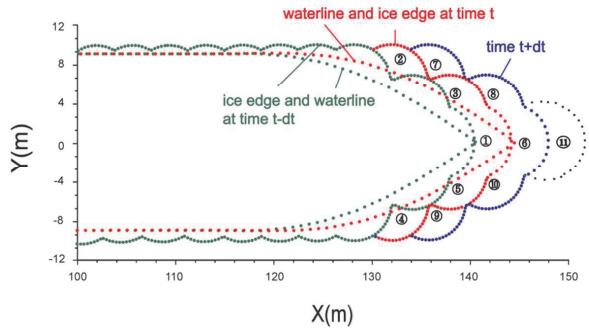

Fig. 6 Example of the ice edge update procedure and the icebreaking pattern

It has been observed in field and model-scale tests (e.g. Izumiyama et al., 1991; Valanto, 1992) that the breaking length of the ice slab is dependent on the loading rate. In the numerical model, the size of the broken ice floe is described by the length and depth of the ice cusp, as depicted in Fig. 7. The breaking length is determined by the material properties of the ice and the loading rate, and the depth of ice cusp is determined by empirical formula given by Milano (1973).

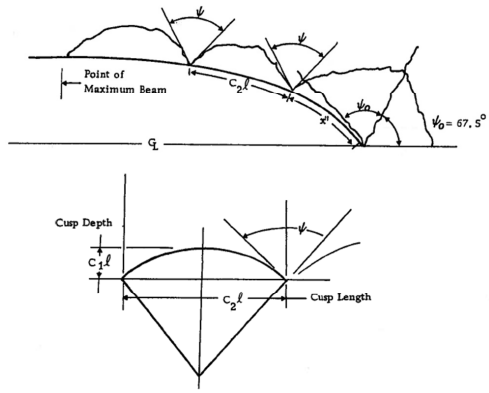

Fig. 7 Idealized bending model of icebreaking (*l* denotes the characteristic length of ice) (Milano, 1973)

2.3 Calculated Icebreaking pattern and Time Histories

Examples of the calculated icebreaking pattern, time histories of ship motions and ice resistance and pitch moment are plotted in Fig. 8 through Fig. 10. Note that the time axes in the following figures are in model-scale.

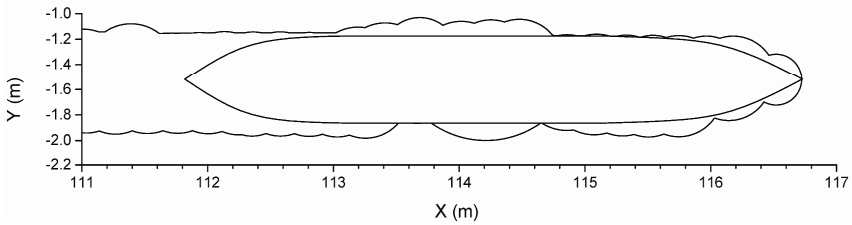

Fig. 8 Icebreaking pattern (h_i = 29mm, v_x=0.292m/s, astern mode)

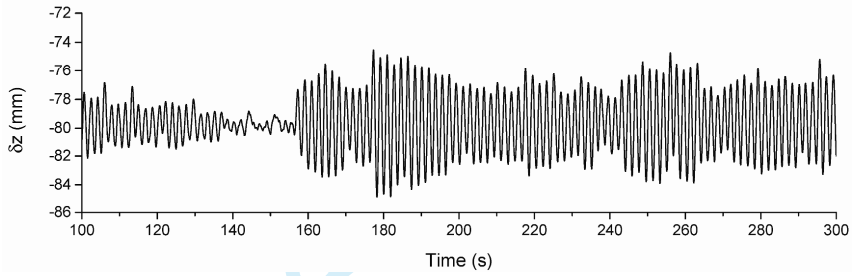

(a) Heave

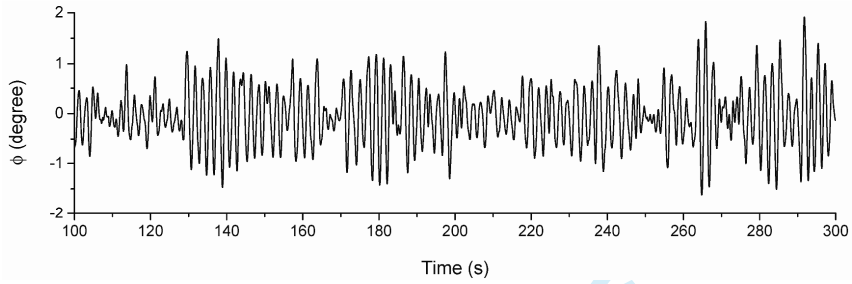

(b) Roll

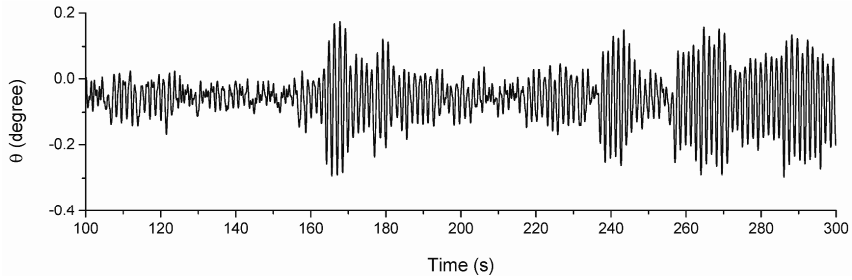

(c) Pitch

Fig. 9 Time histories of motions (h_i = 29mm, v_x=0.292m/s, astern mode)

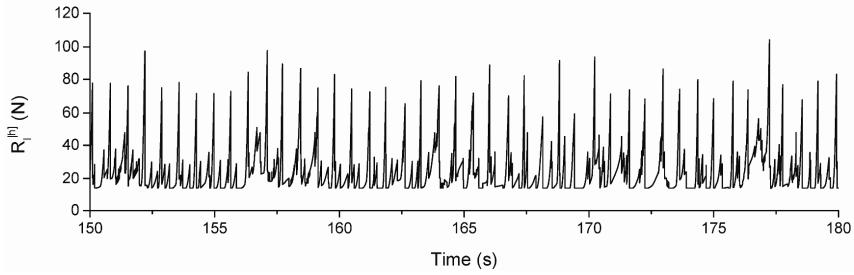

(a) Ice resistance (in surge)

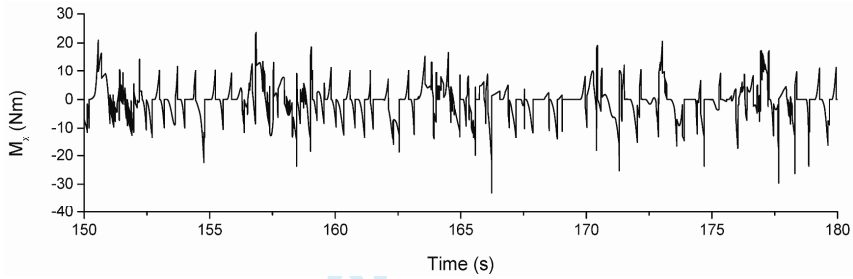

(b) Roll moment

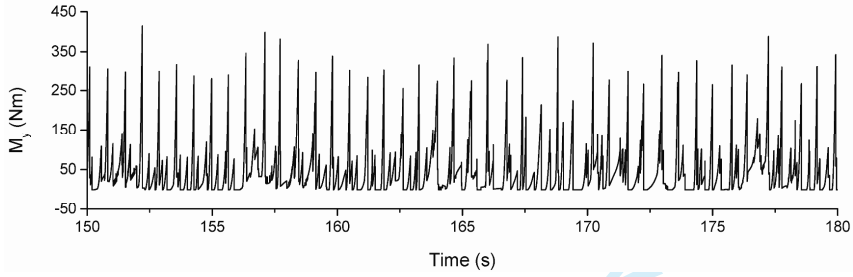

(c) Pitch moment

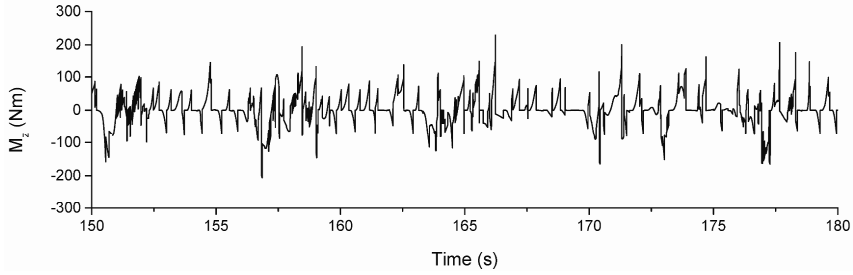

(d) Yaw moment

Fig. 10 Time histories of ice resisting force and moments (h_i = 29mm, v_x=0.292m/s, astern mode)

3. Investigation of the Influence of Propeller–Hull–Ice Interaction

In this chapter, the flushing effect of propeller flow on broken ice resistance is investigated through a case study with the model of M/T Uikku. With the actual total thrust, the open water thrust deduction factors and open water resistance obtained from the model tests conducted by Leiviskä (2004) as inputs, numerical experiments are carried to fit the calculated ship speeds at the installed propulsion power to the tested data points by adjusting the relevant coefficient in the numerical model.

3.1 M/T Uikku

M/T Uikku is one of the earliest ice-going ships outfitted with an azimuthing propulsion system. Built in 1977, the product tanker was originally installed with a conventional propeller-rudder propulsion system. In 1993, a conversion is made to replace the propeller-rudder configuration with an 11.4 MW Azipod unit with a "pushing" type azimuth propeller (Fig. 11).

Fig. 11 Conversion on M/T Uikku (source: www.abb.com)

Due to the design of the stern, the propeller is not permitted to azimuth fully in 360°. As a result, the efficiency in astern mode is lower than that in the ahead mode due to the inversely rotating propeller.

The main particulars of the ship are listed in Table 4. The geometry scale factor of the model is 31.56.

Table 4 Ship parameters

Parameter	Notation	Dimension	Full Scale Value	Model Scale Value
Length over all	LOA	m	164.4	5.21
Length between perpendiculars	l_{pp}	m	150.0	4.75
Breath, moulded	B	m	22.2	0.70
Draught, icebreaking	D	m	9.5	0.30
Installed propulsion power	P_D	W	11.4×10^6	64.55
Propeller diameter	D_P	m	5.6	0.179

3.2 Propulsion Characteristics

3.2.1 Thrust and torque coefficients

The thrust and torque coefficients are plotted in Fig. 12 versus the advance ratio. The corresponding propeller shaft speed is 15 s^{-1}. As can be seen from the figure, when going astern, the propeller has to rotate in the opposite direction, which results in a lower efficiency.

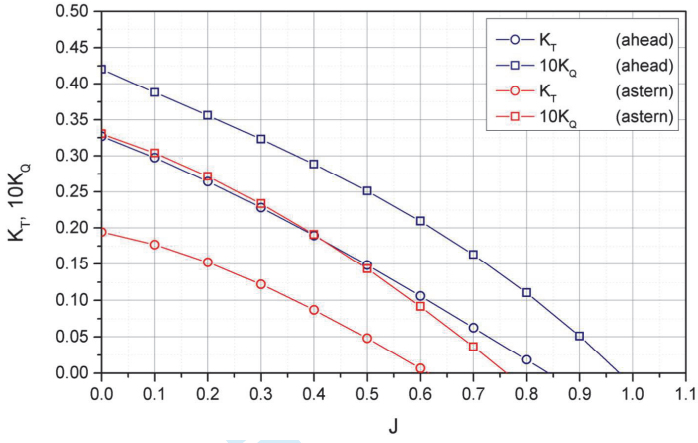

Fig. 12 K_T, K_Q curves (n = 15 s^{-1})

3.2.2 Net thrust in ice

The total thrusts at full propulsion power obtained through K_T, K_Q curves are plotted versus ship speed in Fig. 13, where the open water resistances are also plotted.

By using the thrust deduction factors given by Fig. 2 and Fig. 3, the net thrust in ice, T_{net}, is also plotted in Fig. 13.

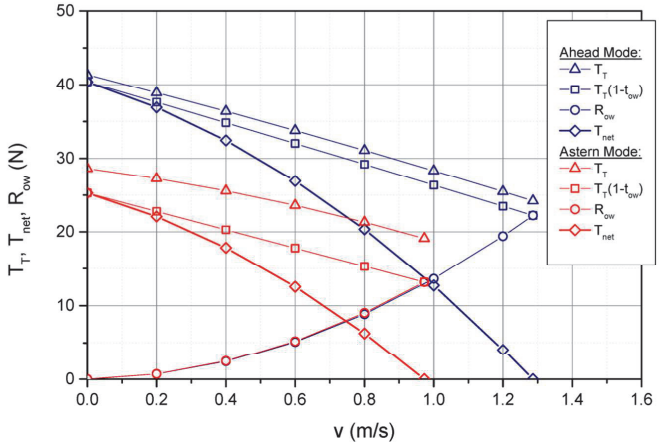

Fig. 13 Total thrust, T_T, open water resistance, R_{ow}, and net thrust, T_{net}

The T_{net} curves shown in Fig. 13 are incorporated into the numerical model as propulsion forces to predict the performance of the ship in level ice.

3.3 Calibrating the Numerical Model

As explained in Section 1.2, when the ship is running astern, the total hull resistance is reduced due to the flushing effect of propeller flow on the broken ice resistance, R_{sbmg}.

In the numerical model, R_{sbmg} is calculated by the empirical formula given by Lindqvist (1989), where it is assumed that 70% of the hull bottom length is covered by broken ice floes during icebreaking, so that the area of the flat bottom covered with ice can be expressed as:

$$A_u = B \cdot (0.7 l_{pp} - D / \tan\phi - 0.25B / \tan\alpha) \quad (18)$$

where ϕ and α denote the stem angle and the waterline angle, respectively.

Since the Lindqvist's resistance formula was originally developed for ships going ahead, this coefficient representing the coverage is calibrated in the numerical model to account for the flushing effect of propeller flow on broken ice floes when going astern.

In this paper, the calibration is done by fitting the numerical calculations to the model test results presented in Table 3. That is, for each of the ice thicknesses listed in Table 3, the ship speed at the full installed propulsion power is calculated by the numerical procedure. By adjusting the Lindqvist's coverage coefficient in the numerical model, it is found that a value of 0.32 gives the best fit to the model test results. This value is used in the numerical procedure for the performance prediction for astern mode. For ahead mode, the original value of 0.7 proposed by Lindqvist (1989) is followed.

With the calibrated broken ice resistance component, the ship's performance in a range of ice thicknesses is predicted with the numerical procedure, as is plotted in Fig. 14. In the calculations of ship performance presented in Fig. 14, the average values of the material properties of ice measured in the model tests are adopted, as listed in Table 5.

Table 5 Average values of model ice properties

Parameter	Notation	Dimension	Value
Density	ρ_i	kg/m^3	880
Young's modulus	E	MPa	34.7
Poisson ratio	ν		0.33
Crushing strength	σ_{cr}	kPa	76.7
Bending strength	σ_f	kPa	24.3
Coefficient of friction	μ		0.05

It is clearly shown in Fig. 14 that the ship's performance in thick ice in astern mode is better than that in ahead mode even if the total thrust is lower.

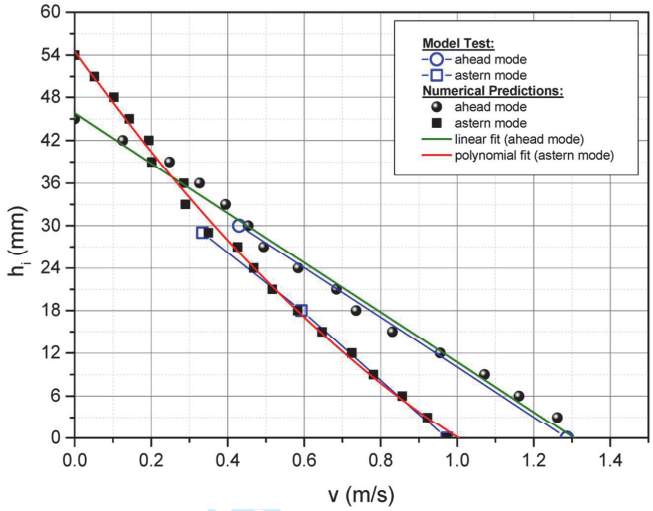

Fig. 14 *h*–*v* curve

The predicted bare hull ice resistance versus ship speed is plotted in Fig. 15 against the model test results. It is shown that a good agreement is achieved.

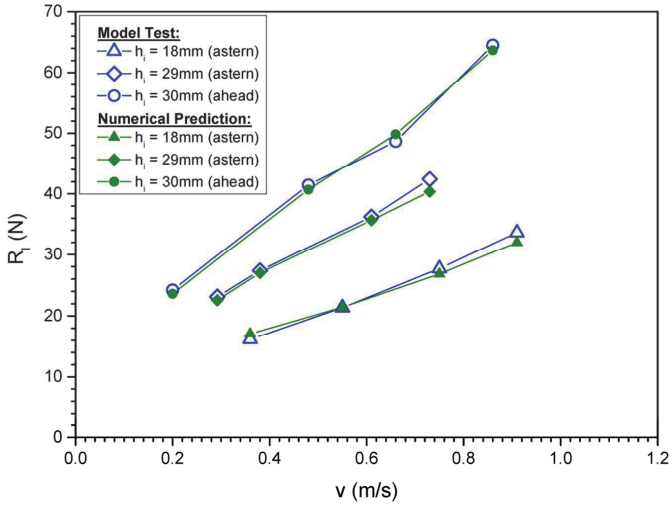

Fig. 15 Bare hull ice resistance

It should be noted that, in order to verify the numerical predictions with the model test results, the calculations in Fig. 15 are done with the actual values of the ice material properties measured in each test, as listed in Table 6.

Table 6 Model ice properties for resistance tests

Direction	h_i (mm)	σ_f (kPa)	σ_{cr} (kPa)	E (MPa)
Astern	18	21.6	100.2	73.0
Astern	29	26.9	69.4	24.2
Ahead	30	28.1	69.3	23.8

4. Thrust Deduction in Ice

In Fig. 16, the predicted bare hull ice resistance versus ship speed for a series of ice thicknesses is plotted. In these calculations, the average values of the material properties of ice listed in Table 5 are used so that the results are comparable to each other.

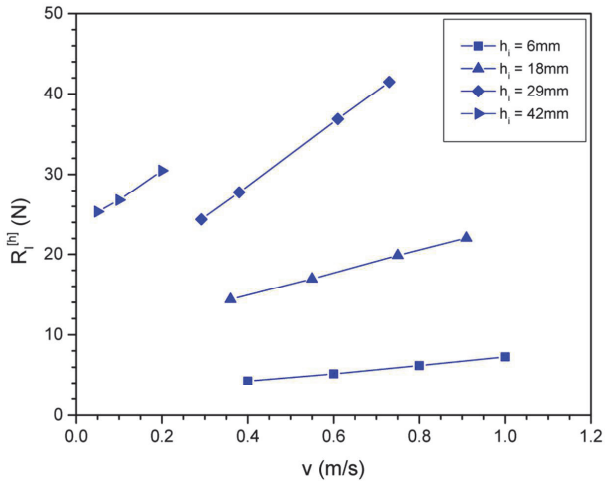

Fig. 16 Predicted bare hull ice resistance vs. ship speed

In Fig. 17, an example of the procedure of deriving thrust deduction in ice is illustrated. For each ice thickness, firstly, the ship speed at the full installed propulsion power is looked up from the h–v curve for astern mode plotted in Fig. 14. Then, the net thrust and bare hull ice resistance at this speed is obtained from the T_{net} curve (Fig. 13) and the calculation given by Fig. 16. According to Eq. (7), the added resistance from propeller–ice interaction, ΔR_I, i.e., the thrust deduction in ice, is equal to the difference between the net thrust, T_{net}, and the bare hull ice resistance, $R_I^{[h]}$.

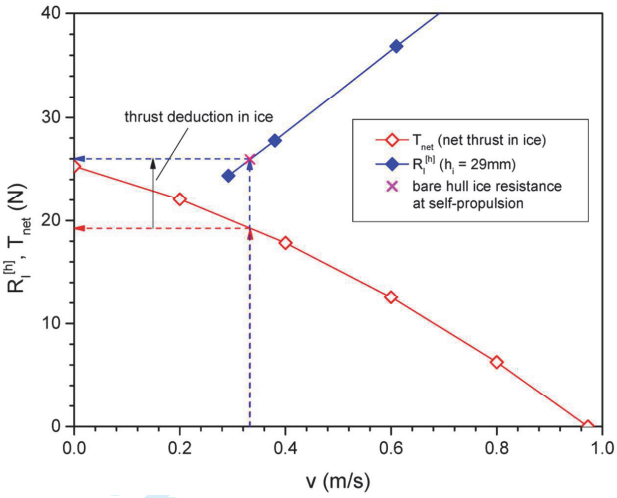

Fig. 17 Example of deriving the added resistance due to propeller–ice interaction

The thrust deduction in ice at self-propulsion with the installed propulsion power for a range of ice thicknesses is plotted in Fig. 18.

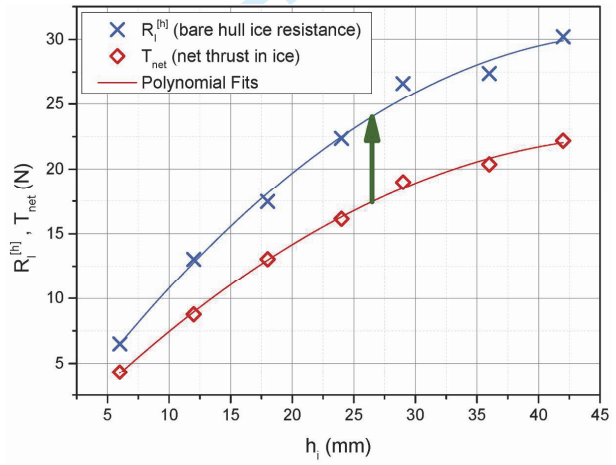

Fig. 18 Thrust deduction in ice at self-propulsion in astern mode

The thrust deduction factor in ice, t_I, and the overall thrust deduction factor, t_{TOT}, defined in Eq. (9) and Eq.(11), are plotted in Fig. 19 versus ship speed.

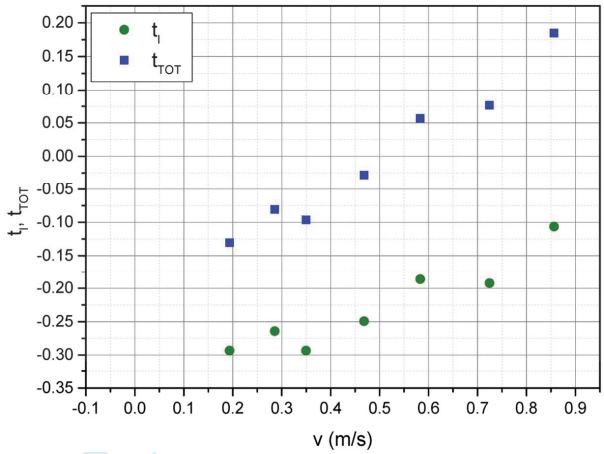

Fig. 19 Thrust deduction factors during icebreaking

5. Conclusions

The performance of a dual-direction ship is investigated through a numerical procedure simulating continuous-mode icebreaking in level ice. With knowledge obtained from model tests, the thrust deduction during icebreaking for the astern mode is especially looked into. The main conclusions are as follows:

1) The actual thrust, open water thrust deduction factor and the open water resistance of Uikku model is derived based on model tests; the obtained net thrust in ice is applied to the numerical procedure to simulate the ship's performance in both ahead and astern modes.
2) By fitting to the model test results, the effect of propeller flow on broken ice resistance in astern mode is accounted for by modifying the underwater area covered by broken ice in Lindqvist's (1989) submergence and clearing resistance formula.
3) The *h*–*v* curves which represent the ship's performance at full propulsion power in a range of ice thicknesses are calculated with the numerical procedure.
4) As shown in Fig. 4, the absolute value of the added resistance due to propeller–ice interaction increases with ship speed (different propulsion power) for a certain ice thickness.
5) As shown in Fig. 18, for the installed propulsion power, thrust deduction in thick ice is higher than that in thin ice.
6) For the installed propulsion power, the absolute value of the thrust deduction factor in pure ice decreases with ship speed generally (Fig. 19).

The current study is based on a particular ship – M/T Uikku, where limited model test results are extrapolated to draw relations between thrust deduction in ice and parameters such as ice thickness and ship speed. Future works recommended are:

1) In reality, the propeller flow may also have an effect on the breaking of level ice by lowering the water pressure below the intact ice. Future work is needed to clarify this effect quantitatively.
2) The numerical model calibration is done with limited information from model tests, it is suggested that more case studies be conducted to further verify the numerical model.

Acknowledgement

The authors would like to acknowledge TOTAL E&P NORGE AS for funding of the research. The Research Council of Norway through the Centre for Ships and Ocean Structures in the Norwegian University of Science and Technology is also acknowledged.

References

Enkvist, E., 1972. On the ice resistance encountered by ships operating in the continuous mode of icebreaking. Report No. 24. The Swedish Academy of Engineering Science in Finland.

Faltinsen, O.M., 1990. Sea loads on ships and offshore structures. Cambridge University Press, Cambridge, UK.

Jansson, J-E.,1956a. Ice-breakers and their design, Pt. I. European Shipbuildings, No. 5, pp. 112–128.

Jansson, J-E., 1956b. Ice-breakers and their design, Pt. II. European Shipbuildings, No. 6, pp. 143–151.

Jones, S.J., 2004. Ships in ice – a review. 25th Symposium on Naval Hydrodynamics, St. John's, Newfoundland and Labrador, Canada, August 2004.

Izumiyama, K., Kitagawa, H., Koyama, K. and Uto, S., 1991. On the interaction between a conical structure and ice sheet. Proc. 11th International Conference on Port and Ocean Engineering under Arctic Conditions (POAC), St. John's, Canada. pp.155–166.

Juurmaa, K., Wilkman, G. and Bäckström, M., 1995. New ice breaking tanker concept for the Arctic (DAT). Proceedings of the 13th International Conference on Port and Ocean Engineering under Arctic Conditions (POAC), August 15–18, Murmansk, Russia.

Kashteljan, V.I., Poznjak, I.I. and Ryvlin, A.J., 1968. Ice resistance to motion of a ship. Sudostroyeniye, Leningrad, Russia.

Leiviskä, T., 2004. The propulsion coefficients of ships in ice and in open water (in Finish). Helsinki University of Technology, Ship Laboratory, Report M-287, Espoo, Finland.

Lindqvist, G., 1989. A straightforward method for calculation of ice resistance of ships. Proceedings of POAC 1989. pp. 722–735.

Milano, V.R., 1973. Ship resistance to continuous motion in ice. SNAME Transactions, Vol. 81, pp. 274–306.

Spencer, D. and Jones, S.J., 2001. Model-scale/full-scale correlation in open water and ice for Canadian Coast Guard "R-Class" icebreakers. Journal of Ship Research, Vol. 45, No. 4, pp. 249–261.

Tan, X., Su, B., Riska, K. and Moan, T., 2013. A six-degrees-of-freedom numerical model for level ice–ship interaction. Cold Regions Science and Technology, Vol. 92, pp. 1–16.

Valanto, P., 1992. The icebreaking problem in two dimensions: experiments and theory. Journal of Ship Research, Vol. 36, pp. 299–316.

Varsta, P., 1983. On the mechanics of ice load on ships in level ice in the Baltic Sea. Ph.D. Thesis, Helsinki University of Technology, Finland.

Vocke, M., Ranki, E., Uuskallio, A., Niini, M. and Wilkman, G., 2011. Experience from Vessels Operating in Ice in the Double Acting Principle. OTC Arctic Technology Conference , 7-9 February 2011, Houston, Texas, USA.

Previous PhD theses published at the Department of Marine Technology
(Earlier: Faculty of Marine Technology)

NORWEGIAN UNIVERSITY OF SCIENCE AND TECHNOLOGY

Report No.	Author	Title
	Kavlie, Dag	Optimization of Plane Elastic Grillages, 1967
	Hansen, Hans R.	Man-Machine Communication and Data-Storage Methods in Ship Structural Design, 1971
	Gisvold, Kaare M.	A Method for non-linear mixed -integer programming and its Application to Design Problems, 1971
	Lund, Sverre	Tanker Frame Optimalization by means of SUMT-Transformation and Behaviour Models, 1971
	Vinje, Tor	On Vibration of Spherical Shells Interacting with Fluid, 1972
	Lorentz, Jan D.	Tank Arrangement for Crude Oil Carriers in Accordance with the new Anti-Pollution Regulations, 1975
	Carlsen, Carl A.	Computer-Aided Design of Tanker Structures, 1975
	Larsen, Carl M.	Static and Dynamic Analysis of Offshore Pipelines during Installation, 1976
UR-79-01	Brigt Hatlestad, MK	The finite element method used in a fatigue evaluation of fixed offshore platforms. (Dr.Ing. Thesis)
UR-79-02	Erik Pettersen, MK	Analysis and design of cellular structures. (Dr.Ing. Thesis)
UR-79-03	Sverre Valsgård, MK	Finite difference and finite element methods applied to nonlinear analysis of plated structures. (Dr.Ing. Thesis)
UR-79-04	Nils T. Nordsve, MK	Finite element collapse analysis of structural members considering imperfections and stresses due to fabrication. (Dr.Ing. Thesis)
UR-79-05	Ivar J. Fylling, MK	Analysis of towline forces in ocean towing systems. (Dr.Ing. Thesis)
UR-80-06	Nils Sandsmark, MM	Analysis of Stationary and Transient Heat Conduction by the Use of the Finite Element Method. (Dr.Ing. Thesis)
UR-80-09	Sverre Haver, MK	Analysis of uncertainties related to the stochastic modeling of ocean waves. (Dr.Ing. Thesis)
UR-81-15	Odland, Jonas	On the Strength of welded Ring stiffened cylindrical Shells primarily subjected to axial Compression
UR-82-17	Engesvik, Knut	Analysis of Uncertainties in the fatigue Capacity of Welded Joints

UR-82-18	Rye, Henrik	Ocean wave groups
UR-83-30	Eide, Oddvar Inge	On Cumulative Fatigue Damage in Steel Welded Joints
UR-83-33	Mo, Olav	Stochastic Time Domain Analysis of Slender Offshore Structures
UR-83-34	Amdahl, Jørgen	Energy absorption in Ship-platform impacts
UR-84-37	Mørch, Morten	Motions and mooring forces of semi submersibles as determined by full-scale measurements and theoretical analysis
UR-84-38	Soares, C. Guedes	Probabilistic models for load effects in ship structures
UR-84-39	Aarsnes, Jan V.	Current forces on ships
UR-84-40	Czujko, Jerzy	Collapse Analysis of Plates subjected to Biaxial Compression and Lateral Load
UR-85-46	Alf G. Engseth, MK	Finite element collapse analysis of tubular steel offshore structures. (Dr.Ing. Thesis)
UR-86-47	Dengody Sheshappa, MP	A Computer Design Model for Optimizing Fishing Vessel Designs Based on Techno-Economic Analysis. (Dr.Ing. Thesis)
UR-86-48	Vidar Aanesland, MH	A Theoretical and Numerical Study of Ship Wave Resistance. (Dr.Ing. Thesis)
UR-86-49	Heinz-Joachim Wessel, MK	Fracture Mechanics Analysis of Crack Growth in Plate Girders. (Dr.Ing. Thesis)
UR-86-50	Jon Taby, MK	Ultimate and Post-ultimate Strength of Dented Tubular Members. (Dr.Ing. Thesis)
UR-86-51	Walter Lian, MH	A Numerical Study of Two-Dimensional Separated Flow Past Bluff Bodies at Moderate KC-Numbers. (Dr.Ing. Thesis)
UR-86-52	Bjørn Sortland, MH	Force Measurements in Oscillating Flow on Ship Sections and Circular Cylinders in a U-Tube Water Tank. (Dr.Ing. Thesis)
UR-86-53	Kurt Strand, MM	A System Dynamic Approach to One-dimensional Fluid Flow. (Dr.Ing. Thesis)
UR-86-54	Arne Edvin Løken, MH	Three Dimensional Second Order Hydrodynamic Effects on Ocean Structures in Waves. (Dr.Ing. Thesis)
UR-86-55	Sigurd Falch, MH	A Numerical Study of Slamming of Two-Dimensional Bodies. (Dr.Ing. Thesis)
UR-87-56	Arne Braathen, MH	Application of a Vortex Tracking Method to the Prediction of Roll Damping of a Two-Dimension Floating Body. (Dr.Ing. Thesis)

UR-87-57	Bernt Leira, MK	Gaussian Vector Processes for Reliability Analysis involving Wave-Induced Load Effects. (Dr.Ing. Thesis)
UR-87-58	Magnus Småvik, MM	Thermal Load and Process Characteristics in a Two-Stroke Diesel Engine with Thermal Barriers (in Norwegian). (Dr.Ing. Thesis)
MTA-88-59	Bernt Arild Bremdal, MP	An Investigation of Marine Installation Processes – A Knowledge - Based Planning Approach. (Dr.Ing. Thesis)
MTA-88-60	Xu Jun, MK	Non-linear Dynamic Analysis of Space-framed Offshore Structures. (Dr.Ing. Thesis)
MTA-89-61	Gang Miao, MH	Hydrodynamic Forces and Dynamic Responses of Circular Cylinders in Wave Zones. (Dr.Ing. Thesis)
MTA-89-62	Martin Greenhow, MH	Linear and Non-Linear Studies of Waves and Floating Bodies. Part I and Part II. (Dr.Techn. Thesis)
MTA-89-63	Chang Li, MH	Force Coefficients of Spheres and Cubes in Oscillatory Flow with and without Current. (Dr.Ing. Thesis
MTA-89-64	Hu Ying, MP	A Study of Marketing and Design in Development of Marine Transport Systems. (Dr.Ing. Thesis)
MTA-89-65	Arild Jæger, MH	Seakeeping, Dynamic Stability and Performance of a Wedge Shaped Planing Hull. (Dr.Ing. Thesis)
MTA-89-66	Chan Siu Hung, MM	The dynamic characteristics of tilting-pad bearings
MTA-89-67	Kim Wikstrøm, MP	Analysis av projekteringen for ett offshore projekt. (Licenciat-avhandling)
MTA-89-68	Jiao Guoyang, MK	Reliability Analysis of Crack Growth under Random Loading, considering Model Updating. (Dr.Ing. Thesis)
MTA-89-69	Arnt Olufsen, MK	Uncertainty and Reliability Analysis of Fixed Offshore Structures. (Dr.Ing. Thesis)
MTA-89-70	Wu Yu-Lin, MR	System Reliability Analyses of Offshore Structures using improved Truss and Beam Models. (Dr.Ing. Thesis)
MTA-90-71	Jan Roger Hoff, MH	Three-dimensional Green function of a vessel with forward speed in waves. (Dr.Ing. Thesis)
MTA-90-72	Rong Zhao, MH	Slow-Drift Motions of a Moored Two-Dimensional Body in Irregular Waves. (Dr.Ing. Thesis)
MTA-90-73	Atle Minsaas, MP	Economical Risk Analysis. (Dr.Ing. Thesis)
MTA-90-74	Knut-Aril Farnes, MK	Long-term Statistics of Response in Non-linear Marine Structures. (Dr.Ing. Thesis)

MTA-90-75	Torbjørn Sotberg, MK	Application of Reliability Methods for Safety Assessment of Submarine Pipelines. (Dr.Ing. Thesis)
MTA-90-76	Zeuthen, Steffen, MP	SEAMAID. A computational model of the design process in a constraint-based logic programming environment. An example from the offshore domain. (Dr.Ing. Thesis)
MTA-91-77	Haagensen, Sven, MM	Fuel Dependant Cyclic Variability in a Spark Ignition Engine - An Optical Approach. (Dr.Ing. Thesis)
MTA-91-78	Løland, Geir, MH	Current forces on and flow through fish farms. (Dr.Ing. Thesis)
MTA-91-79	Hoen, Christopher, MK	System Identification of Structures Excited by Stochastic Load Processes. (Dr.Ing. Thesis)
MTA-91-80	Haugen, Stein, MK	Probabilistic Evaluation of Frequency of Collision between Ships and Offshore Platforms. (Dr.Ing. Thesis)
MTA-91-81	Sødahl, Nils, MK	Methods for Design and Analysis of Flexible Risers. (Dr.Ing. Thesis)
MTA-91-82	Ormberg, Harald, MK	Non-linear Response Analysis of Floating Fish Farm Systems. (Dr.Ing. Thesis)
MTA-91-83	Marley, Mark J., MK	Time Variant Reliability under Fatigue Degradation. (Dr.Ing. Thesis)
MTA-91-84	Krokstad, Jørgen R., MH	Second-order Loads in Multidirectional Seas. (Dr.Ing. Thesis)
MTA-91-85	Molteberg, Gunnar A., MM	The Application of System Identification Techniques to Performance Monitoring of Four Stroke Turbocharged Diesel Engines. (Dr.Ing. Thesis)
MTA-92-86	Mørch, Hans Jørgen Bjelke, MH	Aspects of Hydrofoil Design: with Emphasis on Hydrofoil Interaction in Calm Water. (Dr.Ing. Thesis)
MTA-92-87	Chan Siu Hung, MM	Nonlinear Analysis of Rotordynamic Instabilities in Highspeed Turbomachinery. (Dr.Ing. Thesis)
MTA-92-88	Bessason, Bjarni, MK	Assessment of Earthquake Loading and Response of Seismically Isolated Bridges. (Dr.Ing. Thesis)
MTA-92-89	Langli, Geir, MP	Improving Operational Safety through exploitation of Design Knowledge - an investigation of offshore platform safety. (Dr.Ing. Thesis)
MTA-92-90	Sævik, Svein, MK	On Stresses and Fatigue in Flexible Pipes. (Dr.Ing. Thesis)

MTA-92-91	Ask, Tor Ø., MM	Ignition and Flame Growth in Lean Gas-Air Mixtures. An Experimental Study with a Schlieren System. (Dr.Ing. Thesis)
JMTA-86-92	Hessen, Gunnar, MK	Fracture Mechanics Analysis of Stiffened Tubular Members. (Dr.Ing. Thesis)
MTA-93-93	Steinebach, Christian, MM	Knowledge Based Systems for Diagnosis of Rotating Machinery. (Dr.Ing. Thesis)
MTA-93-94	Dalane, Jan Inge, MK	System Reliability in Design and Maintenance of Fixed Offshore Structures. (Dr.Ing. Thesis)
MTA-93-95	Steen, Sverre, MH	Cobblestone Effect on SES. (Dr.Ing. Thesis)
MTA-93-96	Karunakaran, Daniel, MK	Nonlinear Dynamic Response and Reliability Analysis of Drag-dominated Offshore Platforms. (Dr.Ing. Thesis)
MTA-93-97	Hagen, Arnulf, MP	The Framework of a Design Process Language. (Dr.Ing. Thesis)
MTA-93-98	Nordrik, Rune, MM	Investigation of Spark Ignition and Autoignition in Methane and Air Using Computational Fluid Dynamics and Chemical Reaction Kinetics. A Numerical Study of Ignition Processes in Internal Combustion Engines. (Dr.Ing. Thesis)
MTA-94-99	Passano, Elizabeth, MK	Efficient Analysis of Nonlinear Slender Marine Structures. (Dr.Ing. Thesis)
MTA-94-100	Kvålsvold, Jan, MH	Hydroelastic Modelling of Wetdeck Slamming on Multihull Vessels. (Dr.Ing. Thesis)
MTA-94-102	Bech, Sidsel M., MK	Experimental and Numerical Determination of Stiffness and Strength of GRP/PVC Sandwich Structures. (Dr.Ing. Thesis)
MTA-95-103	Paulsen, Hallvard, MM	A Study of Transient Jet and Spray using a Schlieren Method and Digital Image Processing. (Dr.Ing. Thesis)
MTA-95-104	Hovde, Geir Olav, MK	Fatigue and Overload Reliability of Offshore Structural Systems, Considering the Effect of Inspection and Repair. (Dr.Ing. Thesis)
MTA-95-105	Wang, Xiaozhi, MK	Reliability Analysis of Production Ships with Emphasis on Load Combination and Ultimate Strength. (Dr.Ing. Thesis)
MTA-95-106	Ulstein, Tore, MH	Nonlinear Effects of a Flexible Stern Seal Bag on Cobblestone Oscillations of an SES. (Dr.Ing. Thesis)
MTA-95-107	Solaas, Frøydis, MH	Analytical and Numerical Studies of Sloshing in Tanks. (Dr.Ing. Thesis)
MTA-95-108	Hellan, Øyvind, MK	Nonlinear Pushover and Cyclic Analyses in Ultimate Limit State Design and Reassessment of Tubular Steel Offshore Structures. (Dr.Ing. Thesis)

MTA-95-109	Hermundstad, Ole A., MK	Theoretical and Experimental Hydroelastic Analysis of High Speed Vessels. (Dr.Ing. Thesis)
MTA-96-110	Bratland, Anne K., MH	Wave-Current Interaction Effects on Large-Volume Bodies in Water of Finite Depth. (Dr.Ing. Thesis)
MTA-96-111	Herfjord, Kjell, MH	A Study of Two-dimensional Separated Flow by a Combination of the Finite Element Method and Navier-Stokes Equations. (Dr.Ing. Thesis)
MTA-96-112	Æsøy, Vilmar, MM	Hot Surface Assisted Compression Ignition in a Direct Injection Natural Gas Engine. (Dr.Ing. Thesis)
MTA-96-113	Eknes, Monika L., MK	Escalation Scenarios Initiated by Gas Explosions on Offshore Installations. (Dr.Ing. Thesis)
MTA-96-114	Erikstad, Stein O., MP	A Decision Support Model for Preliminary Ship Design. (Dr.Ing. Thesis)
MTA-96-115	Pedersen, Egil, MH	A Nautical Study of Towed Marine Seismic Streamer Cable Configurations. (Dr.Ing. Thesis)
MTA-97-116	Moksnes, Paul O., MM	Modelling Two-Phase Thermo-Fluid Systems Using Bond Graphs. (Dr.Ing. Thesis)
MTA-97-117	Halse, Karl H., MK	On Vortex Shedding and Prediction of Vortex-Induced Vibrations of Circular Cylinders. (Dr.Ing. Thesis)
MTA-97-118	Igland, Ragnar T., MK	Reliability Analysis of Pipelines during Laying, considering Ultimate Strength under Combined Loads. (Dr.Ing. Thesis)
MTA-97-119	Pedersen, Hans-P., MP	Levendefiskteknologi for fiskefartøy. (Dr.Ing. Thesis)
MTA-98-120	Vikestad, Kyrre, MK	Multi-Frequency Response of a Cylinder Subjected to Vortex Shedding and Support Motions. (Dr.Ing. Thesis)
MTA-98-121	Azadi, Mohammad R. E., MK	Analysis of Static and Dynamic Pile-Soil-Jacket Behaviour. (Dr.Ing. Thesis)
MTA-98-122	Ulltang, Terje, MP	A Communication Model for Product Information. (Dr.Ing. Thesis)
MTA-98-123	Torbergsen, Erik, MM	Impeller/Diffuser Interaction Forces in Centrifugal Pumps. (Dr.Ing. Thesis)
MTA-98-124	Hansen, Edmond, MH	A Discrete Element Model to Study Marginal Ice Zone Dynamics and the Behaviour of Vessels Moored in Broken Ice. (Dr.Ing. Thesis)
MTA-98-125	Videiro, Paulo M., MK	Reliability Based Design of Marine Structures. (Dr.Ing. Thesis)
MTA-99-126	Mainçon, Philippe, MK	Fatigue Reliability of Long Welds Application to Titanium Risers. (Dr.Ing. Thesis)

MTA-99-127	Haugen, Elin M., MH	Hydroelastic Analysis of Slamming on Stiffened Plates with Application to Catamaran Wetdecks. (Dr.Ing. Thesis)
MTA-99-128	Langhelle, Nina K., MK	Experimental Validation and Calibration of Nonlinear Finite Element Models for Use in Design of Aluminium Structures Exposed to Fire. (Dr.Ing. Thesis)
MTA-99-129	Berstad, Are J., MK	Calculation of Fatigue Damage in Ship Structures. (Dr.Ing. Thesis)
MTA-99-130	Andersen, Trond M., MM	Short Term Maintenance Planning. (Dr.Ing. Thesis)
MTA-99-131	Tveiten, Bård Wathne, MK	Fatigue Assessment of Welded Aluminium Ship Details. (Dr.Ing. Thesis)
MTA-99-132	Søreide, Fredrik, MP	Applications of underwater technology in deep water archaeology. Principles and practice. (Dr.Ing. Thesis)
MTA-99-133	Tønnessen, Rune, MH	A Finite Element Method Applied to Unsteady Viscous Flow Around 2D Blunt Bodies With Sharp Corners. (Dr.Ing. Thesis)
MTA-99-134	Elvekrok, Dag R., MP	Engineering Integration in Field Development Projects in the Norwegian Oil and Gas Industry. The Supplier Management of Norne. (Dr.Ing. Thesis)
MTA-99-135	Fagerholt, Kjetil, MP	Optimeringsbaserte Metoder for Ruteplanlegging innen skipsfart. (Dr.Ing. Thesis)
MTA-99-136	Bysveen, Marie, MM	Visualization in Two Directions on a Dynamic Combustion Rig for Studies of Fuel Quality. (Dr.Ing. Thesis)
MTA-2000-137	Storteig, Eskild, MM	Dynamic characteristics and leakage performance of liquid annular seals in centrifugal pumps. (Dr.Ing. Thesis)
MTA-2000-138	Sagli, Gro, MK	Model uncertainty and simplified estimates of long term extremes of hull girder loads in ships. (Dr.Ing. Thesis)
MTA-2000-139	Tronstad, Harald, MK	Nonlinear analysis and design of cable net structures like fishing gear based on the finite element method. (Dr.Ing. Thesis)
MTA-2000-140	Kroneberg, André, MP	Innovation in shipping by using scenarios. (Dr.Ing. Thesis)
MTA-2000-141	Haslum, Herbjørn Alf, MH	Simplified methods applied to nonlinear motion of spar platforms. (Dr.Ing. Thesis)
MTA-2001-142	Samdal, Ole Johan, MM	Modelling of Degradation Mechanisms and Stressor Interaction on Static Mechanical Equipment Residual Lifetime. (Dr.Ing. Thesis)

MTA-2001-143	Baarholm, Rolf Jarle, MH	Theoretical and experimental studies of wave impact underneath decks of offshore platforms. (Dr.Ing. Thesis)
MTA-2001-144	Wang, Lihua, MK	Probabilistic Analysis of Nonlinear Wave-induced Loads on Ships. (Dr.Ing. Thesis)
MTA-2001-145	Kristensen, Odd H. Holt, MK	Ultimate Capacity of Aluminium Plates under Multiple Loads, Considering HAZ Properties. (Dr.Ing. Thesis)
MTA-2001-146	Greco, Marilena, MH	A Two-Dimensional Study of Green-Water Loading. (Dr.Ing. Thesis)
MTA-2001-147	Heggelund, Svein E., MK	Calculation of Global Design Loads and Load Effects in Large High Speed Catamarans. (Dr.Ing. Thesis)
MTA-2001-148	Babalola, Olusegun T., MK	Fatigue Strength of Titanium Risers – Defect Sensitivity. (Dr.Ing. Thesis)
MTA-2001-149	Mohammed, Abuu K., MK	Nonlinear Shell Finite Elements for Ultimate Strength and Collapse Analysis of Ship Structures. (Dr.Ing. Thesis)
MTA-2002-150	Holmedal, Lars E., MH	Wave-current interactions in the vicinity of the sea bed. (Dr.Ing. Thesis)
MTA-2002-151	Rognebakke, Olav F., MH	Sloshing in rectangular tanks and interaction with ship motions. (Dr.Ing. Thesis)
MTA-2002-152	Lader, Pål Furset, MH	Geometry and Kinematics of Breaking Waves. (Dr.Ing. Thesis)
MTA-2002-153	Yang, Qinzheng, MH	Wash and wave resistance of ships in finite water depth. (Dr.Ing. Thesis)
MTA-2002-154	Melhus, Øyvin, MM	Utilization of VOC in Diesel Engines. Ignition and combustion of VOC released by crude oil tankers. (Dr.Ing. Thesis)
MTA-2002-155	Ronæss, Marit, MH	Wave Induced Motions of Two Ships Advancing on Parallel Course. (Dr.Ing. Thesis)
MTA-2002-156	Økland, Ole D., MK	Numerical and experimental investigation of whipping in twin hull vessels exposed to severe wet deck slamming. (Dr.Ing. Thesis)
MTA-2002-157	Ge, Chunhua, MK	Global Hydroelastic Response of Catamarans due to Wet Deck Slamming. (Dr.Ing. Thesis)
MTA-2002-158	Byklum, Eirik, MK	Nonlinear Shell Finite Elements for Ultimate Strength and Collapse Analysis of Ship Structures. (Dr.Ing. Thesis)
IMT-2003-1	Chen, Haibo, MK	Probabilistic Evaluation of FPSO-Tanker Collision in Tandem Offloading Operation. (Dr.Ing. Thesis)

IMT-2003-2	Skaugset, Kjetil Bjørn, MK	On the Suppression of Vortex Induced Vibrations of Circular Cylinders by Radial Water Jets. (Dr.Ing. Thesis)
IMT-2003-3	Chezhian, Muthu	Three-Dimensional Analysis of Slamming. (Dr.Ing. Thesis)
IMT-2003-4	Buhaug, Øyvind	Deposit Formation on Cylinder Liner Surfaces in Medium Speed Engines. (Dr.Ing. Thesis)
IMT-2003-5	Tregde, Vidar	Aspects of Ship Design: Optimization of Aft Hull with Inverse Geometry Design. (Dr.Ing. Thesis)
IMT-2003-6	Wist, Hanne Therese	Statistical Properties of Successive Ocean Wave Parameters. (Dr.Ing. Thesis)
IMT-2004-7	Ransau, Samuel	Numerical Methods for Flows with Evolving Interfaces. (Dr.Ing. Thesis)
IMT-2004-8	Soma, Torkel	Blue-Chip or Sub-Standard. A data interrogation approach of identity safety characteristics of shipping organization. (Dr.Ing. Thesis)
IMT-2004-9	Ersdal, Svein	An experimental study of hydrodynamic forces on cylinders and cables in near axial flow. (Dr.Ing. Thesis)
IMT-2005-10	Brodtkorb, Per Andreas	The Probability of Occurrence of Dangerous Wave Situations at Sea. (Dr.Ing. Thesis)
IMT-2005-11	Yttervik, Rune	Ocean current variability in relation to offshore engineering. (Dr.Ing. Thesis)
IMT-2005-12	Fredheim, Arne	Current Forces on Net-Structures. (Dr.Ing. Thesis)
IMT-2005-13	Heggernes, Kjetil	Flow around marine structures. (Dr.Ing. Thesis
IMT-2005-14	Fouques, Sebastien	Lagrangian Modelling of Ocean Surface Waves and Synthetic Aperture Radar Wave Measurements. (Dr.Ing. Thesis)
IMT-2006-15	Holm, Håvard	Numerical calculation of viscous free surface flow around marine structures. (Dr.Ing. Thesis)
IMT-2006-16	Bjørheim, Lars G.	Failure Assessment of Long Through Thickness Fatigue Cracks in Ship Hulls. (Dr.Ing. Thesis)
IMT-2006-17	Hansson, Lisbeth	Safety Management for Prevention of Occupational Accidents. (Dr.Ing. Thesis)
IMT-2006-18	Zhu, Xinying	Application of the CIP Method to Strongly Nonlinear Wave-Body Interaction Problems. (Dr.Ing. Thesis)
IMT-2006-19	Reite, Karl Johan	Modelling and Control of Trawl Systems. (Dr.Ing. Thesis)
IMT-2006-20	Smogeli, Øyvind Notland	Control of Marine Propellers. From Normal to Extreme Conditions. (Dr.Ing. Thesis)

IMT-2007-21	Storhaug, Gaute	Experimental Investigation of Wave Induced Vibrations and Their Effect on the Fatigue Loading of Ships. (Dr.Ing. Thesis)
IMT-2007-22	Sun, Hui	A Boundary Element Method Applied to Strongly Nonlinear Wave-Body Interaction Problems. (PhD Thesis, CeSOS)
IMT-2007-23	Rustad, Anne Marthine	Modelling and Control of Top Tensioned Risers. (PhD Thesis, CeSOS)
IMT-2007-24	Johansen, Vegar	Modelling flexible slender system for real-time simulations and control applications
IMT-2007-25	Wroldsen, Anders Sunde	Modelling and control of tensegrity structures. (PhD Thesis, CeSOS)
IMT-2007-26	Aronsen, Kristoffer Høye	An experimental investigation of in-line and combined inline and cross flow vortex induced vibrations. (Dr. avhandling, IMT)
IMT-2007-27	Gao, Zhen	Stochastic Response Analysis of Mooring Systems with Emphasis on Frequency-domain Analysis of Fatigue due to Wide-band Response Processes (PhD Thesis, CeSOS)
IMT-2007-28	Thorstensen, Tom Anders	Lifetime Profit Modelling of Ageing Systems Utilizing Information about Technical Condition. (Dr.ing. thesis, IMT)
IMT-2008-29	Berntsen, Per Ivar B.	Structural Reliability Based Position Mooring. (PhD-Thesis, IMT)
IMT-2008-30	Ye, Naiquan	Fatigue Assessment of Aluminium Welded Box-stiffener Joints in Ships (Dr.ing. thesis, IMT)
IMT-2008-31	Radan, Damir	Integrated Control of Marine Electrical Power Systems. (PhD-Thesis, IMT)
IMT-2008-32	Thomassen, Paul	Methods for Dynamic Response Analysis and Fatigue Life Estimation of Floating Fish Cages. (Dr.ing. thesis, IMT)
IMT-2008-33	Pákozdi, Csaba	A Smoothed Particle Hydrodynamics Study of Two-dimensional Nonlinear Sloshing in Rectangular Tanks. (Dr.ing.thesis, IMT/ CeSOS)
IMT-2007-34	Grytøyr, Guttorm	A Higher-Order Boundary Element Method and Applications to Marine Hydrodynamics. (Dr.ing.thesis, IMT)
IMT-2008-35	Drummen, Ingo	Experimental and Numerical Investigation of Nonlinear Wave-Induced Load Effects in Containerships considering Hydroelasticity. (PhD thesis, CeSOS)
IMT-2008-36	Skejic, Renato	Maneuvering and Seakeeping of a Singel Ship and of Two Ships in Interaction. (PhD-Thesis, CeSOS)

IMT-2008-37	Harlem, Alf	An Age-Based Replacement Model for Repairable Systems with Attention to High-Speed Marine Diesel Engines. (PhD-Thesis, IMT)
IMT-2008-38	Alsos, Hagbart S.	Ship Grounding. Analysis of Ductile Fracture, Bottom Damage and Hull Girder Response. (PhD-thesis, IMT)
IMT-2008-39	Graczyk, Mateusz	Experimental Investigation of Sloshing Loading and Load Effects in Membrane LNG Tanks Subjected to Random Excitation. (PhD-thesis, CeSOS)
IMT-2008-40	Taghipour, Reza	Efficient Prediction of Dynamic Response for Flexible amd Multi-body Marine Structures. (PhD-thesis, CeSOS)
IMT-2008-41	Ruth, Eivind	Propulsion control and thrust allocation on marine vessels. (PhD thesis, CeSOS)
IMT-2008-42	Nystad, Bent Helge	Technical Condition Indexes and Remaining Useful Life of Aggregated Systems. PhD thesis, IMT
IMT-2008-43	Soni, Prashant Kumar	Hydrodynamic Coefficients for Vortex Induced Vibrations of Flexible Beams, PhD thesis, CeSOS
IMT-2009-43	Amlashi, Hadi K.K.	Ultimate Strength and Reliability-based Design of Ship Hulls with Emphasis on Combined Global and Local Loads. PhD Thesis, IMT
IMT-2009-44	Pedersen, Tom Arne	Bond Graph Modelling of Marine Power Systems. PhD Thesis, IMT
IMT-2009-45	Kristiansen, Trygve	Two-Dimensional Numerical and Experimental Studies of Piston-Mode Resonance. PhD-Thesis, CeSOS
IMT-2009-46	Ong, Muk Chen	Applications of a Standard High Reynolds Number Model and a Stochastic Scour Prediction Model for Marine Structures. PhD-thesis, IMT
IMT-2009-47	Hong, Lin	Simplified Analysis and Design of Ships subjected to Collision and Grounding. PhD-thesis, IMT
IMT-2009-48	Koushan, Kamran	Vortex Induced Vibrations of Free Span Pipelines, PhD thesis, IMT
IMT-2009-49	Korsvik, Jarl Eirik	Heuristic Methods for Ship Routing and Scheduling. PhD-thesis, IMT
IMT-2009-50	Lee, Jihoon	Experimental Investigation and Numerical in Analyzing the Ocean Current Displacement of Longlines. Ph.d.-Thesis, IMT.
IMT-2009-51	Vestbøstad, Tone Gran	A Numerical Study of Wave-in-Deck Impact usin a Two-Dimensional Constrained Interpolation Profile Method, Ph.d.thesis, CeSOS.

IMT-2009-52	Bruun, Kristine	Bond Graph Modelling of Fuel Cells for Marine Power Plants. Ph.d.-thesis, IMT
IMT 2009-53	Holstad, Anders	Numerical Investigation of Turbulence in a Sekwed Three-Dimensional Channel Flow, Ph.d.-thesis, IMT.
IMT 2009-54	Ayala-Uraga, Efren	Reliability-Based Assessment of Deteriorating Ship-shaped Offshore Structures, Ph.d.-thesis, IMT
IMT 2009-55	Kong, Xiangjun	A Numerical Study of a Damaged Ship in Beam Sea Waves. Ph.d.-thesis, IMT/CeSOS.
IMT 2010-56	Kristiansen, David	Wave Induced Effects on Floaters of Aquaculture Plants, Ph.d.-thesis, CeSOS.
IMT 2010-57	Ludvigsen, Martin	An ROV-Toolbox for Optical and Acoustic Scientific Seabed Investigation. Ph.d.-thesis IMT.
IMT 2010-58	Hals, Jørgen	Modelling and Phase Control of Wave-Energy Converters. Ph.d.thesis, CeSOS.
IMT 2010- 59	Shu, Zhi	Uncertainty Assessment of Wave Loads and Ultimate Strength of Tankers and Bulk Carriers in a Reliability Framework. Ph.d. Thesis, IMT/ CeSOS
IMT 2010-60	Shao, Yanlin	Numerical Potential-Flow Studies on Weakly-Nonlinear Wave-Body Interactions with/without Small Forward Speed, Ph.d.thesis,CeSOS.
IMT 2010-61	Califano, Andrea	Dynamic Loads on Marine Propellers due to Intermittent Ventilation. Ph.d.thesis, IMT.
IMT 2010-62	El Khoury, George	Numerical Simulations of Massively Separated Turbulent Flows, Ph.d.-thesis, IMT
IMT 2010-63	Seim, Knut Sponheim	Mixing Process in Dense Overflows with Emphasis on the Faroe Bank Channel Overflow. Ph.d.thesis, IMT
IMT 2010-64	Jia, Huirong	Structural Analysis of Intect and Damaged Ships in a Collission Risk Analysis Perspective. Ph.d.thesis CeSoS.
IMT 2010-65	Jiao, Linlin	Wave-Induced Effects on a Pontoon-type Very Large Floating Structures (VLFS). Ph.D.-thesis, CeSOS.
IMT 2010-66	Abrahamsen, Bjørn Christian	Sloshing Induced Tank Roof with Entrapped Air Pocket. Ph.d.thesis, CeSOS.
IMT 2011-67	Karimirad, Madjid	Stochastic Dynamic Response Analysis of Spar-Type Wind Turbines with Catenary or Taut Mooring Systems. Ph.d.-thesis, CeSOS.
IMT - 2011-68	Erlend Meland	Condition Monitoring of Safety Critical Valves. Ph.d.-thesis, IMT.

IMT – 2011-69	Yang, Limin	Stochastic Dynamic System Analysis of Wave Energy Converter with Hydraulic Power Take-Off, with Particular Reference to Wear Damage Analysis, Ph.d. Thesis, CeSOS.
IMT – 2011-70	Visscher, Jan	Application of Particla Image Velocimetry on Turbulent Marine Flows, Ph.d.Thesis, IMT.
IMT – 2011-71	Su, Biao	Numerical Predictions of Global and Local Ice Loads on Ships. Ph.d.Thesis, CeSOS.
IMT – 2011-72	Liu, Zhenhui	Analytical and Numerical Analysis of Iceberg Collision with Ship Structures. Ph.d.Thesis, IMT.
IMT – 2011-73	Aarsæther, Karl Gunnar	Modeling and Analysis of Ship Traffic by Observation and Numerical Simulation. Ph.d.Thesis, IMT.
Imt – 2011-74	Wu, Jie	Hydrodynamic Force Identification from Stochastic Vortex Induced Vibration Experiments with Slender Beams. Ph.d.Thesis, IMT.
Imt – 2011-75	Amini, Hamid	Azimuth Propulsors in Off-design Conditions. Ph.d.Thesis, IMT.
IMT – 2011-76	Nguyen, Tan-Hoi	Toward a System of Real-Time Prediction and Monitoring of Bottom Damage Conditions During Ship Grounding. Ph.d.thesis, IMT.
IMT- 2011-77	Tavakoli, Mohammad T.	Assessment of Oil Spill in Ship Collision and Grounding, Ph.d.thesis, IMT.
IMT- 2011-78	Guo, Bingjie	Numerical and Experimental Investigation of Added Resistance in Waves. Ph.d.Thesis, IMT.
IMT- 2011-79	Chen, Qiaofeng	Ultimate Strength of Aluminium Panels, considering HAZ Effects, IMT
IMT- 2012-80	Kota, Ravikiran S.	Wave Loads on Decks of Offshore Structures in Random Seas, CeSOS.
IMT- 2012-81	Sten, Ronny	Dynamic Simulation of Deep Water Drilling Risers with Heave Compensating System, IMT.
IMT- 2012-82	Berle, Øyvind	Risk and resilience in global maritime supply chains, IMT.
IMT- 2012-83	Fang, Shaoji	Fault Tolerant Position Mooring Control Based on Structural Reliability, CeSOS.
IMT- 2012-84	You, Jikun	Numerical studies on wave forces and moored ship motions in intermediate and shallow water, CeSOS.
IMT- 2012-85	Xiang ,Xu	Maneuvering of two interacting ships in waves, CeSOS
IMT-	Dong, Wenbin	Time-domain fatigue response and reliability analysis of offshore wind turbines with emphasis

2012-86		on welded tubular joints and gear components, CeSOS
IMT-2012-87	Zhu, Suji	Investigation of Wave-Induced Nonlinear Load Effects in Open Ships considering Hull Girder Vibrations in Bending and Torsion, CeSOS
IMT-2012-88	Zhou, Li	Numerical and Experimental Investigation of Station-keeping in Level Ice, CeSOS
IMT-2012-90	Ushakov, Sergey	Particulate matter emission characteristics from diesel enignes operating on conventional and alternative marine fuels, IMT
IMT-2013-1	Yin, Decao	Experimental and Numerical Analysis of Combined In-line and Cross-flow Vortex Induced Vibrations, CeSOS
IMT-2013-2	Kurniawan, Adi	Modelling and geometry optimisation of wave energy converters, CeSOS
IMT-2013-3	Al Ryati, Nabil	Technical condition indexes doe auxiliary marine diesel engines, IMT
IMT-2013-4	Firoozkoohi, Reza	Experimental, numerical and analytical investigation of the effect of screens on sloshing, CeSOS
IMT-2013-5	Ommani, Babak	Potential-Flow Predictions of a Semi-Displacement Vessel Including Applications to Calm Water Broaching, CeSOS
IMT-2013-6	Xing, Yihan	Modelling and analysis of the gearbox in a floating spar-type wind turbine, CeSOS
IMT-7-2013	Balland, Océane	Optimization models for reducing air emissions from ships, IMT
IMT-8-2013	Yang, Dan	Transitional wake flow behind an inclined flat plate-----Computation and analysis, IMT
IMT-9-2013	Abdillah, Suyuthi	Prediction of Extreme Loads and Fatigue Damage for a Ship Hull due to Ice Action, IMT
IMT-10-2013	Ramìrez, Pedro Agustìn Pèrez	Ageing management and life extension of technical systems-Concepts and methods applied to oil and gas facilities, IMT
IMT-11-2013	Chuang, Zhenju	Experimental and Numerical Investigation of Speed Loss due to Seakeeping and Maneuvering. IMT
IMT-12-2013	Etemaddar, Mahmoud	Load and Response Analysis of Wind Turbines under Atmospheric Icing and Controller System Faults with Emphasis on Spar Type Floating Wind Turbines, IMT
IMT-13-2013	Lindstad, Haakon	Strategies and measures for reducing maritime CO2 emissons, IMT

IMT-14-2013	Haris, Sabril	Damage interaction analysis of ship collisions, IMT
IMT-15-2013	Shainee, Mohamed	Conceptual Design, Numerical and Experimental Investigation of a SPM Cage Concept for Offshore Mariculture, IMT
IMT-16-2013	Gansel, Lars	Flow past porous cylinders and effects of biofouling and fish behavior on the flow in and around Atlantic salmon net cages, IMT
IMT-17-2013	Gaspar, Henrique	Handling Aspects of Complexity in Conceptual Ship Design, IMT
IMT-18-2013	Thys, Maxime	Theoretical and Experimental Investigation of a Free Running Fishing Vessel at Small Frequency of Encounter, CeSOS
IMT-19-2013	Aglen, Ida	VIV in Free Spanning Pipelines, CeSOS
IMT-1-2014	Song, An	Theoretical and experimental studies of wave diffraction and radiation loads on a horizontally submerged perforated plate, CeSOS
IMT-2-2014	Rogne, Øyvind Ygre	Numerical and Experimental Investigation of a Hinged 5-body Wave Energy Converter, CeSOS
IMT-3-2014	Dai, Lijuan	Safe and efficient operation and maintenance of offshore wind farms ,IMT
IMT-4-2014	Bachynski, Erin Elizabeth	Design and Dynamic Analysis of Tension Leg Platform Wind Turbines, CeSOS
IMT-5-2014	Wang, Jingbo	Water Entry of Freefall Wedged – Wedge motions and Cavity Dynamics, CeSOS
IMT-6-2014	Kim, Ekaterina	Experimental and numerical studies related to the coupled behavior of ice mass and steel structures during accidental collisions, IMT
IMT-7-2014	Tan, Xiang	Numerical Investigation of Ship's Continuous-Mode Icebreaking in Level Ice, CeSOS